Finite Element Modeling and Simulation of Hard Disk Slider with In-Situ Flying Height Measurement Capability

He Han-Xiang

School of Mechanical and Aerospace Engineering

A thesis submitted to the Nanyang Technological University
in fulfilment of the requirement for the degree of
Doctor of Philosophy

2009

ABSTRACT

To achieve areal density of 1 Tb/in^2 in the next generation hard disk drive (HDD), the slider has to fly at a height of 3-4 nanometers above the disk surface. To obtain the required accuracy of track seeking and following, the same slider may have to possess capability of in-situ flying height (FH) measurement. A new slider has been proposed and designed with in-situ measurement capability of flying height and mechanical impedance of air bearing.

With proper aerodynamic design, the slider will fly at the prescribed height. Onto this slider, a much more flexible cantilever will be built to carry the read/write head at its tip. The flexible cantilever, which is driven by PZT film coated on its surfaces, is capable of measuring the flying height in real time. The output of the PZT, namely the electrical impedance, is used as a signal to sense the flying height.

Mechanically, this system has three coupling fields, which are related to electrical (PZT), structure (cantilever) and fluid (air bearing). In this PhD study, the air bearing is modeled as by Fukui model due to its accuracy for describing the air bearing in large Knudsen number. Finite element (FE) method was applied to study the cantilever, PZT film and air bearing by building a FE model for them. With the well established FE procedure, the in-situ flying height measurement capability of the new slider has been validated by virtual testing or numerical simulation. The numerical results show that there is a good linearity between the flying height and the output electrical impedance. The sensitivity could reach about 1.048 ohm per nanometer within a frequency range.

Moreover, simultaneous sensing and actuation (SSA) method has been applied for studying the mechanical impedance of air bearing of new slider design. Based on this method, the cantilever, PZT film and air bearing can be viewed as a four-pole device. With achieving the transduction matrix of the four-pole device, the mechanical impedance of air bearing will be obtained through measuring the output electrical impedance of PZT numerically. The results show well consistent with other researchers', with more advantages such as easy installment, light loading effect and real-time measurement capability.

Except for the above virtual testing of the new slider design, actual testing has been prepared, and the MEMS-based slider prototype has been fabricated. Although this prototype was not fabricated successfully due to the limitations of lab equipments and time, all these studies give us a clear direction on designing and fabricating the new slider for following researchers.

Index Terms --- flying height, head disk interface, in-situ, hard disk drive, air bearing, slider, SSA, MEMS, PZT, cantilever, four-pole, finite element.

ACKNOWLEDGEMENT

The author wishes to extend his greatest gratitude and appreciation to the following persons, who offered invaluable contribution towards my PhD study:

Professor Ling Shih-Fu, the project supervisor, for his distinguished guidance, respectable patience, and novel idea on the project, further more, for his excellent effort on scientific research and distinguished discovery on the novel method on dynamic systems. From him, I learnt much more about the research and life.

Dr. Liu Bo, the project co-supervisor, for his respectable guidance, effective discussion and creative advice. Moreover, he gives me lots of advices on research, work and life.

The love and the support of my family are instrumental in my ability to complete this report. To them this report is gratefully dedicated.

Dr. Zhang Mingsheng, who gives me lots of advices on the MEMS fabrication and slider design.

Thanks are also given to associate professor Qiu Jinhao, for his respectable guidance and help on the project.

Gratitude is also given to our research group, Ms. Hou Xiaoyan, Ms. Ying Yanling, Dr. Zhou Gangyi, Dr. Fu Lianyu, Dr. Liang Fenggang, Dr Ying Ming, Mr. Xiao Zhiyun, Mr. Wang Deyang, Mr. Peng Qunming and Mr XieJin, for effectively talking with them on this project.

My thanks also extend to Dr. Hu Min, Dr. Sun Yuhong, research fellows of MAE, for their kind assistance, and Ms. Li Xuhong, Mr. Han Yufei, research students of MAE, for their kind help.

Last but not least, each and everyone who had in one way or another, conducted towards the success of the project.

TABLE OF CONTENTS

LIST OF FIG.S

LIST OF TABLES

Chapter 1

Introduction

The ongoing growth of the computer industry and the advent of the information super-high way, high definition television, digital images, digital music etc., generate an enormous demand for data storage capacity. To satisfy the greatly increasing data storage capacity, several competing technologies are available, such as magnetic hard disk, optical disk, and magnetic flexible tape. However, magnetic hard disk technology continues to be the primary choice for high performance storage [1]. In the past 5 years, the areal density of disk drive storage grew 60% annually. Areal density of the order of 10 Gb/ in^2 is currently in production for laptop drives. Recently, the Read-Rite Corporation demonstrated a record areal density of 36Gb/in^2, and the next feasibility demonstration target for the disk drive industry is 1Tb/in^2. To obtain this areal density the required magnetic spacing should be moved to 10 nm or less. Advances in nanotechnology with regards to fabrication, characterization, and tribology are essential to achieve this areal density [2, 3]. The flying height (FH) is the main part of magnetic spacing. FH is the thickness of the air bearing, which is formed when hard disk drive is in the working state. A well-designed air bearing surface (ABS) is required to keep the slider fly several nanometers above the disk.

As the flying height decreases to a nanometer level, the methods of flying height measurement and flying height control should be performed accurately with much more modifications.

In a hard disk drive, the slider plays an important role, as it has a large influence on the ability of the hard disk drive. On one hand, a slider with a good aerodynamic design will increase the capability of the hard disk drive. On the other hand, the smaller the flying height of the slider will be, the larger the capacity of the disk will be. In such a low flying height, the contact between the slider and the disk becomes more and more frequently, which makes the slider more fragile. To reduce the contact, keeping a constant flying height is a demand. For this purpose, we must know the flying height value before controlling it. That is the reason we need to measure the flying height when the hard disk drive is in operation state. This kind of flying height measurement is called in-situ flying height measurement. Knowing the flying height, we can control it by some driving mechanisms. Both the method of in-situ flying height measurement and flying height control are receiving more and more attentions. In this research, we will focus on in-situ flying height measurement. Before introducing the further research, some fundamental concepts of hard disk drive will be described briefly in the following sections.

1.1 Fundamental of Hard Disk Drive

All the current hard disk drives contain the same elements as shown in Figure 1-1. One or more magnetic media hard disks are mounted on a spindle that rotates at a high speed.

When the hard disk drive is working, the voice-coil actuator controls the suspension for track seeking and following. A slider is mounted on the suspension through the gimbal. This gimbal is so flexible that the slider can move freely in a certain domain and directions. As the high speed of the rotating disk, there will be a thin film air produced between the slider and the disk. The slider, disk and the thin film air buildup the head-disk interface. Figure 1-2 shows the sketch of head-disk interface. Figure 1-3 shows the side view of head-disk interface.

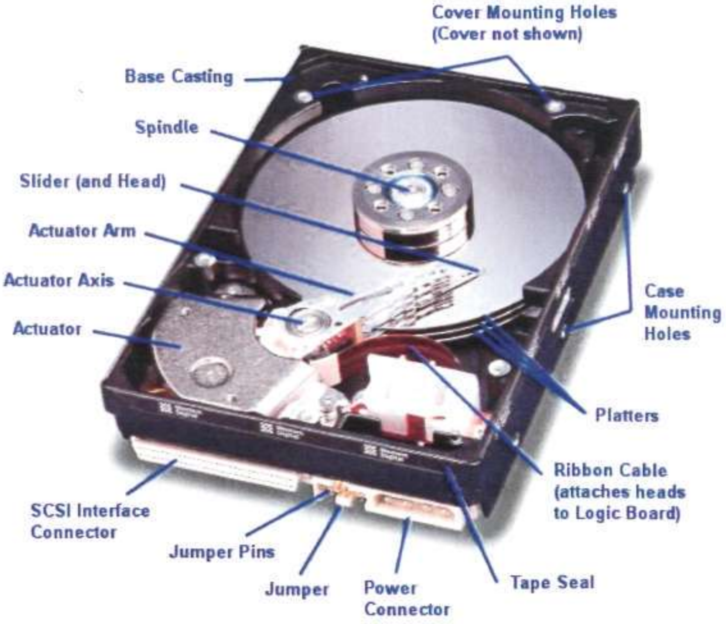

Fig. 1-1 Components of hard disk drives (IBM351-K 5400 20GB Disk Drive)

In all these components, the slider where the read/write elements are mounted is pivotal in the hard disk drive. The magnetic read/write elements (the "heads") are attached to the ceramic slider that is loaded onto the disk surface by a spring suspension. The air flow between the slider and disk generates a thin film air, which is a hydrodynamic air bearing. The air bearing provides a small spacing between the heads and the disk. This small space reduces the contact between the heads and the disk. The thickness of air bearing is normally called flying height as shown in Figure 1-3. Each suspension is attached to an arm. The arm is then fixed together to form a head stack assembly, which is driven by an electromagnetic voice-coil actuator. The heads can be positioned at any track on the disk surface.

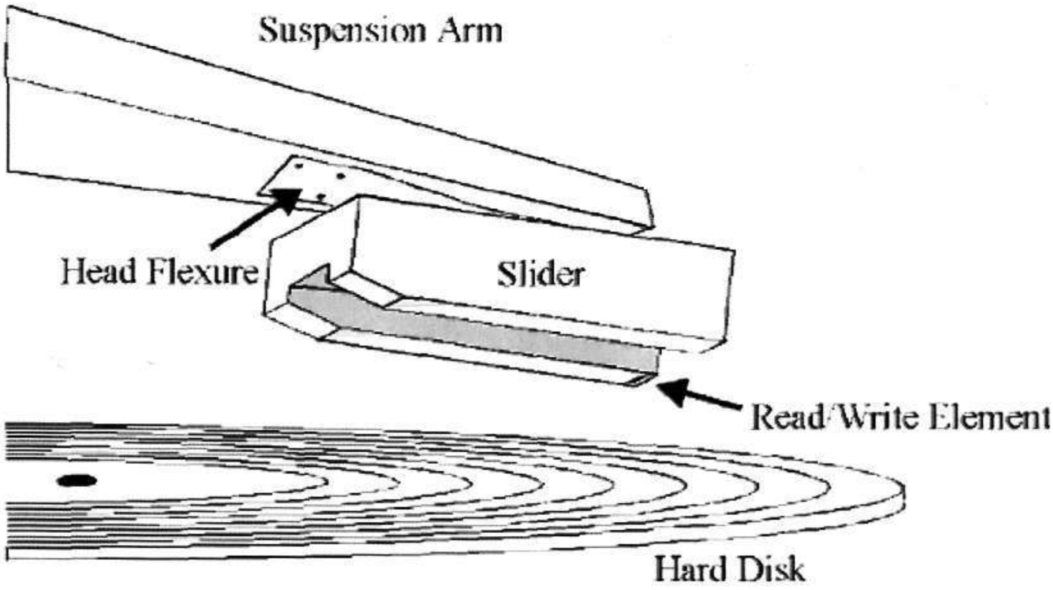

Fig. 1-2 Sketch of head-disk interface (Figure extracted from Hitachi webpage)

The hydrodynamic film, or air bearing, that supports the ceramic slider has traditionally made up the largest portion of the total spacing between the magnetic media and head. The air bearing is needed in order to minimize wear of the two surfaces-the magnetic disk and the slider. Ideally, when the disk is rotating at its full speed, the slider does not contact the disk surface and thus no wear occurs. In most designs, the slider lands on the

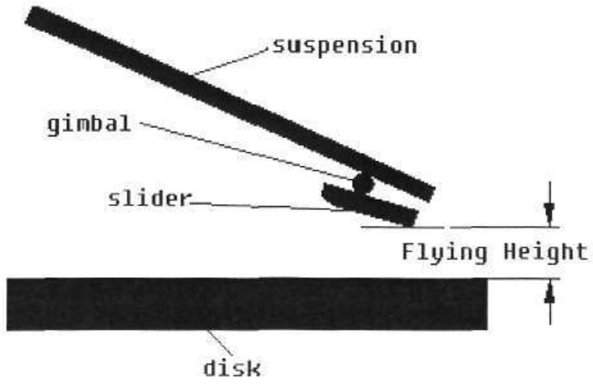

Fig. 1-3 Side view of head disk interface

disk when the disk is not spinning. When the drive is turned on, the disk spins up and the slider takes off as the air bearing forms. Flying height has much influence on the performance of hard disk drives. The larger the flying height is, the less possibility for the slider contacting with the disk is. Therefore, we need to enlarge the flying height. But, when the flying height is too large or not stable, the data transferring between the head and disk becomes slow. Thus, there is a tradeoff for the flying height in order to minimize the wear and keep high speed of data transferring.

Traditionally, the flying height is measured experimentally in design stage. For the past several decades, many methods have been developed for measuring flying height [4-17]. For example, the white-light interferometry method was used in 1972 by Lin and Sullivan [18] to measure flying height in hard disk drive. They claimed a resolution of 50 nm. Many individuals subsequently improved this technique. Best et al. obtained resolution down to a few nanometers in 1986. Miu et al. [19] reported on the first use of a laser doppler vibrometer (LDV) to study the motion of either the head or the disk. Since then, LDV has been used extensively in the study of the slider load/unload process and actuation. Methods other than optical ones have also been employed. In 1957, Brunner et al. used a capacitance probe to measure the flying height. More recently, Berg et al. [20] studied spacing during actuation in an actual disk file using a slider equipped with capacitance probes. The readback signal modulation from the magnetic transducer has also been utilized to measure the spacing variation [21]. The introduction of the magnetoresistive read/write element, which gives a signal independence of the relative velocity, makes this technique even more powerful, as it allows the measurement of steady changes in flying height. One drawback of the magnetic readback signal method [22], however, is that the spacing can only be determined at the trailing edge, where the head is located. With optical methods, the slider pitch and roll attitude, as well as the head-to-disk spacing, can be measured. These methods will be introduced in detail in Chapter 2. Although these methods are widely used in current industry, they are not used in the actual hard disk drive. Worse more, they are only used in the experimental stage. To solve this problem, and to carry out the flying height measurement when the hard disk drive is working, a new slider design and an in-situ flying height measurement technique have been proposed. Numerical simulation and mechanism study will be introduced and discussed in this thesis.

In the above discussion, we have introduced that the suspension is driven by voice-coil motor, such that the read/write element can be located on the expected track. This kind of actuation also is called single-stage actuation, as the flying height has lain into nanometer domains, the single-stage actuation is not enough for high demand of the accuracy. Recently, the dual-stage actuation was introduced. In this method, the read/write head is not only driven by the voice-coil actuator, but also by one more actuator. The latter actuator is called dual-stage actuator [23]. For the past years, researchers have developed many kinds of dual-stage actuators for more exactly track seeking, track following and flying height control in hard disk drives [24, 25, 26].

1.2 Proposed New Slider Design

Figure 1-4 shows the structural of a proposed slider design. A very small tip, or called step will be fabricated on the free end of the cantilever. The requirements of this slider are:

(1) A cantilever, together with PZT film coated onto its surface is formed inside the slider.

(2) The cantilever is much thinner and more flexible than other part of slider.

(3) The flying attitude of slider is mainly determined by the ABS on the slider body.

(4) The ABS on cantilever has little influence on the flying attitude.

(5) The flying attitude of the slider body hardly changed when the cantilever deforms.

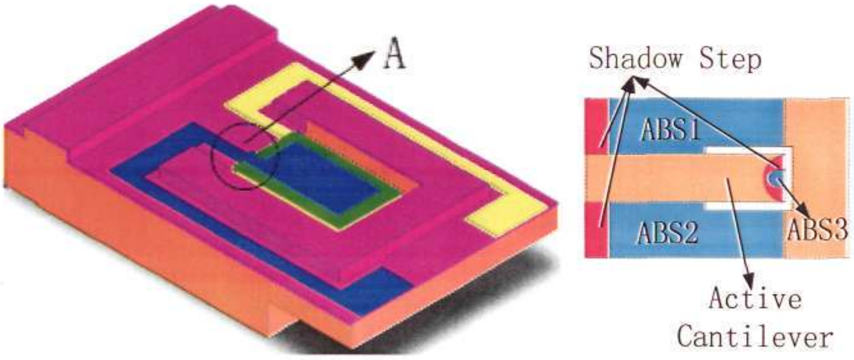

(a) Three-dimensional view (b) Bottom view

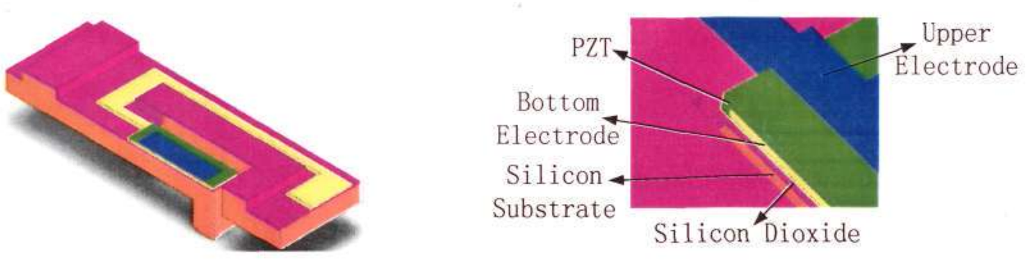

(c) Cross session view (d) Zoom-in view of part A

Fig. 1-4 Proposed slider design

In this figure, a PZT film is coated onto the surface of cantilever. And the PZT is sandwiched by two electrical layers. These two layers are used for the output electrical signal from PZT.

When a slider is flying above the disk surface during HDD's working state, air bearing is formed between slider and disk. Lift force from the air bearing is created to make the slider fly above the disk surface. The aerodynamic behavior of the air bearing is governed by classical Reynolds equation, which will be introduced in detailed in Chapter 2. The sensor, which is consisting of a flexible cantilever and a patch of PZT film, is also flying above the disk surface. So the cantilever, PZT film, air bearing and disk will construct the head disk interface (HDI). The flying height of the slider is same as the thickness of the air bearing at tip of the cantilever. At this moment, when a certain voltage with a prescribed frequency is input to the PZT, it will expand in the length direction due to its piezoelectricity. This expansion will cause the cantilever to be deformed. Due to the cantilever's deformation, the shape of the air bearing will be modified, which leads to the variation of the aerodynamic lift force produced on the cantilever. At the same time, because of the deformation on the cantilever, the inverse piezoelectricity will occur. This inverse piezoelectricity results into the variation of the output of PZT. The flying height of the slider will affect this output. Different flying height will cause different output of PZT film. To study the detailed relationship between flying height and this output, the HDI is viewed as a coupled multi-field problem which is consisting of electrical (PZT), structure (cantilever) and fluid (air bearing). For simplification, a stiffness matrix (1-1) is used to represent this system.

$$\begin{bmatrix} E & C_1 & C_2 \\ C_3 & S & C_4 \\ C_5 & C_6 & F \end{bmatrix} \tag{1-1}$$

The matrix (1-1) represents the system of head disk interface, in which E represents the electrical part, S represents the structural part, F represents the fluid part, and C_1-C_6 represents the coupling parts. In this project, the coupling field problem has been solved by a package using finite element (FE) method. Moreover, the novel slider, with in-situ flying height measurement capability, has been designed and fabricated by MEMS technology. We also know that there exist three fields in the whole system, electrical (PZT), structure (cantilever) and fluid (air bearing). In this research, we will find out the relationship between the output of PZT and the flying height. Here, the output of PZT will be the electrical impedance Z_e, which is defined as the ratio of the voltage U over the current I. U and I are the output voltage and output current of PZT respectively. That is

$$Z_e = U / I \tag{1-2}$$

1.3 Objectives

The objectives of this project are:

1. To develop a 1-D finite element program for solving a coupling field problem between air-bearing, cantilever and PZT response, as well as compare the results from the developed finite element program, ANSYS, CML-1st order and CML 2nd order analysis.

2. To develop some SSA applications on PZT cantilever/slider assembly. In our study, in-situ flying height measurement and in-situ mechanical impedance measurement are realized.

3. To explore the fabrication of the new slider by MEMS technology.

1.4 Scopes

The scopes of this project are to:

1. Derive the finite element matrix for the air-bearing, cantilever and PZT film respectively in its local coordinate. Then transforming the specific matrix into a global coordinate is a must to solve the coupling field problem. In our solution, the global coordinate is selected as same as the local coordinate of the air-bearing. Most of the numerical computational codes are written in MATLAB language, and some of the codes are written in FORTRAN. After the FE program has been developed, verification of these FE program is carried out through some simplified models.

2. Apply the sensor (PZT cantilever) to realize in-situ flying height measurement in the new slider design and build up a four-pole model of the cantilever together with PZT film as a sensor to measure mechanical impedance of air bearing.

3. Fabricate the slider with new design. Here MEMS technique is adopted. Firstly, a well mechanical structure design is carried out. The difference between the new slider and the

traditional slider lies on the PZT cantilever, which is used to realize the in-situ flying height measurement and in-situ mechanical impedance measurement. Since there is not mature product like this, deposition of the PZT on the cantilever is carried out by MEMS fabrication technique. Thermal analysis is carried out during MEMS fabrication due to the large temperature variation. Then mask for MEMS fabrication is designed, which helps the alignment of the wafer. At last, hand on slider fabrication is carried out.

1.5 Outline of Thesis

This thesis is organized as follows: In Chapter 2, a comprehensive literature review will be carried out to study the existing methods of flying height measurement, air bearing model and SSA method. In Chapter 3, finite element method will be used to simulate a PZT cantilever flying above disk surface. In this chapter, the derivation of finite element matrix for the coupling field system is introduced in detailed and the validation of the finite element package will be carried out through several simplified models. Then, in Chapter 4, the capability of in-situ flying height measurement of the new slider design is verified through ANSYS and the developed finite element package. In the following, the applications of the finite element package are used to virtually test the in-situ mechanical impedance measurement capability of new slider, which is shown in Chapter 5. In the same chapter, the MEMS fabrication of the proposed slider for actual testing will be shown. Even we could not obtain a good prototype through the fabrication due to limitation of lab equipments and time, these fabrication techniques will be served as guidance for the following researchers. In Chapter 6, the conclusions, including contributions, achievements and limitations, will be given. Some remarks for future research are also given. At the end of the thesis, some detailed design and analysis of the MEMS fabrication will be shown in the Appendix. At the same time, the cause of the failure of slider fabrication will be discussed and some recommendations for the future slider fabrication will also be given.

Chapter 2

Literature Review

In Chapter 1, some fundamental concepts of hard disk drive have been introduced. In this chapter, the existing methods of flying height measurement and the air bearing model will be presented. The SSA method will also be introduced in this chapter.

2.1 Flying Height Measurement in HDD

Up to now, optical interference techniques based on the Netwonian ring principle have mainly been used for static flying height measurement [27,28,29,30]. Except for the optical method, electrical methods similar to the capacitance probe have been utilized for dynamic flying height measurement [31]. Other methods, such as acoustic emission (AE) method, thermal acoustic (TA) method, strain gauge method, and magnetoresistance (MR) thermal response method, are also used in flying height measurement [32, 33]. In these methods, a monochromatic light source or a white light source was utilized to measure flying height by detecting the bright or dark fringe position on an air bearing surface or by comparing the color fringe with a series of standard unicolors corresponding to known spacing. Although these methods are very practical, their accuracy is questionable in the spacing range below 0.2 μm, and they present difficulties in measuring dynamic spacing fluctuation.

In an effort to solve these problems, Fleischer [34] first combined the photo-electrical detection technique with the optical interference technique. The measurement of the static characteristics of slider was fulfilled. In this technique, the interference intensity variation was detected through a focused infrared laser cavity. Nigam [35] improved the laser interferometric technique by employing a visible (He-Ne) laser as a light source. With this technique, flying height fluctuation resulting from suspension resonance could be measured successfully up to 2-kHz range.

Since Nigam's work, various flying height measurement techniques based on the photo-electrical conversion of interference intensity have been introduced. One typical aspect of these techniques involves determination of the wavelength. The light with such a wavelength could produce maximum and/or minimum interference intensity at a certain spacing by monochromatric scanning of a incident light wavelength. Another typical aspect concerns detecting the position, in which intensity indicates the maximum or minimum value along the surface of the air bearing. By detecting such a position, the spacing of leading or trailing edge could be extrapolated. The former is restricted, however, in its capability to measure the minimum spacing because of the limitation in shortening the wavelength. The latter also offers insufficient resolution since it produces few intensity peaks.

The Laser Doppler Vibrometer (LDV) [36,37,38], which can be used to measure the motion velocity of objects, is another optical method for evaluating the dynamic characteristics of the slider. Using LDV, Miu and Bogy measured transient motion in the slider caused by crater-like imperfections and sputtered rectangular aluminum oxide steps on the medium surface. These results were compared with the numerical results obtained directly from solving the modified Reynolds equation in the time domain. LDV is seen to be quite suitable for measuring the dynamic characteristics of a slider on a real medium, and is useful in directly evaluating the performance of the equipment. However, concerning to surface irregularities in the medium such as bumps, some difficulty exists in accurately measuring slider's relative motion. In addition, in order to attain an accurate transient response, it is absolutely essential to carefully eliminate all lower frequency disturbance components resulting mainly from medium run-out.

Against this background, Ohkubo and Kishigami [39, 40] presented an accurate spacing measurement technique which focuses a visible laser into a minute cavity on the slider and disk interface, and electrically detects the interference intensity change, which corresponds to the spacing variation. In this section several methods to measure flying height will be briefly reviewed.

2.1.1 Optical Interference Method

Optical interferometry has long been used for the accurate measurements of flying height. The principle of the method and its application for measuring flying height will now be described. The basic concept is shown in Figure 2-1. A monochromatic light beam is directed to pass through a transparent flat glass disk. Some light is reflected from the lower surface of the disk, and the rest passes into the air bearing. This part of the light reflects from the slider and is imaged into a detector that could be a photodetector or the human eye. Figure 2-1-1a shows the two optical paths merging at the detector P. Our

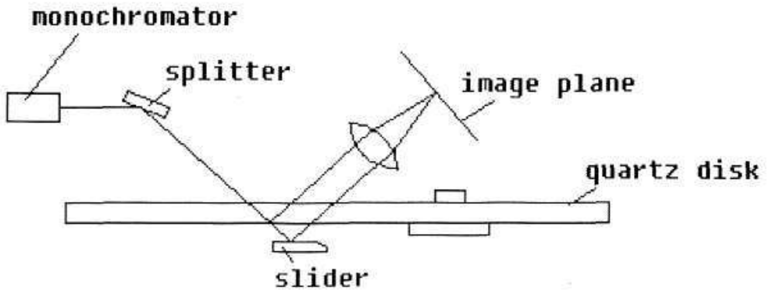

Fig. 2-1 Optical method for measuring flying height

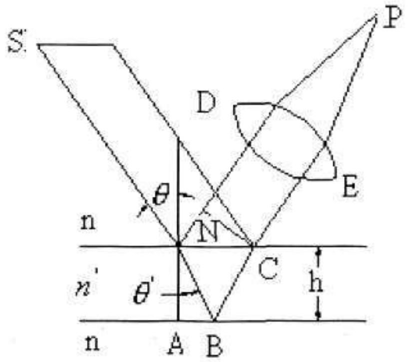

Fig. 2-1-1a Parallel-plate interferometry for flying height measurement

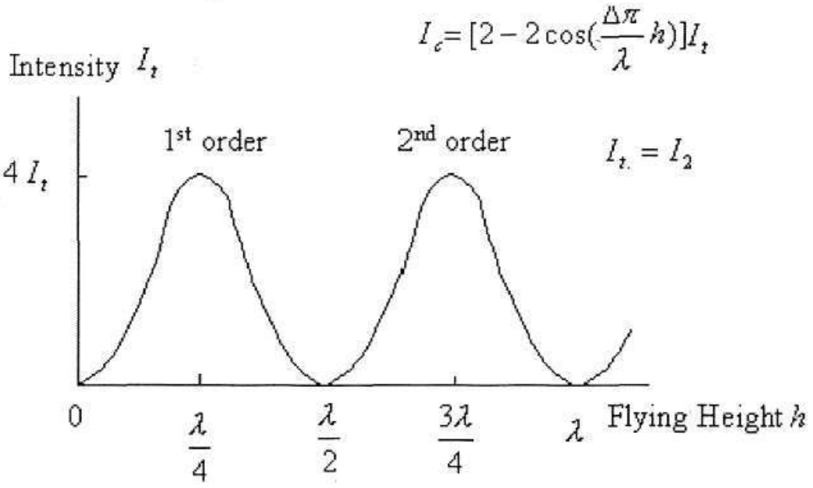

Fig. 2-1-1b Intensity variation (fringes) as a function of head-disk separation

interest is in knowing the intensity of resultant light detected at the detector P as the distance h between the disk surface and the slider surface varies from low to high values.

The intensity detected at P is due to the interference of two optical waves, one along the path ADP and another along path BCEP, given by

$$I_t = I_1 + I_2 - 2\sqrt{I_1 I_2}\cos\delta \qquad (2\text{-}1)$$

where I_1 and I_2 are intensities of two optical waves. The phase angle difference δ between two paths is proportional to the difference in path lengths between ADP and BCEP. The value of δ can be derived simply from the geometry shown in Figure 2-1-1a and using Snell's law of refraction for angles $\sin\theta$ and $\sin\theta'$. Assuming $I_1 = I_2$, the plot of intensity at the detector as a function of flying height is as shown in Figure 2-1-1b. As the value of h approaches $\frac{\lambda}{4}$ (called first order) or $\frac{3\lambda}{4}$ (second order), the intensity is maximum, while at 0, $\frac{\lambda}{2}$, and λ the detected intensity is zero. These intensities can be shown as fringes on a plot or by video imaging. The slope of the periodic curve in Figure 2-1-1b shows that the sensitivity of the measurements will be very small at maximum and minimum intensities, that is, at peaks and valleys of the curve, while it will highest at locations of highest slope, $h = \frac{1}{8}\lambda, \frac{3}{8}\lambda, \ldots$. For many years, the wavelength of light was sometimes selected to optimize measurement sensitivity for a given flying height. A standard source for these experiments is a mercury arc monochromator with a wavelength (λ) of 545 nm. The first-order optimized point for maximum sensitivity in this case is

$(\frac{1}{8}\lambda)$ or 68 nm. Measurements of flying height can be made at several points along a slider's rails. The accurate flying height at the head's position location can be computed based on the sliders geometry and the calculated pitch and roll angles.

2.1.2 Capacitance-stripe Method

The novel capacitance-stripe method was originated by Hegde, Scranton, and Yarmchuk [41]. In this method, a special disk and high-speed capacitance amplifier to yield profiles of the air bearing surface of a flying slider is used. Richard Sonnenfeld [42, 43] made a further research on this method, which make this method can be applied to measure nano-scale flying height. The capacitance-stripe technique can characterize sliders made of any electrically conducting material. A 10-nm-thick 200 um-wide radial metal stripe is sputtered or evaporated onto a disk substrate of insulating material. As shown in Figure 2-2, when the stripe passes under the rail of a flying slider, the intersection of the stripe and rail forms a parallel plate capacitor of area (A) determined by the product of the stripe width and the rail width. The distance (h) between these plates is the local flying height. One can measure the capacitance between slider and stripe (C) as a function of time, solve for plate spacing, and immediately calculate a profile of the flying slider rail. One can readily calculate from these profiles trailing-edge flying height. This method requires little calibration. The parallel-plate capacitor equation $C = \varepsilon_0 (A/h)$ may be used with little correction to calculate the spacing. For air, $\varepsilon_0 = 8.8(picofarad/meter)$.

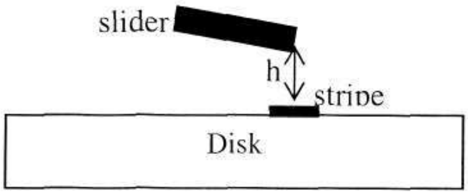

Fig. 2-2 Capacitance-stripe method to measure flying height

2.1.3 Readback Signal Method

In this section, the readback signal method for flying height measurement is discussed. The associated electronic instrumentation implementing these methods will be referred to as readback signal analyzer (RSA). In this method, the flying height measurement analyzed here rely on Wallace spacing loss [44] as measured from the change in relative harmonic content of the readback signal. Therefore, the first prerequisite is that the magnetization patterns recorded in the medium do not change during the actual measurement. It is immaterial whether or not this magnetic pattern was written with the same head as the read head under test. Neither is it important if the written magnetization becomes partially erased, as long as no appreciable erasure takes place during the measurement itself. It is also immaterial whether the read head is a Karlquist head, for instance, a (MIG) ferrite head, a finite pole tip head (thin-film inductive head), or a (G)MR head. It is also unimportant whether or not the magnetization is uniform throughout the medium thickness (as Wallace assumed). The measurement method works for saturation recording (hard disk drives) as well as for partial penetration recording (tape and diskette drives). The nature of the medium is not important either: The method works on particulate as well as on thin-film media.

If the RSA technique is used in the frequency sweep mode, i.e., the head-disk velocity is changed during the measurement, a second prerequisite is that the readback signal path must have a "flat" frequency characteristic over the frequency range of interest for the measurement. If this is not the case, the measurements can be corrected for a known "nonflat" frequency characteristic. This correction will not be discussed in this section.

A third prerequisite is that the read head, relative to which the flying height is measured, must be a linear transducer over the range of signal amplitudes occurring in the measurement. Nonlinearity is only allowed in as much as it produces even-order spectral harmonic distortion, because the RSA method will only use the odd harmonics in the readback spectrum. Thus, amplitude nonlinearity asymmetrical with respect to the signal baseline is allowable. This is, the major source of signal distortion in (G)MR heads. Any other nonlinearity is allowed only as long as it does not change over the range of signal amplitudes encountered in the measurement.

The RSA method for measuring flying height utilizes two basic measurement techniques: the ratio technique and the difference technique. The method is designed to be sensitive only to the ratio of the first (fundamental) harmonic amplitude and the third harmonic amplitude of the frequency spectrum of the readback signal being the largest two odd harmonics in the readback spectrum. This measurement method is, therefore, sometimes referred to as the harmonic ratio method (HRM). To arrive at displacements, spacings, and clearances, differences are measured before and after the displacement, spacing, or clearance occurred. The HRM constitutes, therefore, an incremental measurement. It is inherently calibrated and relies only on the Wallace spacing loss.

The "before-after" difference can be created artificially. For instance, in a (hard) disk drive, one can measure the flying height by measuring the difference before and after a spin-up (or spin-down) of the spindle motor. This difference can also be created by destroying the air bearing by different means (i.e., pumping down the air pressure in the drive or forcing the slider in contact).

The difference may also occur naturally. For instance, a change in flying height by a disk asperity with a positive interaction height can cause the slider to momentarily lift off. The resulting flying height change (and associated dynamics) can be measured directly by HRM. Another example of naturally occurring differences is the air pressure sensitivity of the flying height.

It should be mentioned that there are other ways of using Wallace spacing loss for flying height measurement that do not rely on a harmonic analysis. Klaassen and Peppen [45, 46] presented a method making use of the resulting changes in the half-amplitude pulse width (PW_{50}) of the readback signal.

As what we have seen, in the quest for higher and higher areal density, the linear density is under constant upward pressure. The isolated pulse width is a measure for the attainable linear density. One of the factors determining this pulse width is the (vertical) flying height. The flying height is also an important factor in the mechanical reliability of the head-disk interface.

The flying height is an important mechanical parameter that should be verified in a completed storage product. Such a noninvasive HRM measurement in-situ can be made from the analog readback signal using the signals that occur in the normal recording band and that can be written with a ready-to-ship device.

2.2 Existing Air Bearing Model in HDD

2.2.1 Reynolds Equation and Slip Model

In section 2.1, we have introduced the existing flying height measurement methods in the current industry. The researches show that quite a good result has been achieved. But to clearly know about what happens on the flying slider, we should learn more details on the air bearing, which is a layer of thin air flowing between the slider and the disk. The air bearing provides the lift force for the slider. During the past several decades, several models of the air bearing had been studied. In the following part, these existing models will be introduced. The comparisons among them will also be shown in detailed.

As we know, in the continuum limit, values of parameters such as density and viscosity at different points in the domain essentially represent averages of the microscopic behavior in the neighborhood of the point. This assumption eventually leads to the formulation of the Navier-Stokes (N-S) and energy equations. The air bearing, a layer of thin air flowing between the slider and the disk, is different from the macroscopic flow. The flow is rarefied and can be compressible. Thus the air bearing cannot be modeled based on the continuum concept and the no-slip hypothesis. The derivation from the continuum state is measured by the Knudsen number (K_n) which is defined as the ratio of the molecular mean free path (λ) to the characteristic domain length (L) and is written as: $K_n = \lambda / L$. When the K_n number exceeds 0.01, the pressure drop, shear stress, heat flux and the mass flow rate calculated from the general flow governing equations based on the continuum hypothesis are no longer accurate. When the K_n number is greater than 10 the flow is in the free molecular region and the appropriate governing equations must be determined using kinetic gas theories (see Figure 2-3). A classification of the different flow regimes is as follows: for flow with $K_n \leq 10^{-3}$, it can be considered as continuum, the N-S equations is still applicable; for flow with K_n>10, it is considered to be a free molecular flow; for flows with K_n between 10^{-3} and 10, they can neither be considered as continuum flows nor free molecular flows. A sub-classification is given in this regime, with slip flow defined as $10^{-3} < K_n < 0.1$ and transition flow for $0.1 < K_n < 10$. For all current hard disk drives, the K_n number is approximately in the region of 0.4 to 1.7 and there is a need to predict the flow accurately in this regime.

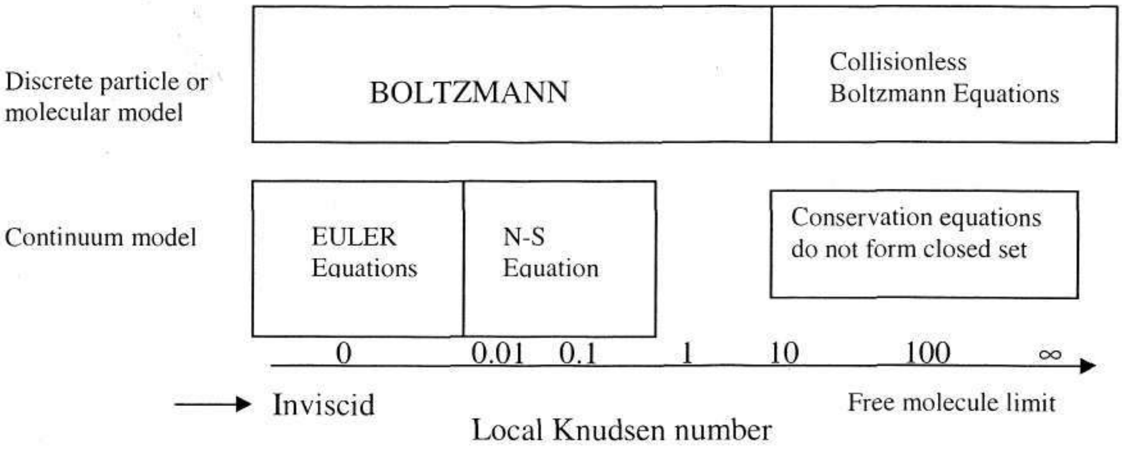

Fig. 2-3 The Knudsen number limits on the mathematical models

The classification is based on empirical information so the limits that classify the flows can be different depending on the problem geometry.

Up to now, there are two approaches for the simulation of rarefied flow. One comes from molecular kinetic theory that is particle-based and this is appropriate for high K_n number (K_n>>1), especially when the flow is in the free-molecular regime. The other approach attempts to make approximate corrections to the continuum model. The latter is suitable for flows in the slip region that may still be considered to be governed by the Navier-Stokes equations. However there is still a lack of understanding of flows in the transition regime though some models are said to be valid in the whole K_n number regime. This section will briefly review the fundamental theories for rarefied flows.

For 2-Dimensional simulations, the air bearing between the slider and the disk can be as a thin film. Assuming the air bearing to be steady, the momentum equation combined with the continuity equation will yield the Reynolds Equation. A sketch of this problem is shown in Figure 2-4 where the 2 sliders and the disk are separated by the air bearing of thickness h. The Reynolds Equation is a single differential equation relating pressure, density, fluid velocities and film thickness.

Several assumptions are made in deriving the Reynolds Equation:

•1. Body forces are neglected.

•2. Pressure is constant across the film.

•3. No slip at the boundaries

•4. Lubricant behaves as a Newtonian fluid

•5. Flow is laminar

•6. Fluid inertia is neglected

•7. Fluid density is constant

•8. Viscosity is constant throughout the fluid film

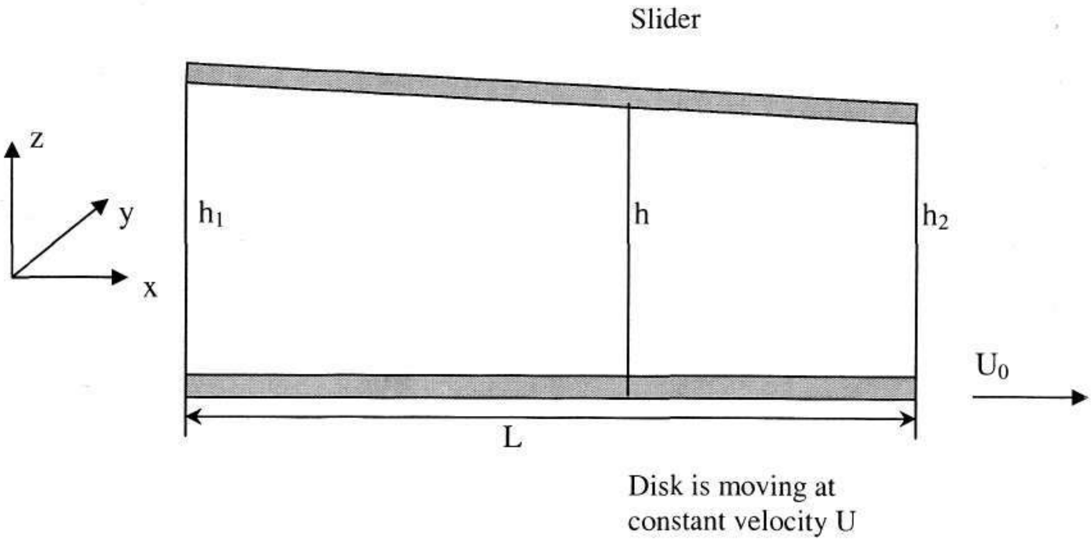

Fig. 2-4 Air bearing flow geometry

The well-known Reynolds Equation in its most general form can then be written as:

$$\frac{\partial}{\partial x}\left(\frac{\rho h^3}{\mu}\frac{\partial p}{\partial x}\right)+\frac{\partial}{\partial y}\left(\frac{\rho h^3}{\mu}\frac{\partial p}{\partial y}\right)=6\left\{2\frac{\partial}{\partial t}(\rho h)+\frac{\partial}{\partial x}[\rho h(u_1+u_2)]+\frac{\partial}{\partial y}[\rho h(v_1+v_2)]\right\} \qquad (2\text{-}2)$$

The boundary conditions are given respectively as: $u(x,y,0)=u_1$, $u(x,y,h)=u_2$, $v(x,y,0)=v_1$, $v(x,y,h)=v_2$, where u are the x-direction velocities and v are y-direction velocities.

Under the case of Figure 2-4, when the slider is fixed, the bottom disk is moving with a constant velocity U, that is $u(x,y,0)=U_0$, $u(x,y,h)=0$, using no-slip boundary condition v_1 and v_2 are equal to 0. The Reynolds Equation can be simplified to:

$$\frac{\partial}{\partial x}\left(\frac{\rho h^3}{\mu}\frac{\partial p}{\partial x}\right)+\frac{\partial}{\partial y}\left(\frac{\rho h^3}{\mu}\frac{\partial p}{\partial y}\right)=6\left\{2\frac{\partial}{\partial t}(\rho h)+\frac{\partial}{\partial x}(\rho U_0 h)\right\} \qquad (2\text{-}3)$$

Under most cases, the normalized Reynolds Equation is used. The normalizations are:

$$H=\frac{h}{h_2}\ ,\ X=\frac{x}{L}\ ,\ Y=\frac{y}{L}\ ,\ Z=\frac{z}{h_2}\ ,\ \gamma=\frac{\mu}{\mu_a}\ ,\ \Gamma=\frac{\rho}{\rho_a}\ ,\ P=\frac{p}{p_a}\ ,\ T=\omega t$$

where h_2 is the distance between the slider and the disk at the outlet. L is the length of the slider, μ_a , ρ_a and p_a are the fluid dynamic viscosity, density and pressure respectively at reference temperature and ω is an appropriate frequency, in hard disk systems this may be the characteristic angular speed.

In addition two other numbers are commonly used. They are:

Bearing number $\Lambda=\dfrac{6\mu_a U_0 L}{h_2^2 P_a}$, (2-4)

Squeeze number (for unsteady film) $\sigma = \dfrac{12\mu_a \omega L^2}{h(0)^2 P_a}$ (2-5)

Here the bearing number Λ can be understood to be a ratio of the Couette flow rate to the Poiseuille flow rate, while the squeeze number is a non-dimensional number for unsteady conditions. h(0) is the bearing thickness at t=0.

The non-dimensional form of the Reynolds Equation is written as:

$$\nabla \bullet \left(\frac{\Gamma H^3 \nabla P}{\gamma} \right) = \Lambda \frac{\partial}{\partial X}(\Gamma H) + \sigma \frac{\partial}{\partial T}(\Gamma H) \qquad (2\text{-}6)$$

This equation yields accurate results when the K_n number is less than 0.001 which corresponds to the continuum flow regime. But as the spacing between the slider and the disk decreases such that the K_n number is very near to 0.1, or even greater than 1, continuum no-slip boundary condition is no longer valid, as the current slider is flying at only a height of several nanometers above the disk. Hence the no-slip Reynolds Equation must be modified to take into account of slip at the boundaries.

There are several models [47-52] available to account for slip depending on the flow condition. These models are classified according to the approach they take. The following sections will provide a review of models based on the continuum approach. Subsequently, models derived using molecular gas dynamics or the Boltzmann equation will be presented.

2.2.1.1 Maxwell's Slip Model

Maxwell introduced a slip velocity in 1879 which is given by:

$$u_s - u_w = \frac{2-\sigma_v}{\sigma_v} \frac{1}{\rho\left(2RT_w \middle/ \pi\right)^{1/2}} \left(\frac{\partial u}{\partial n}\right)_s + \frac{3}{4} \frac{\Pr(\gamma-1)}{\gamma \rho R T_w}(-q_s) \qquad (2\text{-}7)$$

where n is the normal direction to the wall, Pr is the Prandtl number, γ is the ratio of specific heats and σ_v is the tangential momentum accommodation coefficient, q_s is the heat flux in the normal direction of the wall. The accommodation coefficient σ_v accounts for solid surface-fluid interactions.

When gas molecules impinge onto the solid surface, molecules exchange their normal and tangential momentum and energy according to the kinetic model. The extent to which the impingement reaches equilibrium is represented by the accommodation coefficients. The momentum exchange between molecules and wall is expressed by the normal and tangential momentum. In hard disk drive systems, since the length in the width direction is infinite only tangential momentum exchange is considered. The tangential accommodation coefficient is given by:

$$\sigma_v = \frac{\tau_i - \tau_r}{\tau_i - \tau_w} \qquad (2\text{-}8)$$

where τ_i and τ_r are the tangential momentum of incoming and reflected molecules, τ_w is the tangential momentum of re-emitted molecules. When σ_v =0, the reflection is specular in that the tangential velocity of the molecule reflected from the wall is unchanged. When σ_v =1, the reflection is termed diffusive since molecules are reflected from the walls with zero average tangential velocity. The accommodation coefficients are empirically determined and are functions of the surface and gas temperatures and environmental condition. Similarly, the energy accommodation coefficient σ_T is defined as:

$$\sigma_T = \frac{E_i - E_r}{E_i - E_w} \tag{2-9}$$

The accommodation coefficients are usually tabulated for certain interfaces of common gases and surfaces but diffuse reflection is likely to happen for rough surfaces which are common in engineering applications. The values for σ_v and σ_T are not necessarily to be equal.

2.2.1.2 Burgdorfer's First-Order Slip Model

Burgdorfer postulated that the slip velocity is a function of the molecular velocity that is at a distance of one mean free path away from the wall as illustrated in Figure 2-5. The following expression was proposed:

$$u_{slip} = f\frac{(2-\sigma)}{\sigma}\lambda\left.\frac{\partial u}{\partial z}\right|_{z=wall} \tag{2-10}$$

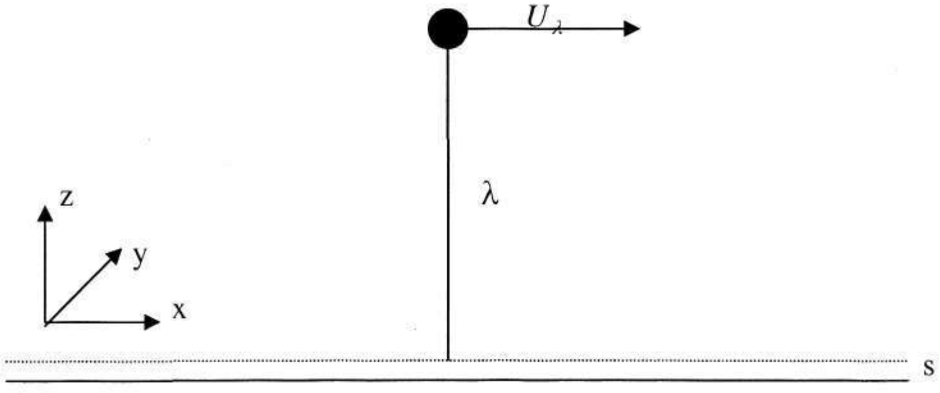

Fig. 2-5 Control surface for tangential momentum flux near an isothermal wall

where

f = a numerical constant

σ = surface accommodation coefficient

λ = mean free path of gas

In most cases, f and σ are set to be 1. In the case of the flow shown in Figure 2-5, using the Taylor Series expansion, the boundary velocities at the wall can be expressed as:

$$
\begin{aligned}
u(z=0) &= U_0 + \lambda \left.\frac{\partial u}{\partial z}\right|_{z=0} + \cdots\cdots \\
u(z=h) &= -\lambda \left.\frac{\partial u}{\partial z}\right|_{z=h} + \cdots\cdots \\
v(z=0) &= \lambda \left.\frac{\partial v}{\partial z}\right|_{z=0} + \cdots\cdots \\
v(z=h) &= -\lambda \left.\frac{\partial v}{\partial z}\right|_{z=h} + \cdots\cdots
\end{aligned}
\tag{2-11}
$$

The above boundary conditions are then substituted into the momentum equations:

$$
\begin{aligned}
\frac{\partial p}{\partial x} &= \mu \frac{\partial^2 u}{\partial z^2} \\
\frac{\partial p}{\partial y} &= \mu \frac{\partial^2 v}{\partial z^2} \\
\frac{\partial p}{\partial z} &= 0
\end{aligned}
\tag{2-12}
$$

Assuming the pressure gradients to be constant, Equation (2-12) can be integrated twice to yield the velocity distributions as follows:

$$\begin{aligned} u &= \frac{1}{2\mu}\frac{\partial p}{\partial x}z^2 + c_1 z + c_2 \\ v &= \frac{1}{2\mu}\frac{\partial p}{\partial y}z^2 + d_1 z + d_2 \end{aligned} \tag{2-13}$$

where c_1, c_2, d_1 and d_2 are constants. The constants can be determined by substituting the boundary conditions given by Equation (2-10) into Equation (2-11). This yields

$$\begin{aligned} u &= \frac{1}{2\mu}\frac{\partial p}{\partial x}\left(z^2 - hz - h\lambda\right) + U_0\left(1 - \frac{\lambda + z}{h + 2\lambda}\right) \\ v &= \frac{1}{2\mu}\frac{\partial p}{\partial y}\left(z^2 - hz - h\lambda\right) \end{aligned} \tag{2-14}$$

Replacing the expressions for u and v in the continuity equation and integrating it from z=0 to z=h, a modified first-order Reynolds Equation is derived:

$$\frac{\partial(\rho h)}{\partial t} + \frac{\partial(\rho U_0 h)}{\partial x}\frac{1}{2} = \frac{\partial}{\partial x}\left[\frac{1}{2\mu}\frac{\partial p}{\partial x}\rho\left(\frac{h^3}{6} + \lambda h^2\right)\right] + \frac{\partial}{\partial y}\left[\frac{1}{2\mu}\frac{\partial p}{\partial y}\rho\left(\frac{h^3}{6} + \lambda h^2\right)\right] \tag{2-15}$$

2.2.1.3 Hsia's Second-Order Slip Model

Based on Taylor series expansion the first order expression is only valid when the local K_n number is very small. For larger K_n number, second order molecular slip effects can no longer be neglected. Hsia proposed including second order terms to refine the definition of the boundary conditions for slip velocity as follows:

$$
\begin{aligned}
u(z=0) &= U_0 + \lambda \left.\frac{\partial u}{\partial z}\right|_{z=0} - \frac{\lambda^2}{2}\left.\frac{\partial^2 u}{\partial z^2}\right|_{z=0} + \cdots\cdots \\
u(z=h) &= -\lambda \left.\frac{\partial u}{\partial z}\right|_{z=h} - \frac{\lambda^2}{2}\left.\frac{\partial^2 u}{\partial z^2}\right|_{z=h} + \cdots\cdots \\
v(z=0) &= \lambda \left.\frac{\partial v}{\partial z}\right|_{z=0} - \frac{\lambda^2}{2}\left.\frac{\partial^2 v}{\partial z^2}\right|_{z=0} + \cdots\cdots \\
v(z=h) &= -\lambda \left.\frac{\partial v}{\partial z}\right|_{z=h} - \frac{\lambda^2}{2}\left.\frac{\partial^2 v}{\partial z^2}\right|_{z=h} + \cdots\cdots
\end{aligned}
\qquad (2\text{-}16)
$$

Based on these expressions, the velocity distributions can be obtained similarly as for the first order slip model:

$$
\begin{aligned}
u &= \frac{1}{2\mu}\frac{\partial p}{\partial x}\left(z^2 - hz - h\lambda - \lambda^2\right) + U_0\left(1 - \frac{\lambda + z}{h + 2\lambda}\right) \\
v &= \frac{1}{2\mu}\frac{\partial p}{\partial y}\left(z^2 - hz - h\lambda - \lambda^2\right)
\end{aligned}
\qquad (2\text{-}17)
$$

Replacing the velocity expressions above in the continuity equation the second-order slip boundary lubrication equation is obtained as follows:

$$
\frac{\partial(\rho h)}{\partial t} + \frac{\partial(\rho U_0 h)}{\partial x}\frac{1}{2} = \frac{\partial}{\partial x}\left[\frac{1}{2\mu}\frac{\partial p}{\partial x}\rho\left(\frac{h^3}{6} + \lambda h^2 + \lambda^2 h\right)\right] + \frac{\partial}{\partial y}\left[\frac{1}{2\mu}\frac{\partial p}{\partial y}\rho\left(\frac{h^3}{6} + \lambda h^2 + \lambda^2 h\right)\right]
$$

(2-18)

2.2.2 Boltzmann Equation and Slip Models

The models in Section 2.2.1 assume that the Navier-Stokes equations are applicable for the slip and transition regime. Modifications to the governing equations are incorporated through the use of slip models at the wall. However as mentioned before, the accuracy cannot be guaranteed in the transition regime where the K_n number exceeds the slip limit.

Although some of the models proposed reasonable estimates of the load carrying capacity in the transition regime, they lack rigorous physical interpretation. In particular, empirical parameters or adjustable coefficients are used arbitrary. In this section we will review models based on molecular kinetic theory.

2.2.2.1 Boltzmann Equation

Neutral gases are usually characterized by short-range interaction forces between molecules. In this situation, the Boltzmann equation describes changes of the velocity distribution function f (**r**,**c**) in space and time, where **r** is the position vector and **c** is the molecular velocity vector . This equation is based on molecular gas dynamics and gives reasonable results for flows with quite high Knudsen number in the near free molecular region. The rate of change of the number of molecules in an element is $\frac{\partial}{\partial t}(nf)dcdr$, where n is the number density, dc represents the physical space while dr represents the velocity space. In addition, c and r are independent variables if the location and shape of the element do not vary with time. There are three processes that contribute to the change in the number of molecules within dcdr:

(1) The convection of molecules across the face of dr by the molecular velocity c which may be expressed by:

$$-c \bullet \frac{\partial(nf)}{\partial r} dcdr \qquad (2\text{-}19)$$

The negative sign indicates that this is the net inflow of molecules while the positive direction is outwards.

(2) Similarly, the convection of net inflow molecules across the surface of dc as a result of the external force per unit mass F can be written as:

$$-F \bullet \frac{\partial (nf)}{\partial c} dcdr \tag{2-20}$$

(3) The scattering of molecules into and out of *dcdr* as a result of intermolecular collisions can be expressed as:

$$\int_{-\infty}^{\infty}\int_{0}^{4\pi} n^2 \left(f^* f_1^* - ff_1\right) c_r \sigma d\Omega dc_1 dcdr \tag{2-21}$$

Here the subscript '1' represents the molecule colliding the test molecule. c_r is relative molecular velocity and $\sigma d\Omega$ is the collision-cross section.

The Boltzmann equation for a simple dilute gas can then be written as

$$c \bullet \frac{\partial (nf)}{\partial r} dcdr + F \bullet \frac{\partial (nf)}{\partial c} dcdr + \frac{\partial}{\partial t}(nf) dcdr = \int_{-\infty}^{\infty}\int_{0}^{4\pi} n^2 \left(f^* f_1^* - ff_1\right) c_r \sigma d\Omega dc_1 dcdr \tag{2-22}$$

The Boltzmann equation is a complex differential-integral equation which is the conservation law at molecular level and it is almost impossible to derive an analytical solution. However, at equilibrium state where the gas has a homogeneous and time-independent distribution, that is $\frac{\partial f}{\partial t} = \frac{\partial f}{\partial r} = 0$, then it is possible to derive a solution for which is called the Maxwellian distribution. The Maxwell distribution is a statistical description of a molecular chaotic motion of molecular velocities. The Maxwell distribution function f_0 is:

$$f_0 = n\left(\frac{m}{2\pi kT}\right)^{\frac{2}{3}} e^{-\left(m/_{2kT}\right)\left(v_1^2+v_2^2+v_3^2\right)} \tag{2-23}$$

where the velocity of a molecule is V, with components v_1, v_2 and v_3. The number of molecules per unit volume with velocities within the range $v_1 \pm {}^{\delta v_1}/_2$, $v_2 \pm {}^{\delta v_2}/_2$, $v_3 \pm {}^{\delta v_3}/_2$ is $f_0\ (V)\delta v_1 \delta v_2 \delta v_3$ and n can be obtained by:

$$n = \iiint f_0 dv_1 dv_2 dv_3 \tag{2-24}$$

2.2.2.2 BGK Model and Slip Problem

The solution of the Boltzmann equation is, in general, of great difficulty even for cases corresponding to the simplest physical situations. The right hand side of equation (2-22) is called the collision term, which is the most complex term. Approximations to simplify this term were attempted. One approach involves an approximation to the form of the Boltzmann equation. As the collision term on the right hand side of the Boltzmann equation poses the greatest mathematical difficulties, this term is modified. The best-known model is the BGK model, which is introduced in 1954 by Bhatnagar, Gross and Krook and can be expressed as:

$$\frac{\partial}{\partial t}(nf) + c \cdot \frac{\partial}{\partial r}(nf) + F \cdot \frac{\partial}{\partial c}(nf) = n\nu(f_0 - f) \tag{2-25}$$

where ν is generally regarded as a collision frequency. It has a restricted functional dependence in that it is proportional to density and may depend on temperature, but is assumed to be independent of the molecular velocity c. f_0 is the local Maxwellian distribution function. The BGK model is consistent with conservation equations in that the collision term vanishes when moments are taken over the conserved quantities. The conservation law requires that the collision terms to be zero.

The BGK model is derived from the Chapman-Enskog theory. The basis of this theory is that when the distribution function f is perturbed by only a small amount from the equilibrium Maxwellian form, it can be expressed as:

$$f = f_0(1+\phi_1+\phi_2+\cdots\cdots) \tag{2-26}$$

where ϕ_j is the dissipation function or perturbation of the equilibrium distribution function and it depends only on the density, velocity and gas temperature. In most cases, only the first perturbation function is taken into account. To explicitly express the effects of the above-mentioned parameters, the distribution function f can be rewritten as:

$$f = f_0(1+\varepsilon\phi) \tag{2-27}$$

where ε represents the Mach number, ϕ represents the perturbation distribution function. Using perturbation quantities the BGK models can be non-dimentionalized as:

$$\varepsilon\xi_x\frac{\partial\phi}{\partial X}+\varepsilon\xi_y\frac{\partial\phi}{\partial Y}+\xi_z\frac{\partial\phi}{\partial Z}=\frac{1}{k_0}\left[-\phi+\omega+2(\xi_x v_1+\xi_y v_2+\xi_z v_3)+\left(\xi_x^2+\xi_y^2+\xi_z^2-\frac{3}{2}\right)\tau\right] \tag{2-28}$$

where

ϕ, ω, τ : perturbed quantities of velocity distribution function, density and temperature

ξ_x, ξ_y, ξ_z: molecular velocities

v_1, v_2, v_3: flow velocities

$$E = \frac{1}{\pi^{3/2}} \exp\left\{-\left(\xi_x^2 + \xi_y^2 + \xi_z^2\right)\right\}$$

$$\omega = \iiint_{\infty} (\phi \cdot E)\, d\xi_x d\xi_y d\xi_z$$

$$\tau = \frac{2}{3} \iiint_{\infty} \left[\left(\xi_x^2 + \xi_y^2 + \xi_z^2 - \frac{3}{2}\right) \cdot \phi \cdot E\right] d\xi_x d\xi_y d\xi_z$$

$$v_j = \iiint_{\infty} \left(\xi_j \phi \cdot E\right) d\xi_x d\xi_y d\xi_z \quad \text{j=1, 2 and 3}$$

$$k_0 = \left(2/\sqrt{\pi}\right) Kn_0$$

In cases where the thickness of the gas films is small compared with the other characteristic dimensions and the flow velocities in the z direction are negligibly small, the equation can be simplified as:

$$\varepsilon \xi_x \frac{\partial \phi}{\partial X} + \xi_z \frac{\partial \phi}{\partial Z} = \frac{1}{k_0}\left[-\phi + \omega + 2\left(\xi_x v_1\right) + \left(\xi_x^2 + \xi_y^2 + \xi_z^2 - \frac{3}{2}\right)\tau\right] \tag{2-29}$$

2.2.2.3 FK Model

Fukui and Kaneko [53] started from a linearized Boltzmann equation based on the BGK model. The basic equation is decomposed so as to describe the fundamental flows that depend on the gradients of pressure (Poiseuille flow), velocity (Couette flow) and temperature (thermal creep flow). As the FK model is derived from kinetic gas theory, it is believed that it can be used for arbitrary K_n number. However it is still very complex for numerical simulation.

The governing equation is the same as equations (2-28 or 2-29). The boundary conditions for diffusive reflection are:

$$\phi\big|_{\substack{z=0\\ \xi_z>0}} = \sigma_{w0} + 2\xi_x V_0 + \left(\xi_x^2 + \xi_y^2 + \xi_z^2 - \frac{3}{2}\right)\cdot \tau_w \ \big|_{z=0} \tag{2-30}$$

$$\phi\ \big|_{\substack{z=h\\ \xi_z<0}} = \sigma_{w,h} + \left(\xi_x^2 + \xi_y^2 + \xi_z^2 - \frac{3}{2}\right)\cdot \tau_w \ \big|_{z=h} \tag{2-31}$$

where

$$\sigma_{w0} = -\frac{1}{2}\tau_w \ \big|_{z=0} - 2\sqrt{\pi}\iiint_{\xi_z<0}\left(\xi_z \cdot \phi\ \big|_{z=0} \cdot E\right) d\xi_x d\xi_y d\xi_z \tag{2-32}$$

$$\sigma_{w,h} = -\frac{1}{2}\tau_w \ \big|_{z=h} + 2\sqrt{\pi}\iiint_{\xi_z>0}\left(\xi_z \cdot \phi\ \big|_{z=h} \cdot E\right) d\xi_x d\xi_y d\xi_z \tag{2-33}$$

The non-dimensional boundary temperatures are assumed to be of the form given by:

$$\begin{aligned} \tau_w \ \big|_{z=0} &= \gamma\left(X/_{\varepsilon}\right) \\ \tau_w \ \big|_{z=h} &= \gamma\left(X/_{\varepsilon}\right) + \Delta\tau_w \end{aligned} \tag{2-34}$$

ϕ can now be expressed as

$$\phi = \left(X/_{\varepsilon}\right)\cdot \phi_0\left(\xi_{i1}^2\right) + \xi_x \cdot \phi_1\left(Z, \xi_z, \xi_i^2\right) + \phi_2\left(Z, \xi_z, \xi_i^2\right) \tag{2-35}$$

and if ω and τ can be defined in a similar way as ϕ,

$$\omega_j = \iiint\left(\phi_j \cdot E\right) d\xi_x d\xi_y d\xi_z \tag{2-36}$$

$$\tau_j = \iiint\left(\frac{3}{2}\xi_i^2\right)\cdot\left(\phi_j \cdot E\right) d\xi_x d\xi_y d\xi_z \quad \text{j=X,Y,Z} \tag{2-37}$$

Then there exists the following relations:

$$\begin{aligned}\omega &= (X/\varepsilon)\omega_0 + \omega_2\\ \tau &= (X/\varepsilon)\tau_0 + \tau_2\end{aligned} \tag{2-38}$$

replacing the above relations to the original BGK equation and decomposing the resulting expression, the respective equations for ϕ_0, ϕ_1 and ϕ_2 are obtained as:

$$\phi_0 = \omega_0 + \left(\xi_i^2 - \frac{3}{2}\right)\tau_0 \tag{2-39}$$

$$\xi_z \frac{\partial \phi_1}{\partial Z} + \frac{1}{k_0}\phi_1 = \frac{1}{k_0}(2v_1) - \phi_0 \tag{2-40}$$

$$\xi_z \frac{\partial \phi_2}{\partial Z} + \frac{1}{k_0}\phi_2 = \frac{1}{k_0}\left[\omega_2 + \left(\xi_i^2 - \frac{3}{2}\right)\tau_2\right] \tag{2-41}$$

The boundary conditions for the decomposed equations are now obtained by replacing the above three expressions into equations (2-36) to (2-38). The velocity profile can be obtained by assuming that the flow is isothermal with constant boundary temperature.

To overcome the difficulties in solving the BGK model, Fukui and Kaneko introduced the use of a Poiseuille flow database to allow a quicker computation of a generalized lubrication equation for high K_n number gas bearing [54]. However this database is created by numerical calculations based on the linearized Boltzmann equation. While the interpolation method reduced the calculation time, it also compromised the accuracy of results obtained.

2.3 Simultaneous Sensing and Actuation Method and Four-pole Theory

Transducers may generally be divided into two classes: sensors and actuators. Sensors are devices which monitor a parameter of a system, hopefully without disturbing that parameter. In real sensors it is not possible to achieve the ideal of a transducer which monitors a parameter while having absolutely no affect on it, because the act of making a measurement requires either adding energy to the system or subtracting energy from system. We can minimize the effect of a sensor on the system by minimizing the energy exchange. For this reason, most sensors are low-power device and are small in order to minimize the load they impose on the system that they are monitoring. Actuators are devices which impose a state on a system, hopefully independent of the load applied to them. The ideal of a load-independent actuator can never be achieved for a transducer with finite energy, because there will always be a load exceeding its energy handling ability. In general, we minimize the effect of the load seen by the actuator by having high-power actuators, so that typical loads cause only a little perturbation.

The distinctions between sensors and actuators also explain why it is so difficult to build a transducer which functions well, as both a sensor and an actuator. Because it is extremely difficult to conceive a transducer design that produces a device that can function well, both as a sensor and as an actuator, very few transducers are used in a manner which takes advantage of this reversible nature.

With development of smart materials and structures, the coupling effects between electrical and mechanical domain have been studied widely. Ling and his team set up a new method called simultaneous sensing and actuation (SSA) method which used a four-pole model to simulate the electromechanical system. In their study, a piezoceramic inertial actuator is used to monitor structural integrity and measure mechanical impedance of a structure. When an AC power is applied, the inertial actuator exerts to the structure under testing a force which is the reaction due to accelerating a proof mass in the actuator without the need of a grounded support. Because of the electromechanical interaction taken place in the piezo-ceramic driver, its input electrical impedance directly correlates with the pseudo mechanical impedance of the structure at the excitation point. When this correlation, described by a 2 by 2 "transduction" matrix of the actuator, is fully known, the pseudo mechanical impedance of the structure at the excitation point can be quantitatively detected from the measured electrical impedance. In the following sections, the four-pole theory and the SSA method, as well as their application will be introduced.

2.3.1 Four-pole Theory

From the viewpoint of system dynamics, a complex system can be separated as many subsystems. Each subsystem is a multi-port device. The relationship of variables at different ports can be described with a transfer matrix. The theory is first used for circuit network analysis. In 1960's, the multi-port theory was applied on other subsystems including mechanical element, electromechanical element, hydraulic element, etc. Thereafter, the theory is commonly used for system modeling and element coupling [55]. Among various multi-port theories, two-port theory that has only one input port and one output port is more useful for its simple form and common usage.

A) Superposition and reciprocity theorems

In system theory, a linear system is mostly used. The superposition theorem and the reciprocity theorem are also commonly used. Firstly we introduce these two theorems.

The superposition theorem may be stated as follows: The response of a linear network containing a number of sources is the sum of the response to the sources taken individually.

The reciprocity theorem applies to linear networks (all-electrical or all-mechanical but not necessarily electromechanical) containing a single independent voltage or current (velocity or force) source. It is stated in one of two forms, depending upon the kind of source: (1) The current response in branch j due to a voltage source in branch k is equal to the current response in branch k with the same voltage source now placed in branch j; or (2) The voltage response between nodes p and q due to a current source between nodes r and s is equal to the voltage response between nodes r and s with the same current source now placed between nodes p and q. The two forms of this theorem are illustrated graphically in Figure 2-6.

(a) $I_1=I_2$

(b) $E_1=E_2$

Fig. 2-6 Graphical illustrations of the reciprocity theorem

B) Four-pole model

From the system point, a system can be simplified as a "black box" with two poles, that is, an input pole and an output pole shown in Figure 2-7. We can describe it using the transfer function which is output divided by input. In each terminal, there is only one variable. But we cannot define the power in terms of a single variable; two are required. The four-pole theory is used for this problem which is schematic ally shown in Figure 2-8.

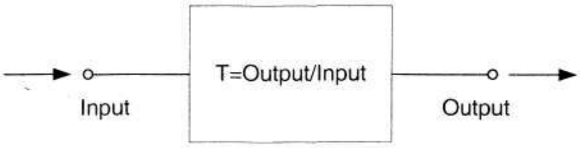

Fig. 2-7 Schematic one-port model

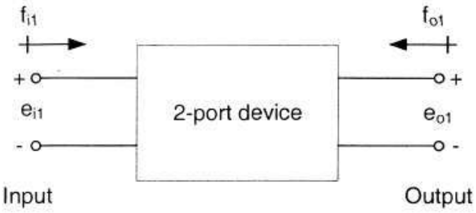

Fig. 2-8 Schematic four-pole model

The four-pole device exchanges energy with others at only two locations (ports). At each port we define two variables, one of which is selected as being of primary practical interest to use and the other, such that the product of the two variables gives the instantaneous power flowing through the port. We use the names effort variable and flow variable; other common usages are "across variable" and "through variable". The most common applications are shown in Table 2-1.

Table 2-1 Common application of four-pole model

Class of system	Effort variable (e)	Flow variable (f)
Electrical circuits	Voltage	Current
Mechanical systems	Force (Torque)	Velocity (Angle Velocity)
Hydraulic systems	Pressure	Volume flow rate

When investigating the transducer, regardless of its type or function, it can be viewed as a device which has input power and output power as shown in Figure 2-8. Each port is defined by two power conjugate variables, making for a total of four variables for the transducer. Two of these variables are designated as independent, and the remaining two are determined by the details of the transducer, so they are dependent variables. The goal of four-pole theory is to develop the likes between the independent and dependent variables. The conventional four-pole theory is severely restricted in application. It is generally regarded as a purely frequency domain approach (applicable to steady-state performance analysis only) that applies to four-pole whose elements are entirely linear.

There are six possible sets of choices for the independent variables used to represent an electromechanical transducer. For each of these we may generate the functional representation linking the dependent and independent variables. For example, suppose we choose the flows f_{in} and f_{out} as the independent variables. Then, in general, we may write the efforts as

$$\begin{aligned} e_{in} &= g(f_{in}, f_{out}) \\ e_{out} &= h(f_{in}, f_{out}) \end{aligned} \tag{2-42}$$

where g and h are functions defined by the details of the transduction. If g and h are linear functions, then we may rewrite equation (2-42) as

$$\begin{aligned} e_{in} &= af_{in} + bf_{out} \\ e_{out} &= cf_{in} + df_{out} \end{aligned} \tag{2-43}$$

Here the coefficients *a*,*b*,*c* and *d* have units of impedance. This representation is called, therefore, the impedance representation and the matrix [*Z*] is the coupler between the flows and the efforts. We can rewrite equation (2-43) in matrix form:

$$\begin{Bmatrix} e_{in} \\ e_{out} \end{Bmatrix} = [Z]\begin{Bmatrix} f_{in} \\ f_{out} \end{Bmatrix} = \begin{bmatrix} a & b \\ c & d \end{bmatrix}\begin{Bmatrix} f_{in} \\ f_{out} \end{Bmatrix} \tag{2-44}$$

The element Z_{11}, that is *a*, of the impedance matrix is referred to as the input impedance since it is the ratio of the input effort to input flow with the output flow set to zero. Similarly *d* is defined as the ratio of the output effort to the output flow when the input flow is zero, and is referred to as the output impedance. And *b* and *c* are transfer impedances, relating input effort to output flow, and output effort to input flow.

A second representation for the transducer uses the efforts as the independent variables and the flows as the dependent variables. Assuming linearity, this generally is written as

$$\begin{Bmatrix} f_{in} \\ f_{out} \end{Bmatrix} = [Y]\begin{Bmatrix} e_{in} \\ e_{out} \end{Bmatrix} = \begin{bmatrix} Y_{11} & Y_{12} \\ Y_{21} & Y_{22} \end{bmatrix}\begin{Bmatrix} e_{in} \\ e_{out} \end{Bmatrix} \tag{2-45}$$

where [*Y*] is the mobility or admittance matrix. Y_{11} is the ratio of the input flow to input effort with the output effort set to zero and is referred to as the input mobility. Y_{22} is the ratio of the output flow to the output effort with the input effort set to zero and is called the output mobility. Y_{12} and Y_{21} are the transfer mobility. The matrices of impedance and admittance are inverses of each other. We can get other possible representation for the transducer, such as

$$\begin{Bmatrix} e_{in} \\ f_{in} \end{Bmatrix} = \begin{bmatrix} a_{11} & -a_{12} \\ a_{21} & -a_{22} \end{bmatrix} \begin{Bmatrix} e_{out} \\ f_{out} \end{Bmatrix} \tag{2-46}$$

$$\begin{Bmatrix} e_{out} \\ f_{out} \end{Bmatrix} = \begin{bmatrix} b_{11} & -b_{12} \\ b_{21} & -b_{22} \end{bmatrix} \begin{Bmatrix} e_{in} \\ f_{in} \end{Bmatrix} \tag{2-47}$$

A passive transducer is the one energy can flow in either direction, i.e., which can function as either a sensor or an actuator. For such transducer, it is possible to derive relations which must hold true and which reduce some of the problems associated with measuring the elements of the various 2-port matrices. Then it is immaterial which port we label the input port and which is labeled the output port. We choose transfer representation of the transducer:

$$\begin{aligned} \begin{Bmatrix} e_{in} \\ f_{in} \end{Bmatrix} &= \begin{bmatrix} a_{11} & -a_{12} \\ a_{21} & -a_{22} \end{bmatrix} \begin{Bmatrix} e_{out} \\ f_{out} \end{Bmatrix} \\ &= \begin{bmatrix} a_{11} & -a_{12} \\ a_{21} & -a_{22} \end{bmatrix} \begin{bmatrix} b_{11} & -b_{12} \\ b_{21} & -b_{22} \end{bmatrix} \begin{Bmatrix} e_{in} \\ f_{in} \end{Bmatrix} \\ &= \begin{bmatrix} a_{11}b_{11} - a_{12}b_{12} & -a_{11}b_{12} + a_{12}b_{22} \\ a_{21}b_{11} - a_{22}b_{21} & -a_{21}b_{12} + a_{22}b_{22} \end{bmatrix} \begin{Bmatrix} e_{in} \\ f_{in} \end{Bmatrix} \end{aligned} \tag{2-48}$$

We identify the last matrix in equation (2-48) as the identity matrix. Hence the following relations must hold true:

$$\begin{aligned} & a_{11}b_{11} - a_{12}b_{12} = 1 \\ & -a_{11}b_{12} + a_{12}b_{22} = 0 \\ & a_{21}b_{11} - a_{22}b_{21} = 0 \\ & -a_{21}b_{12} + a_{22}b_{22} = 1 \end{aligned} \tag{2-49}$$

The relation of equation (2-49) might seem difficult to solve, being a set of four nonlinear algebraic equations in eight unknowns. However, there is a unique, easily verified solution, which is given below:

$$\begin{aligned} a_{11} &= b_{22} = A \\ a_{12} &= b_{12} = B \\ a_{21} &= b_{21} = C \\ a_{22} &= b_{11} = D \end{aligned} \tag{2-50}$$

$$AD - BC = 1 \tag{2-51}$$

here A,B,C and D are the four transfer matrix components that define the transducer. Equation (2-51) is called the reciprocity relation, which is the characteristic of the reciprocity.

2.3.2 SSA Method and Its Applications

2.3.2.1 Piezoceramic Inertial Actuator

In recent years, sensing capability of a piezoceramic inertial actuator was utilized to evaluate the pseudo mechanical impedance without involving conventional sensors like accelerometers, load cells, or impedance heads [56 - 59].

The structure of the piezoceramic inertial actuator (PIA) designed by Ling *et al.* is shown in Figure 2-9. The proof mass, the aluminium plate, the PZT patch, and other necessary frame works constitute a piezoceramic inertial actuator.

When the actuator is attached to a host structure, there is an electromechanical interaction between the host structure and the actuator. A two-port model can be used to model the actuator (see Fig. 2-10).

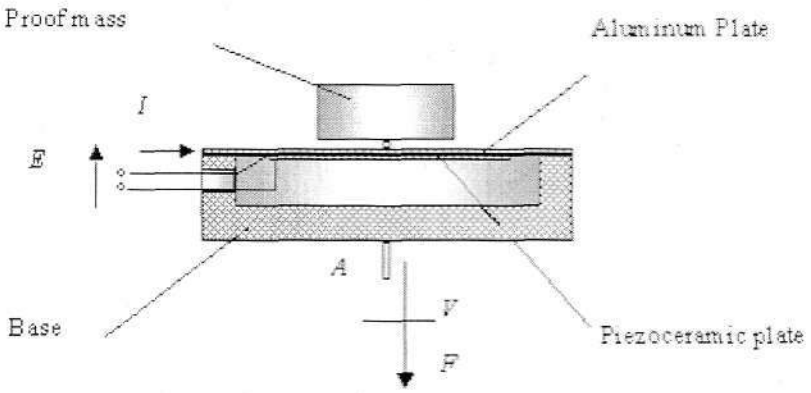

Fig. 2-9 Structure of a piezoceramic inertial actuator

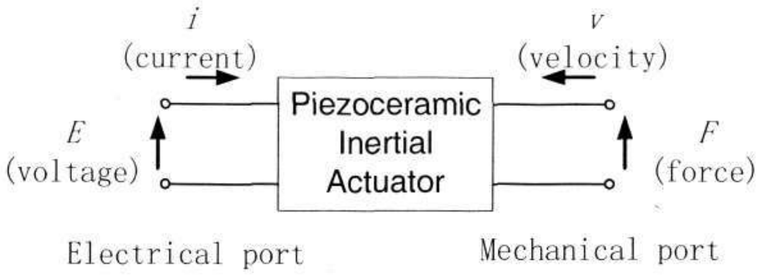

Fig. 2-10 Modeling of piezoceramic initial actuator

The relationship between the input electrical potential and current and the output mechanical force and velocity can be characterized by

$$\begin{Bmatrix} E \\ I \end{Bmatrix} = \begin{bmatrix} t_{11} & t_{12} \\ t_{21} & t_{22} \end{bmatrix} \begin{Bmatrix} F \\ V \end{Bmatrix} = [T] \begin{Bmatrix} F \\ V \end{Bmatrix} \tag{2-52}$$

[*T*] is named the transduction matrix of PIA and its four elements are complex transduction functions with both amplitude and phase information. They are in fact four different frequency response functions describing the relationships between one input variable and one output variable of the PIA in frequency domain. From Equation (2-52), $t_{11} = \frac{E}{F}|_{v=0}$ and $t_{21} = \frac{I}{F}|_{v=0}$ are the transduction functions of the input voltage and input current to the output force when the PIA is clamped onto the ground. Similarly, $t_{12} = \frac{E}{v}|_{F=0}$ and $t_{22} = \frac{I}{v}|_{F=0}$ are the transduction functions of the input voltage and current to the output velocity of PIA when the actuator is freely suspended.

From Equation (2-52), the mechanical impedance at the output port can be calculated from the measured input electrical impedance of the actuator:

$$Z_M = \frac{F}{v} = \frac{t_{12} - t_{22}Z_e}{t_{21}Z_e - t_{11}} \tag{2-53}$$

where F is the excitation force exerted to the host structure, v is the corresponding response velocity, Z_M is the point mechanical impedance of the test structure (which is also the excitation point), and $Z_e = E/\mathrm{I}$ is the input electrical impedance of the PIA device.

In this case, the mechanical impedance of the structure acts as a load to the actuator. The mechanical impedance is harder to measure than that of electrical impedance and was measured through electrical impedance. They use this smart structure to detect the mechanical impedance of a beam, the results agree with the other methods very well.

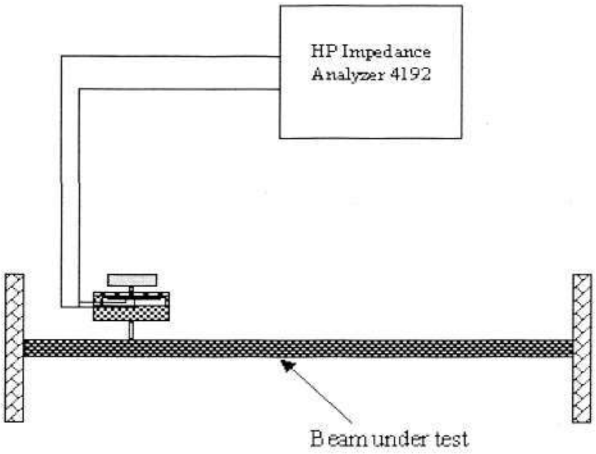

Fig. 2-11 Test mechanical impedance of a beam using PIA

2.3.2.2 Shaker SSA

An electromagnetic shakers are also can be modelled as a SSA device. Yin and Ling [60] used it to characterize soft incompressible viscoelastic materials.

Electromagnetic shakers are commonly used in mechanical testing as an exciter to provide artificial input forces to a dynamic system. When current passes through a coil placed in a magnetic field, a force F proportional to the current I and the magnetic flux intensity D, is produced which accelerates the component placed on the shaker table:

$$F = DIl \tag{2-54}$$

where l is the length of the coil. It should be noted that this very mechanism could also be employed to pick up velocity. When a coil moves in a magnetic field, a voltage E is generated in the coil:

$$E = DlV \tag{2-55}$$

where V is the velocity of the conductor relative to the magnetic field.

From Eq. (2-54) and Eq. (2-55), it is seen that

$$DI = \frac{E}{V} = \frac{F}{I} \tag{2-56}$$

Equation 2-56 shows that the electromechanical interaction of an electromagnetic device is reciprocal. This reciprocity nature of a linear electromechanical shaker can be better viewed as a two-port system with four poles similar to Fig. 2-10.

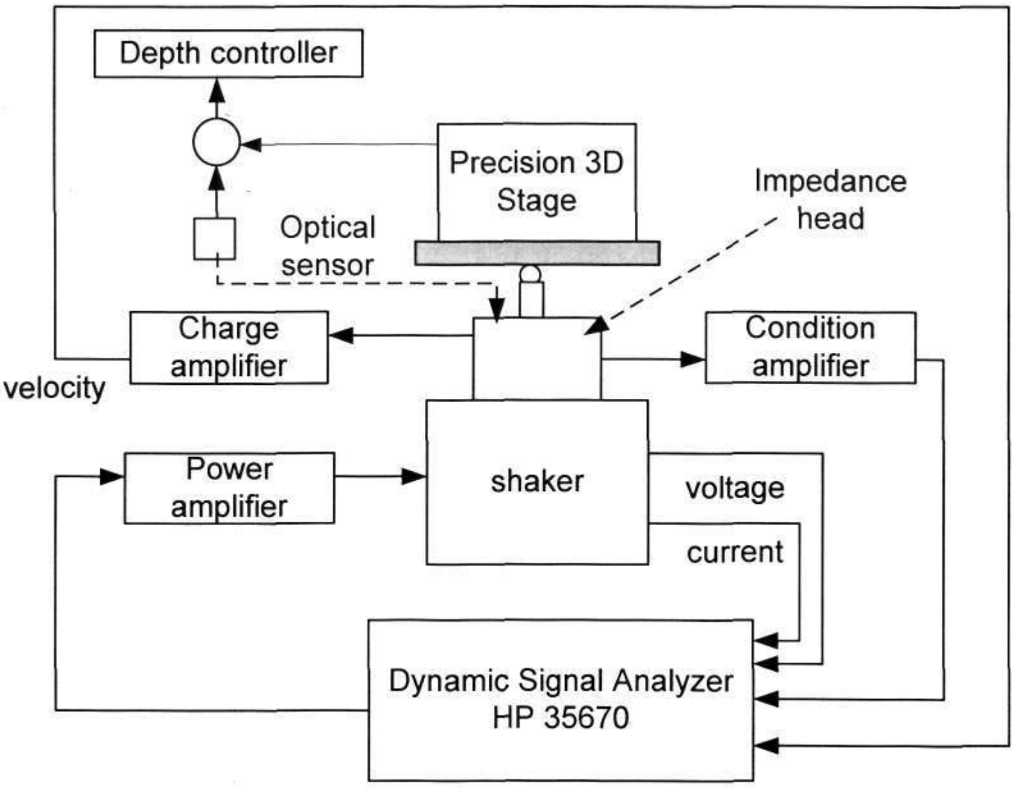

Fig. 2-12 Experiment setting up for soft material characterization

The experimental setup is shown in Fig. 2-12. Experimental results from their method on rubber materials show good agreement in a specific frequency range with those obtained by dynamic mechanical analyzer. Because no direct measurement of motion and force are required, this method possesses advantages in testing miniature samples in-situ and development into a low cost handy tool for characterization of soft tissues, such as human skin is in progress.

2.3.2.3 Other Applications

Besides the transducer introduced above, the SSA method has been applied in the study of measuring translational and rotational mechanical impedance by Hou and Ling since 2002. In their study, a new Bimorph Impedance Transducer was designed to measure both translational and rotational mechanical impedance accurately and conveniently [61]. The newly design BIT contains two series bimorph cantilevers, as insulating layer and a rigid supporting block, as shown in Fig. 2-13. The two bimorphs have identical geometric and material characteristic and are symmetrically glued to the Glass Epoxide insulating layer, which effectively prevents the charge convection between left and right bimorphs. The bottom insulating layer is tightly glued to the supporting block, which is made of aluminum.

As illustrated in this Fig. 2-14, if the left and right bimorphs are electrically connected in parallel, the ac electrical voltage supplied to the left and right bimorphs produces identical electrical fields. Hence the bimorphs bend upward or downward identically and synchronously. Dynamic forces and moments are generated at the connecting parts between the bimorphs and the supporting block due to the inverse piezoelectric effect. Because of the symmetric configuration of the transducer, the moments from the left and right bimorphs have same amplitude but opposite direction, therefore they cancel out each other; while, the dynamic forces from the left and right bimorphs are identical in both amplitude and direction, thus they are doubled in magnitude and exerted to the tested structure through the supporting block. In this process, the BIT functions actuation.

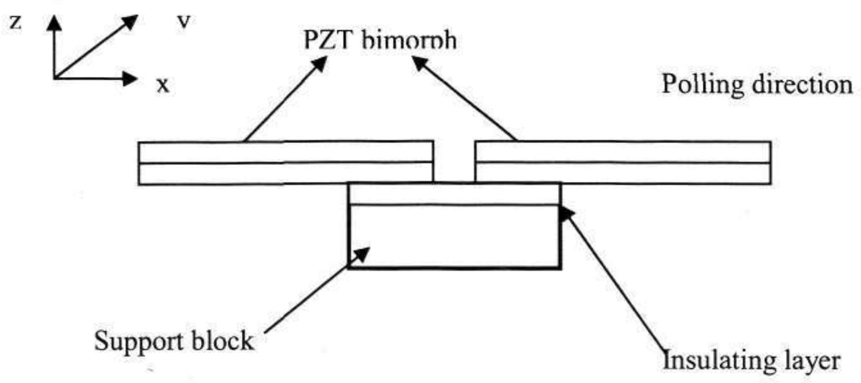

Fig. 2-13 Structure of bimorph impedance transducer

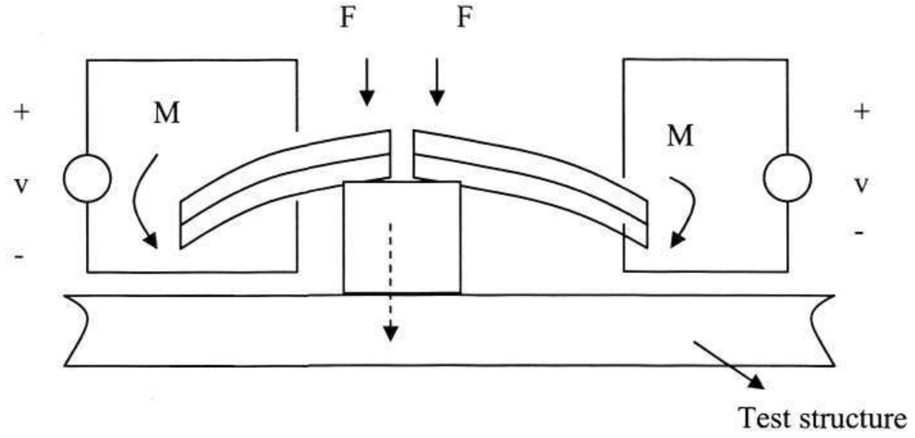

Fig. 2-14 Working principles of BIT for translational impedance measurement

At the same time of actuating, the response of the structure affects the motion of the transducer by introducing additional deformation to the piezoelectric bimorphs. The electrical impedance of the BIT changes due to direct piezoelectric effect. Therefore the deformation on flexural vibrations of the structure is embedded into the input electrical impedance of the transducer. It is possible to evaluate the translational impedance at the excitation point through measuring the input electrical impedance of the transducer. In this way, the transducer performs sensing simultaneously.

In their research, the transducer functions actuating and sensing simultaneously during measurement, which the measurement of translational/rotational impedance is simply performed by measuring the input electrical impedance of BIT. After calibration of transduction matrix, BIT is utilized to numerically measure translational/rotational impedance of structures ranging from one-dimensional beam, two-dimensional plate, to rigid block. And measuring results agree with analytical results by ANSYS. Further more, experiments are also successfully carried out to further examine the validity of BIT in translational and rotational impedance measurement. Finally, this transducer is applied to characterize linear viscoelastomers and magnetorheological elastomer.

SSA method was also used in the ultrasonic welding of thermoplastics, micro-drilling, measuring drilling torque and monitoring electrical discharge machining process, of which preliminary results could be found in some published papers. In summary, it is concluded that SSA method provides a neat and convenient way for studying mechanical performance of structure or material. It would be further studied to be used for measuring the mechanical impedance of the air bearing for our new slider design, which will be introduced in Chapter 5.

Chapter 3

Simulation of a PZT Cantilever Flying above Disk Surface

In Chapter 2, we have given a review of the methods for flying height measurement and the general model describing the characteristic of air bearing. Although these methods are widely used in the current industry, there is a key shortcoming of them. That is, they can not be used to realize the in-situ flying height measurement, which is a bottle-neck for us to fulfill the HDD's capability with the area density of $1 Tb/in^2$. In this high density, nano-track following and seeking control are two key contributors. To improve the track following and seeking capability, it is required to know the actual flying height before the control command is sent out. For this purpose, an in-situ flying height measurement mechanism is required. In Chapter 1, a proposed slider design with in-situ flying height measurement capability has been shown. A sensor consisting of cantilever and PZT film is flying above disk surface and used for flying height measurement. To study its capability, finite element method is used and finite element model is built for the sensor (a PZT cantilever) flying above the disk surface.

3.1 Finite Element Model of PZT Cantilever Flying above Disk Surface

From the previous discussions in Chapter 1, it is seen that when the PZT cantilever is flying above disk surface, the system that would be considered consists of three fields, electrical (PZT), structure (cantilever) and fluid (air bearing). To build-up the FE model of this system, the finite element matrix for each field will be derived firstly and introduced in the following sections.

3.1.1 Finite Element Matrix for Air Bearing

When the flying height reaches within several nanometers, the slip model or FK model of Reynolds equation should be used for accurately representing the air bearing. Ruiz and Bogy [62] had certified that for nano-scale flying height or high Knudsen number, the FK model gives a better approximation than the other slip models. So in our research, the FK model was used to model the air bearing. For air bearing shown in Figure 3-1, the equation of FK model for one-dimensional, static state is given below,

$$\frac{d}{dX}(QPH^3\frac{d}{dX}P-\Lambda_x PH)=0 \qquad (3\text{-}1)$$

where

X=x/l, slider length,

P=p/ p_a , p: pressure, p_a : ambient pressure,

H=h/ h_0 ,h: local flying height; h_0 : minimum flying height,

Q, flow rate coefficient of Poiseuille flow,

Λ_x ,bearing number in X direction.

The boundary condition for it is:

P(X=0)=P(X=1)=1,that is to say, the pressure at the boundary is equal to the ambient pressure.

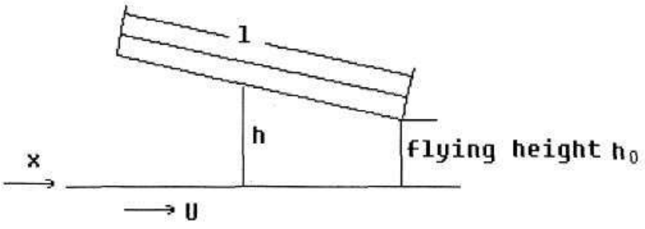

Fig. 3-1 Air bearing configuration

Equation (3-1) is a differential and nonlinear equation, in which P and H are two unknown variables. To solve P and H, we use numerical method. Here the finite element method was selected. In the following part, the derivation of finite element matrix for this governing equation will be described.

We assume $\overline{P}$ and $\overline{H}$ are the solution of the Eq. (3-1). With the help of Galerkin method, we get

$$\int_L [\frac{d}{dX}(Q\overline{PH}^3 \frac{d}{dX}\overline{P} - \Lambda_x \overline{PH})]NdX = 0, \tag{3-2}$$

Here N is the interpolation function.

As equation (3-2) is applicable to the whole domain, it is also applicable to the sub-domain. So, for each element, we have

$$\int_{L^{(e)}} [\frac{d}{dX}(QP^{(e)}H^{(e)^3} \frac{d}{dX}P^{(e)} - \Lambda_x P^{(e)}H^{(e)})]N_i^{(e)}dX = 0, \quad \text{i=1,2,3,…,r} \tag{3-3}$$

Where

$$P^{(e)} = \sum N_i^{(e)} P_i^{(e)} = \lfloor N \rfloor \{P\}^{(e)} \tag{3-4}$$

$$H^{(e)} = \sum N_i^{(e)} H_i^{(e)} = \lfloor N \rfloor \{H\}^{(e)} \tag{3-5}$$

$$\{P\}^{(e)} = [P_1 \;\; P_2 \;\; P_3 \ldots P_r]^T \tag{3-6}$$

$$\{H\}^{(e)} = [H_1 \;\; H_2 \;\; H_3 \ldots H_r]^T \tag{3-7}$$

Here, r is the number of elements.

Integrating equation (3-3) by parts, we get

$$N_i^{(e)}(QP^{(e)}H^{(e)^3}\frac{dP^{(e)}}{dX} - \Lambda_x P^{(e)}H^{(e)})\big|_{L^{(e)}} - \int_{L^{(e)}}(QP^{(e)}H^{(e)^3}\frac{dP^{(e)}}{dX} - \Lambda_x P^{(e)}H^{(e)})\frac{dN_i^{(e)}}{dX}dX = 0 \tag{3-8}$$

That is

$$\int_{L^{(e)}}(QP^{(e)}H^{(e)^3}\frac{dP^{(e)}}{dX} - \Lambda_x P^{(e)}H^{(e)})\frac{dN_i^{(e)}}{dX}dX = N_i^{(e)}(QP^{(e)}H^{(e)^3}\frac{dP^{(e)}}{dX} - \Lambda_x P^{(e)}H^{(e)})\big|_{L^{(e)}} \tag{3-9}$$

Here

$$\frac{dP^{(e)}}{dX} = \left\lfloor \frac{dN_1^{(e)}}{dX} \;\; \frac{dN_2^{(e)}}{dX} \;\; \frac{dN_3^{(e)}}{dX} \;\; \cdots \frac{dN_r^{(e)}}{dX} \right\rfloor \{P\}^{(e)} = \left\lfloor \frac{dN}{dX} \right\rfloor \{P\}^{(e)} \tag{3-10}$$

$$\left\lfloor \frac{dN}{dX} \right\rfloor = \left\lfloor \frac{dN_1^{(e)}}{dX} \;\; \frac{dN_2^{(e)}}{dX} \;\; \frac{dN_3^{(e)}}{dX} \;\; \cdots \frac{dN_r^{(e)}}{dX} \right\rfloor \tag{3-11}$$

We define

$$F_i = N_i^{(e)}(QP^{(e)}H^{(e)^3}\frac{dP^{(e)}}{dX} - \Lambda_x P^{(e)}H^{(e)})\big|_{L^{(e)}} \tag{3-12}$$

From equation (3-9), we have

$$\int_{L^{(e)}}(QP^{(e)}H^{(e)^3}\frac{dP^{(e)}}{dX} - \Lambda_x P^{(e)}H^{(e)})\frac{dN_i^{(e)}}{dX}dX = F_i \tag{3-13}$$

Substitute Eq. (3-4), (3-5) and (3-10) into Eq. (3-13), we get

$$\int_{L^{(e)}} (Q\lfloor N \rfloor \{P\}^{(e)} \{\lfloor N \rfloor \{H\}^{(e)}\}^3 \left\lfloor \frac{dN}{dX} \right\rfloor \{P\}^{(e)} - \Lambda_x \lfloor N \rfloor \{P\}^{(e)} \lfloor N \rfloor \{H\}^{(e)}) \frac{dN_i^{(e)}}{dX} dX = F_i \quad (3\text{-}14)$$

As

$$\begin{aligned}
&\lfloor N \rfloor \{P\}^{(e)} \{\lfloor N \rfloor \{H\}^{(e)}\}^3 \left\lfloor \frac{dN}{dX} \right\rfloor \{P\}^{(e)} \\
&= [\lfloor N \rfloor \{P\}^{(e)} \{\lfloor N \rfloor \{H\}^{(e)}\}^3 \left\lfloor \frac{dN}{dX} \right\rfloor]\{P\}^{(e)} \\
&= [(\sum_{s=1}^{r} N_s^{(e)} P_s^{(e)})(\sum_{j,k,l=1}^{r} N_j^{(e)} N_k^{(e)} N_l^{(e)} H_j^{(e)} H_k^{(e)} H_l^{(e)}) \left\lfloor \frac{dN}{dX} \right\rfloor]\{P\}^{(e)} \\
&= [(\sum_{s,j,k,l=1}^{r} N_s^{(e)} N_j^{(e)} N_k^{(e)} N_l^{(e)} P_s^{(e)} H_j^{(e)} H_k^{(e)} H_l^{(e)}) \left\lfloor \frac{dN}{dX} \right\rfloor]\{P\}^{(e)}
\end{aligned} \quad (3\text{-}15)$$

and

$$\begin{aligned}
&\lfloor N \rfloor \{P\}^{(e)} \lfloor N \rfloor \{H\}^{(e)} \\
&= [\lfloor N \rfloor \{P\}^{(e)} \lfloor N \rfloor]\{H\}^{(e)} \\
&= [\sum_{u,v=1}^{r} N_u^{(e)} N_v^{(e)} P_u \lfloor N \rfloor]\{H\}^{(e)}
\end{aligned} \quad (3\text{-}16)$$

So, substitute (3-15) and (3-16) into (3-14), we get

$$\begin{aligned}
&\int_{L^{(e)}} \{Q[(\sum_{s,j,k,l=1}^{r} N_s^{(e)} N_j^{(e)} N_k^{(e)} N_l^{(e)} P_s^{(e)} H_j^{(e)} H_k^{(e)} H_l^{(e)}) \left\lfloor \frac{dN}{dX} \right\rfloor]\{P\}^{(e)}\} \frac{dN_i^{(e)}}{dX} dX \\
&- \int_{L^{(e)}} (\Lambda_x [\sum_{u,v=1}^{r} N_u^{(e)} N_v^{(e)} P_u]\{H\}^{(e)} \lfloor N \rfloor) \frac{dN_i^{(e)}}{dX} dX = F_i
\end{aligned} \quad (3\text{-}17)$$

Further more, we can rewrite (3-17) as

$$\begin{aligned}
&\int_{L^{(e)}} \{Q[(\sum_{s,j,k,l=1}^{r} N_s^{(e)} N_j^{(e)} N_k^{(e)} N_l^{(e)} P_s^{(e)} H_j^{(e)} H_k^{(e)} H_l^{(e)}) \left\lfloor \frac{dN}{dX} \right\rfloor] \frac{dN_i^{(e)}}{dX} dX \}\{P\}^{(e)} \\
&- \int_{L^{(e)}} \{\Lambda_x [\sum_{u,v=1}^{r} N_u^{(e)} N_v^{(e)} P_u]\lfloor N \rfloor] \frac{dN_i^{(e)}}{dX} dX \}\{H\}^{(e)} = F_i
\end{aligned} \quad (3\text{-}18)$$

Define

$$[K^{iq}_{PH^3}]^{(e)} = \begin{bmatrix} K^{11}_{PH^3} & K^{12}_{PH^3} & \cdot\ \cdot\ \cdot & K^{1r}_{PH^3} \\ K^{21}_{PH^3} & K^{22}_{PH^3} & \cdot\ \cdot\ \cdot & K^{2r}_{PH^3} \\ \cdot & \cdot & \cdot\ \cdot\ \cdot & \cdot \\ \cdot & \cdot & \cdot\ \cdot\ \cdot & \cdot \\ \cdot & \cdot & \cdot\ \cdot\ \cdot & \cdot \\ K^{r1}_{PH^3} & K^{r2}_{PH^3} & \cdot\ \cdot\ \cdot & K^{rr}_{PH^3} \end{bmatrix} \tag{3-19}$$

and

$$[K^{iq}_{P}]^{(e)} = \begin{bmatrix} K^{11}_{P} & K^{12}_{P} & \cdot\ \cdot\ \cdot & K^{1r}_{P} \\ K^{21}_{P} & K^{22}_{P} & \cdot\ \cdot\ \cdot & K^{2r}_{P} \\ \cdot & \cdot & \cdot\ \cdot\ \cdot & \cdot \\ \cdot & \cdot & \cdot\ \cdot\ \cdot & \cdot \\ \cdot & \cdot & \cdot\ \cdot\ \cdot & \cdot \\ K^{r1}_{P} & K^{r2}_{P} & \cdot\ \cdot\ \cdot & K^{rr}_{P} \end{bmatrix} \tag{3-20}$$

In Eq. (3-19) and Eq. (3-20),

$$K^{iq}_{PH^3} = \int_{L^{(e)}} \{Q[(\sum_{s,j,k,l=1}^{r} N_s^{(e)} N_j^{(e)} N_k^{(e)} N_l^{(e)} P_s^{(e)} H_j^{(e)} H_k^{(e)} H_l^{(e)}) \left\lfloor \frac{dN}{dX} \right\rfloor] \frac{dN_i^{(e)}}{dX} dX\} \tag{3-21}$$

$$K^{iq}_{P} = \int_{L^{(e)}} \{\Lambda_x [\sum_{u,v=1}^{r} N_u^{(e)} N_v^{(e)} P_u] \lfloor N \rfloor] \frac{dN_i^{(e)}}{dX} dX\} \{H\}^{(e)} \tag{3-22}$$

Substitute (3-19) and (3-20) into (3-18), we get

$$[K^{iq}_{PH^3}]^{(e)} \{P\}^{(e)} - [K^{iq}_{P}]^{(e)} \{H\}^{(e)} = [F_R]^{(e)} \tag{3-23}$$

where

$$[F_R]^{(e)} = [F_1 \quad F_2 \quad . \ . \ . \quad F_r]^T \tag{3-24}$$

The pressure at the boundary of the air bearing is equal to the ambient pressure.

3.1.2 Finite Element Matrix for Cantilever

In this section, the derivation of finite element matrix of cantilever will be carried out. Firstly, the governing equation of the cantilever will be introduced. Then the derivation of the finite element matrix for cantilever in the local coordinate system is derived. To unify the finite element matrix of the cantilever in the same coordinate system as the finite element matrix of the air bearing, the coordinate system transformation will be carried out at last.

3.1.2.1 Governing Equation of Cantilever

As shown in Figure 3-1, one end of the cantilever is fixed, the other end of it is free. The governing equation for such a cantilever is shown in equation (3-25). Here, we assume that the E and I do not vary along the length of the cantilever. Boundary condition for the cantilever is 1) y(0)=0, and 2) moment about the x axis at x=0 is zero.

$$EI\frac{d^4y}{dx^4} = p(x) \tag{3-25}$$

E, Young's Modulus

I, Moment of inertia

p, pressure acted on the cantilever

x,y, the coordinates

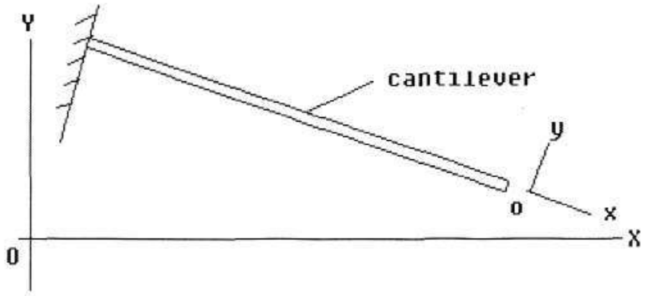

Fig. 3-2 Cantilever in local coordinate system oxy and in global coordinate system OXY

3.1.2.2 Nondimensional of the Governing Equation for Cantilever

We select the L_0 and p_a as the stand length and stand pressure, here L_0 is the length of the cantilever, p_a is the ambient pressure. We also define two constant values $E_0 = 1GP_a, I_0 = 1Kg \cdot m^2$, so we can define $\bar{x} = x / L_0$, $\bar{y} = y / L_0$, $P = p / p_a$, $\bar{E} = E / E_0$, $\bar{I} = I / I_0$. Using these transformations, equation (3-25) becomes

$$\overline{EI}\frac{d^4\bar{y}}{dX} = P(\bar{x}) \tag{3-26}$$

3.1.2.3 Finite Element Matrix of Cantilever

In the local coordinate system, we assume $\bar{y}^a$ and $\bar{P}^a$ are the solutions of equation (3-26). Using the Galerkin method, we get

$$\int_L (\overline{EI}\frac{d^4\bar{y}^a}{dX^4} - \bar{P}^a)N(\bar{x})d\bar{x} = 0 \tag{3-27}$$

Equation (3-27) is applicable to the whole domain, it also holds for each element, so we get

$$\int_{L^{(e)}} [\overline{EI}\frac{d^4 y^{(e)}}{dX^4} - P^{(e)}] N_i^{(e)} d\bar{x} = 0 \tag{3-28}$$

where,

$$y^{(e)} = \sum_{i=1}^{r} N_i^{(e)} y_i = \lfloor N \rfloor \{y\}^{(e)} \tag{3-29}$$

$$P^{(e)} = \sum_{i=1}^{r} N_i^{(e)} P_i = \lfloor N \rfloor \{P\}^{(e)} \tag{3-30}$$

$$\{y\}^{(e)} = [y_1 \;\; y_2 \;\; \cdots \;\; y_r]^T \tag{3-31}$$

$$\{P\}^{(e)} = [P_1 \;\; P_2 \;\; \ldots \;\; P_r]^T \tag{3-32}$$

From Eq. (3-28), we get

$$\int_{L^{(e)}} \overline{EI}\frac{d^4 y^{(e)}}{dX^4} N_i^{(e)} dX - \int_{L^{(e)}} P^{(e)} N_i^{(e)} dX = 0 \tag{3-33}$$

Integrating Eq. (3-33) by parts, we get

$$\int_{L^{(e)}} \overline{EI}\left\lfloor \frac{d^3 N^{(e)}}{dX^3} \right\rfloor \{y\}^{(e)} \frac{dN_i^{(e)}}{dX} dX + \int_{L^{(e)}} \lfloor N \rfloor \{P\}^{(e)} N_i^{(e)} dX = \frac{d^3 y^{(e)}}{dX^3} N_i^{(e)} \Big|_{L^{(e)}} \tag{3-34}$$

We can rewrite Eq. (3-34) as

$$\int_{L^{(e)}} [\overline{EI}\left\lfloor \frac{d^3 N^{(e)}}{dX^3} \right\rfloor \frac{dN_i^{(e)}}{dX} dX]\{y\}^{(e)} + \int_{L^{(e)}} [\lfloor N \rfloor N_i^{(e)} dX]\{P\}^{(e)} = \frac{d^3 y^{(e)}}{dX^3} N_i^{(e)} \Big|_{L^{(e)}} \tag{3-35}$$

Define

$$\{F\}^{(e)} = [F_B^1 \;\; F_B^2 \;\; \ldots F_B^r]^T \tag{3-36}$$

$$F_B^i = \overline{EI}\frac{d^3 y}{dX^3} N_i^{(e)} \Big|_{L^{(e)}} \tag{3-37}$$

$$[K_{yB}]^{(e)} = \begin{bmatrix} K_{yB}^{11} & K_{yB}^{12} & . & . & . & K_{yB}^{1r} \\ K_{yB}^{21} & K_{yB}^{22} & . & . & . & K_{yB}^{2r} \\ . & . & . & . & . & . \\ . & . & . & . & . & . \\ . & . & . & . & . & . \\ K_{yB}^{r1} & K_{yB}^{r2} & . & . & . & K_{yB}^{rr} \end{bmatrix} \tag{3-38}$$

$$[K_{PB}]^{(e)} = \begin{bmatrix} K_{PB}^{11} & K_{PB}^{12} & . & . & . & K_{PB}^{1r} \\ K_{PB}^{21} & K_{PB}^{22} & . & . & . & K_{PB}^{2r} \\ . & . & . & . & . & . \\ . & . & . & . & . & . \\ . & . & . & . & . & . \\ K_{PB}^{r1} & K_{PB}^{r2} & . & . & . & K_{PB}^{rr} \end{bmatrix} \tag{3-39}$$

$$K_{yB}^{iq} = \overline{EI} \int_{L^{(e)}} \left\lfloor \frac{d^3 N^{(e)}}{dX^3} \right\rfloor \frac{dN_i^{(e)}}{dX} dX \tag{3-40}$$

$$K_{PB}^{iq} = \int_{L^{(e)}} \lfloor N \rfloor N_i^{(e)} dX \tag{3-41}$$

i=1,2,…,r;

q=1,2,…,r;

Using equation (3-36) and (3-37), the equation (3-33) can be rewritten as

$$[K_{yB}]^{(e)}\{y\}^{(e)} + [K_{PB}]^{(e)}\{P\}^{(e)} = \{F_B\}^{(e)} \tag{3-42}$$

3.1.2.4 Transformation of Cantilever Element Matrix from Local Coordinate System *oxy* to Global System *OXY*

Now, we will transform the element matrix of equation (3-42) from local coordinate system oxy to the common global coordinate system *OXY*. From the Figure 3-3 shown as below, we can get equation (3-43) shown as below.

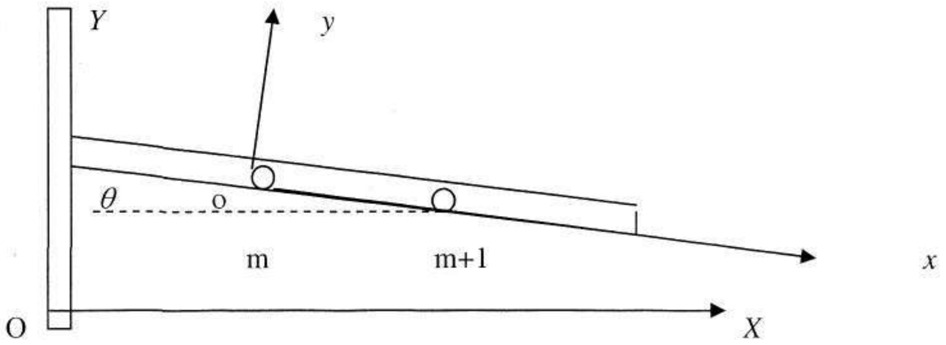

Fig. 3-3 Cantilever in local coordinates system and global coordinates system

$$y = \Delta X \sin\theta + \Delta Y \cos\theta \tag{3-43}$$

In each element, we have

$$y_1 = \Delta X_1 \sin\theta + \Delta Y_1 \cos\theta \tag{3-44}$$

$$y_2 = \Delta X_2 \sin\theta + \Delta Y_2 \cos\theta \tag{3-45}$$

$$\cdots$$

$$y_r = \Delta X_r \sin\theta + \Delta Y_r \cos\theta \tag{3-46}$$

Here, we define

$$\{y\}^{(e)} = [y_1 \;\; y_2 \;\; \cdots y_r]^T \tag{3-47}$$

$$[R]^{(e)}_{Temp} = \begin{bmatrix} \sin\theta & \cos\theta & 0 & 0 & . & . & . & 0 & 0 \\ 0 & 0 & \sin\theta & \cos\theta & . & . & . & 0 & 0 \\ . & . & . & . & . & . & . & . & . \\ . & . & . & . & . & . & . & . & . \\ . & . & . & . & . & . & . & . & . \\ 0 & 0 & 0 & 0 & . & . & . & \sin\theta & \cos\theta \end{bmatrix} \tag{3-48}$$

$$\begin{Bmatrix} \Delta X \\ \Delta Y \end{Bmatrix}^{(e)} = \{\Delta X_1 \;\; \Delta Y_1 \;\; \Delta X_2 \;\; \Delta Y_2 \;\; . \;\; . \;\; . \;\; \Delta X_r \;\; \Delta Y_r\}^T \tag{3-49}$$

So equation (3-47) can be rewritten as

$$\{y\}^{(e)} = [R]^{(e)}_{Temp} \begin{Bmatrix} \Delta X \\ \Delta Y \end{Bmatrix}^{(e)} \tag{3-50}$$

For the node m in an element, we can get its coordinate in OXY before deformation as

$$Y^{ori}_m = H_0 - X_m tg\theta_m \tag{3-51}$$

When the air pressure is acting on the cantilever, the cantilever will deform, and the coordinate of the node m in OXY becomes

$$Y_m = Y^{ori}_m + \Delta Y_m = H_0 - X_m tg\theta_m + \Delta Y_m \tag{3-52}$$

So from m=1 to m=r we have

$$Y_1 = H_0 - X_1 tg\theta_1 + \Delta Y_1 \tag{3-53}$$

$$Y_2 = H_0 - X_2 tg\theta_2 + \Delta Y_2 \tag{3-54}$$

.

.

.

$$Y_r = H_0 - X_r tg\theta_r + \Delta Y_r \tag{3-55}$$

θ_r is the angle between each element and the X direction, which can be calculated as

$$tg\theta_r = (H_{r+1} - H_r)/(X_{r+1} - X_r) \tag{3-56}$$

From (3-53), (3-54) and (3-55) we have

$$\begin{aligned} \Delta Y_1 &= Y_1 - H_0 + X_1 tg\theta_1 \\ \Delta Y_2 &= Y_2 - H_0 + X_2 tg\theta_2 \\ &. \\ &. \\ &. \\ \Delta Y_r &= Y_r - H_0 + X_r tg\theta_r \end{aligned} \tag{3-57}$$

As the Y coordinate has the same value as the flight height H, we can let Y=H. So $Y_1 = H_1,\ Y_2 = H_2, \ldots, Y_r = H_r$, then (3-57) can be rewritten as

$$\begin{aligned} \Delta Y_1 &= H_1 - H_0 + X_1 tg\theta_1 \\ \Delta Y_2 &= H_2 - H_0 + X_2 tg\theta_2 \\ &. \\ &. \\ &. \\ \Delta Y_r &= H_r - H_0 + X_r tg\theta_r \end{aligned} \tag{3-58}$$

We define

$$\{\Delta Y\}^{(e)} = [\Delta Y_1\ \ \Delta Y_2\ \ \ldots \Delta Y_r]^T \tag{3-59}$$

$$\{H\}^{(e)} = [H_1\ \ H_2\ \ \ldots H_r]^T \tag{3-60}$$

$$\{H_c\} = [H_0\ H_0 \cdots H_o]^T \quad (\text{r} \quad H_0 \text{ in the column}) \tag{3-61}$$

$$\{X_\theta\}^{(e)} = [X_1 tg\theta \quad X_2 tg\theta_2\ \ \ldots X_r tg\theta_r]^T \tag{3-62}$$

So equation (3-58) can be rewritten as

$$\{\Delta Y\}^{(e)} = \{H\}^{(e)} + \{X_\theta\}^{(e)} - \{H_c\} \tag{3-63}$$

Based on the transformation method introduced by Huebrner [63], equation (3-42) can be rewritten as

$$[R]_{Temp}^{(e)^T}[K_{yB}]^{(e)}[R]_{Temp}^{(e)}\begin{Bmatrix}\Delta X \\ \Delta Y\end{Bmatrix}^{(e)} + [R]_{Temp}^{(e)^T}\begin{Bmatrix}P_X \\ P_Y\end{Bmatrix}_{Temp}^{(e)}[R]_{Temp}^{(e)} = [R]_{Temp}^{(e)^T}\{F_B\}^{(e)} \tag{3-64}$$

Here, P_X , P_Y is the pressure in X and Y direction.

Define

$$\begin{aligned} [K_{yB}]_{global}^{Temp} &= [R]_{Temp}^{(e)^T}[K_{yB}]^{(e)}[R]_{Temp}^{(e)} \\ [K_{PB}]_{global}^{Temp} &= [R]_{Temp}^{(e)^T}[K_{PB}]^{(e)}[R]_{Temp}^{(e)} \\ \{F_B\}_{global}^{Temp} &= [R]_{Temp}^{(e)^T}\{F_B\}^{(e)} \end{aligned} \tag{3-65}$$

And

$$[K_{yB}]^{Temp}_{global} =$$

$$\begin{bmatrix}
\mathrm{K}^{11}_{\mathrm{gloX}} & \mathrm{K}^{11}_{\mathrm{gloY}} & \mathrm{K}^{12}_{\mathrm{gloX}} & \mathrm{K}^{12}_{\mathrm{gloY}} & \cdot\;\cdot\;\cdot & \mathrm{K}^{1(r-1)}_{\mathrm{gloX}} & \mathrm{K}^{1(r-1)}_{\mathrm{gloY}} & \mathrm{K}^{1(r)}_{\mathrm{gloX}} & \mathrm{K}^{1(r)}_{\mathrm{gloY}} \\
\mathrm{K}^{21}_{\mathrm{gloX}} & \mathrm{K}^{21}_{\mathrm{gloY}} & \mathrm{K}^{22}_{\mathrm{gloX}} & \mathrm{K}^{22}_{\mathrm{gloY}} & \cdot\;\cdot\;\cdot & \mathrm{K}^{2(r-1)}_{\mathrm{gloX}} & \mathrm{K}^{2(r-1)}_{\mathrm{gloY}} & \mathrm{K}^{2(r)}_{\mathrm{gloX}} & \mathrm{K}^{2(r)}_{\mathrm{gloY}} \\
\mathrm{K}^{31}_{\mathrm{gloX}} & \mathrm{K}^{31}_{\mathrm{gloY}} & \mathrm{K}^{32}_{\mathrm{gloX}} & \mathrm{K}^{32}_{\mathrm{gloY}} & \cdot\;\cdot\;\cdot & \mathrm{K}^{3(r-1)}_{\mathrm{gloX}} & \mathrm{K}^{3(r-1)}_{\mathrm{gloY}} & \mathrm{K}^{3(r)}_{\mathrm{gloX}} & \mathrm{K}^{3(r)}_{\mathrm{gloY}} \\
\mathrm{K}^{41}_{\mathrm{gloX}} & \mathrm{K}^{41}_{\mathrm{gloY}} & \mathrm{K}^{42}_{\mathrm{gloX}} & \mathrm{K}^{42}_{\mathrm{gloY}} & \cdot\;\cdot\;\cdot & \mathrm{K}^{4(r-1)}_{\mathrm{gloX}} & \mathrm{K}^{4(r-1)}_{\mathrm{gloY}} & \mathrm{K}^{4(r)}_{\mathrm{gloX}} & \mathrm{K}^{4(r)}_{\mathrm{gloY}} \\
\cdot & \cdot & \cdot & \cdot & \cdot\;\cdot\;\cdot & \cdot & \cdot & \cdot & \cdot \\
\cdot & \cdot & \cdot & \cdot & \cdot\;\cdot\;\cdot & \cdot & \cdot & \cdot & \cdot \\
\cdot & \cdot & \cdot & \cdot & \cdot\;\cdot\;\cdot & \cdot & \cdot & \cdot & \cdot \\
\mathrm{K}^{(2r-3)1}_{\mathrm{gloX}} & \mathrm{K}^{(2r-3)1}_{\mathrm{glYo}} & \mathrm{K}^{(2r-3)2}_{\mathrm{gloX}} & \mathrm{K}^{(2r-3)2}_{\mathrm{gloY}} & \cdot\;\cdot\;\cdot & \mathrm{K}^{(2r-3)(r-1)}_{\mathrm{gloX}} & \mathrm{K}^{(2r-3)(r-1)}_{\mathrm{gloY}} & \mathrm{K}^{(2r-3)(r)}_{\mathrm{gloX}} & \mathrm{K}^{(2r-3)(r)}_{\mathrm{gloY}} \\
\mathrm{K}^{(2r-2)1}_{\mathrm{gloX}} & \mathrm{K}^{(2r-2)1}_{\mathrm{gloY}} & \mathrm{K}^{(2r-2)2}_{\mathrm{gloX}} & \mathrm{K}^{(2r-2)2}_{\mathrm{gloY}} & \cdot\;\cdot\;\cdot & \mathrm{K}^{(2r-2)(r-1)}_{\mathrm{gloX}} & \mathrm{K}^{(2r-2)(r-1)}_{\mathrm{gloY}} & \mathrm{K}^{(2r-2)(r)}_{\mathrm{gloX}} & \mathrm{K}^{(2r-2)(r)}_{\mathrm{gloY}} \\
\mathrm{K}^{(2r-1)1}_{\mathrm{gloX}} & \mathrm{K}^{(2r-1)1}_{\mathrm{gloY}} & \mathrm{K}^{(2r-1)2}_{\mathrm{gloX}} & \mathrm{K}^{(2r-1)2}_{\mathrm{gloY}} & \cdot\;\cdot\;\cdot & \mathrm{K}^{(2r-1)(r-1)}_{\mathrm{gloX}} & \mathrm{K}^{(2r-1)(r-1)}_{\mathrm{gloY}} & \mathrm{K}^{(2r-1)(r)}_{\mathrm{gloX}} & \mathrm{K}^{(2r-1)(r)}_{\mathrm{gloY}} \\
\mathrm{K}^{(2r)1}_{\mathrm{gloX}} & \mathrm{K}^{(2r)1}_{\mathrm{gloY}} & \mathrm{K}^{(2r)2}_{\mathrm{gloX}} & \mathrm{K}^{(2r)2}_{\mathrm{gloY}} & \cdot\;\cdot\;\cdot & \mathrm{K}^{(2r)(r-1)}_{\mathrm{gloX}} & \mathrm{K}^{(2r)(r-1)}_{\mathrm{gloY}} & \mathrm{K}^{(2r)(r)}_{\mathrm{gloX}} & \mathrm{K}^{(2r)(r)}_{\mathrm{gloY}}
\end{bmatrix} \tag{3-66}$$

$$[K_{PB}]^{Temp}_{global} =$$

$$\begin{bmatrix}
\mathrm{K}^{11}_{\mathrm{GPBX}} & \mathrm{K}^{11}_{\mathrm{GPBY}} & \mathrm{K}^{12}_{\mathrm{GPBX}} & \mathrm{K}^{12}_{\mathrm{GPBY}} & \cdot\;\cdot\;\cdot & \mathrm{K}^{1(r-1)}_{\mathrm{GPBX}} & \mathrm{K}^{1(r-1)}_{\mathrm{GPBY}} & \mathrm{K}^{1(r)}_{\mathrm{GPBX}} & \mathrm{K}^{1(r)}_{\mathrm{GPBY}} \\
\mathrm{K}^{21}_{\mathrm{GPBX}} & \mathrm{K}^{21}_{\mathrm{GPBY}} & \mathrm{K}^{22}_{\mathrm{GPBX}} & \mathrm{K}^{22}_{\mathrm{GPBY}} & \cdot\;\cdot\;\cdot & \mathrm{K}^{2(r-1)}_{\mathrm{GPBX}} & \mathrm{K}^{2(r-1)}_{\mathrm{GPBY}} & \mathrm{K}^{2(r)}_{\mathrm{GPBX}} & \mathrm{K}^{2(r)}_{\mathrm{GPBY}} \\
\mathrm{K}^{31}_{\mathrm{GPBX}} & \mathrm{K}^{31}_{\mathrm{GPBY}} & \mathrm{K}^{32}_{\mathrm{GPBX}} & \mathrm{K}^{32}_{\mathrm{GPBY}} & \cdot\;\cdot\;\cdot & \mathrm{K}^{3(r-1)}_{\mathrm{GPBX}} & \mathrm{K}^{3(r-1)}_{\mathrm{GPBY}} & \mathrm{K}^{3(r)}_{\mathrm{GPBX}} & \mathrm{K}^{3(r)}_{\mathrm{GPBY}} \\
\mathrm{K}^{41}_{\mathrm{GPBX}} & \mathrm{K}^{41}_{\mathrm{GPBY}} & \mathrm{K}^{42}_{\mathrm{GPBX}} & \mathrm{K}^{42}_{\mathrm{GPBY}} & \cdot\;\cdot\;\cdot & \mathrm{K}^{4(r-1)}_{\mathrm{GPBX}} & \mathrm{K}^{4(r-1)}_{\mathrm{GPBY}} & \mathrm{K}^{4(r)}_{\mathrm{GPBX}} & \mathrm{K}^{4(r)}_{\mathrm{GPBY}} \\
\cdot & \cdot & \cdot & \cdot & \cdot\;\cdot\;\cdot & \cdot & \cdot & \cdot & \cdot \\
\cdot & \cdot & \cdot & \cdot & \cdot\;\cdot\;\cdot & \cdot & \cdot & \cdot & \cdot \\
\cdot & \cdot & \cdot & \cdot & \cdot\;\cdot\;\cdot & \cdot & \cdot & \cdot & \cdot \\
\mathrm{K}^{(2r-3)1}_{\mathrm{GPBX}} & \mathrm{K}^{(2r-3)1}_{\mathrm{GPBY}} & \mathrm{K}^{(2r-3)2}_{\mathrm{GPBX}} & \mathrm{K}^{(2r-3)2}_{\mathrm{GPBY}} & \cdot\;\cdot\;\cdot & \mathrm{K}^{(2r-3)(r-1)}_{\mathrm{GPBX}} & \mathrm{K}^{(2r-3)(r-1)}_{\mathrm{GPBY}} & \mathrm{K}^{(2r-3)(r)}_{\mathrm{GPBX}} & \mathrm{K}^{(2r-3)(r)}_{\mathrm{GPBY}} \\
\mathrm{K}^{(2r-2)1}_{\mathrm{GPBX}} & \mathrm{K}^{(2r-2)1}_{\mathrm{GPBY}} & \mathrm{K}^{(2r-2)2}_{\mathrm{GPBX}} & \mathrm{K}^{(2r-2)2}_{\mathrm{GPBY}} & \cdot\;\cdot\;\cdot & \mathrm{K}^{(2r-2)(r-1)}_{\mathrm{GPBX}} & \mathrm{K}^{(2r-2)(r-1)}_{\mathrm{GPBY}} & \mathrm{K}^{(2r-2)(r)}_{\mathrm{GPBX}} & \mathrm{K}^{(2r-2)(r)}_{\mathrm{GPBY}} \\
\mathrm{K}^{(2r-1)1}_{\mathrm{GPBX}} & \mathrm{K}^{(2r-1)1}_{\mathrm{GPBY}} & \mathrm{K}^{(2r-1)2}_{\mathrm{GPBX}} & \mathrm{K}^{(2r-1)2}_{\mathrm{GPBY}} & \cdot\;\cdot\;\cdot & \mathrm{K}^{(2r-1)(r-1)}_{\mathrm{GPBX}} & \mathrm{K}^{(2r-1)(r-1)}_{\mathrm{GPBY}} & \mathrm{K}^{(2r-1)(r)}_{\mathrm{GPBX}} & \mathrm{K}^{(2r-1)(r)}_{\mathrm{GPBY}} \\
\mathrm{K}^{(2r)1}_{\mathrm{GPBX}} & \mathrm{K}^{(2r)1}_{\mathrm{GPBY}} & \mathrm{K}^{(2r)2}_{\mathrm{GPBX}} & \mathrm{K}^{(2r)2}_{\mathrm{GPBY}} & \cdot\;\cdot\;\cdot & \mathrm{K}^{(2r)(r-1)}_{\mathrm{GPBX}} & \mathrm{K}^{(2r)(r-1)}_{\mathrm{GPBY}} & \mathrm{K}^{(2r)(r)}_{\mathrm{GPBX}} & \mathrm{K}^{(2r)(r)}_{\mathrm{GPBY}}
\end{bmatrix} \tag{3-67}$$

$$\{F_B\}^{Temp}_{global} = \{F_{B1}\ \ F_{B2}\ F_{B3}\ \ F_{B4}\ \ \ldots F_{B(k-1)}\ \ F_{Bk}\}^T \tag{3-68}$$

k=2r

So equation (3-64) can be rewritten as

$$[K_{yB}]^{Temp}_{global}\begin{Bmatrix}\Delta X \\ \Delta Y\end{Bmatrix}^{(e)} + [K_{PB}]^{Temp}_{global}\begin{Bmatrix}P_X \\ P_Y\end{Bmatrix}^{(e)} = \{F_B\}^{Temp}_{global} \tag{3-69}$$

We can extend equation (3-69) as below,

$$K^{11}_{gloX}\Delta X_1 + K^{11}_{gloY}\Delta Y_1 + K^{12}_{gloX}\Delta X_2 + K^{12}_{gloY}\Delta Y_2 + \ldots + K^{1r}_{gloX}\Delta X_r + K^{1r}_{gloX}\Delta Y_r = F_{B1} \quad (3\text{-}70)$$

$$K^{21}_{gloX}\Delta X_1 + K^{21}_{gloY}\Delta Y_1 + K^{22}_{gloX}\Delta X_2 + K^{22}_{gloY}\Delta Y_2 + \ldots + K^{2r}_{gloX}\Delta X_r + K^{2r}_{gloX}\Delta Y_r = F_{B2} \quad (3\text{-}71)$$

.

.

.

$$K^{(2r)1}_{gloX}\Delta X_1 + K^{(2r)1}_{gloY}\Delta Y_1 + K^{(2r)2}_{gloX}\Delta X_2 + K^{(2r)2}_{gloY}\Delta Y_2 + \ldots + K^{(2r)r}_{gloX}\Delta X_r + K^{(2r)r}_{gloX}\Delta Y_r = F_{B(2r)}$$

(3-72)

In the coupling field problem between the cantilever and the air bearing, the pressure in Y direction and the deformation in Y direction are the only two unknown variables, which will be taken into account. So we can and we will get a set of equations after dealing with equation (3-69). Here

$$\begin{Bmatrix} P_X \\ P_Y \end{Bmatrix}^{(e)}_{Temp} = \{P_{X1} \quad P_{Y1} \quad P_{X2} \quad P_{Y2} \quad . \quad . \quad . \quad P_{XR} \quad P_{YR}\}^T \quad (3\text{-}73)$$

Firstly, equation (3-69) can be extended as (3-74).

$$
\begin{bmatrix}
K^{11}_{gloX} & K^{11}_{gloY} & K^{12}_{gloX} & K^{12}_{gloY} & \cdots & K^{1(r-1)}_{gloX} & K^{1(r-1)}_{gloY} & K^{1(r)}_{gloX} & K^{1(r)}_{gloY} \\
K^{21}_{gloX} & K^{21}_{gloY} & K^{22}_{gloX} & K^{22}_{gloY} & \cdots & K^{2(r-1)}_{gloX} & K^{2(r-1)}_{gloY} & K^{2(r)}_{gloX} & K^{2(r)}_{gloY} \\
K^{31}_{gloX} & K^{31}_{gloY} & K^{32}_{gloX} & K^{32}_{gloY} & \cdots & K^{3(r-1)}_{gloX} & K^{3(r-1)}_{gloY} & K^{3(r)}_{gloX} & K^{3(r)}_{gloY} \\
K^{41}_{gloX} & K^{41}_{gloY} & K^{42}_{gloX} & K^{42}_{gloY} & \cdots & K^{4(r-1)}_{gloX} & K^{4(r-1)}_{gloY} & K^{4(r)}_{gloX} & K^{4(r)}_{gloY} \\
\cdot & \cdot & \cdot & \cdot & \cdots & \cdot & \cdot & \cdot & \cdot \\
\cdot & \cdot & \cdot & \cdot & \cdots & \cdot & \cdot & \cdot & \cdot \\
\cdot & \cdot & \cdot & \cdot & \cdots & \cdot & \cdot & \cdot & \cdot \\
K^{(2r-3)1}_{gloX} & K^{(2r-3)1}_{glYo} & K^{(2r-3)2}_{gloX} & K^{(2r-3)2}_{gloY} & \cdots & K^{(2r-3)(r-1)}_{gloX} & K^{(2r-3)(r-1)}_{gloY} & K^{(2r-3)(r)}_{gloX} & K^{(2r-3)(r)}_{gloY} \\
K^{(2r-2)1}_{gloX} & K^{(2r-2)1}_{gloY} & K^{(2r-2)2}_{gloX} & K^{(2r-2)2}_{gloY} & \cdots & K^{(2r-2)(r-1)}_{gloX} & K^{(2r-2)(r-1)}_{gloY} & K^{(2r-2)(r)}_{gloX} & K^{(2r-2)(r)}_{gloY} \\
K^{(2r-1)1}_{gloX} & K^{(2r-1)1}_{gloY} & K^{(2r-1)2}_{gloX} & K^{(2r-1)2}_{gloY} & \cdots & K^{(2r-1)(r-1)}_{gloX} & K^{(2r-1)(r-1)}_{gloY} & K^{(2r-1)(r)}_{gloX} & K^{(2r-1)(r)}_{gloY} \\
K^{(2r)1}_{gloX} & K^{(2r)1}_{gloY} & K^{(2r)2}_{gloX} & K^{(2r)2}_{gloY} & \cdots & K^{(2r)(r-1)}_{gloX} & K^{(2r)(r-1)}_{gloY} & K^{(2r)(r)}_{gloX} & K^{(2r)(r)}_{gloY}
\end{bmatrix}
\begin{Bmatrix}
\Delta X_1 \\ \Delta Y_1 \\ \Delta X_2 \\ \Delta Y_2 \\ \cdot \\ \cdot \\ \cdot \\ \cdot \\ \Delta X_r \\ \Delta Y_r
\end{Bmatrix}
$$

$$
+
\begin{bmatrix}
K^{11}_{GPBX} & K^{11}_{GPBY} & K^{12}_{GPBX} & K^{12}_{GPBY} & \cdots & K^{1(r-1)}_{GPBX} & K^{1(r-1)}_{GPBY} & K^{1(r)}_{GPBX} & K^{1(r)}_{GPBY} \\
K^{21}_{GPBX} & K^{21}_{GPBY} & K^{22}_{GPBX} & K^{22}_{GPBY} & \cdots & K^{2(r-1)}_{GPBX} & K^{2(r-1)}_{GPBY} & K^{2(r)}_{GPBX} & K^{2(r)}_{GPBY} \\
K^{31}_{GPBX} & K^{31}_{GPBY} & K^{32}_{GPBX} & K^{32}_{GPBY} & \cdots & K^{3(r-1)}_{GPBX} & K^{3(r-1)}_{GPBY} & K^{3(r)}_{GPBX} & K^{3(r)}_{GPBY} \\
K^{41}_{GPBX} & K^{41}_{GPBY} & K^{42}_{GPBX} & K^{42}_{GPBY} & \cdots & K^{4(r-1)}_{GPBX} & K^{4(r-1)}_{GPBY} & K^{4(r)}_{GPBX} & K^{4(r)}_{GPBY} \\
\cdot & \cdot & \cdot & \cdot & \cdots & \cdot & \cdot & \cdot & \cdot \\
\cdot & \cdot & \cdot & \cdot & \cdots & \cdot & \cdot & \cdot & \cdot \\
\cdot & \cdot & \cdot & \cdot & \cdots & \cdot & \cdot & \cdot & \cdot \\
K^{(2r-3)1}_{GPBX} & K^{(2r-3)1}_{GPBY} & K^{(2r-3)2}_{GPBX} & K^{(2r-3)2}_{GPBY} & \cdots & K^{(2r-3)(r-1)}_{GPBX} & K^{(2r-3)(r-1)}_{GPBY} & K^{(2r-3)(r)}_{GPBX} & K^{(2r-3)(r)}_{GPBY} \\
K^{(2r-2)1}_{GPBX} & K^{(2r-2)1}_{GPBY} & K^{(2r-2)2}_{GPBX} & K^{(2r-2)2}_{GPBY} & \cdots & K^{(2r-2)(r-1)}_{GPBX} & K^{(2r-2)(r-1)}_{GPBY} & K^{(2r-2)(r)}_{GPBX} & K^{(2r-2)(r)}_{GPBY} \\
K^{(2r-1)1}_{GPBX} & K^{(2r-1)1}_{GPBY} & K^{(2r-1)2}_{GPBX} & K^{(2r-1)2}_{GPBY} & \cdots & K^{(2r-1)(r-1)}_{GPBX} & K^{(2r-1)(r-1)}_{GPBY} & K^{(2r-1)(r)}_{GPBX} & K^{(2r-1)(r)}_{GPBY} \\
K^{(2r)1}_{GPBX} & K^{(2r)1}_{GPBY} & K^{(2r)2}_{GPBX} & K^{(2r)2}_{GPBY} & \cdots & K^{(2r)(r-1)}_{GPBX} & K^{(2r)(r-1)}_{GPBY} & K^{(2r)(r)}_{GPBX} & K^{(2r)(r)}_{GPBY}
\end{bmatrix}
\begin{Bmatrix}
P_{X1} \\ P_{Y1} \\ P_{X2} \\ P_{Y2} \\ \cdot \\ \cdot \\ \cdot \\ P_{X(r-1)} \\ P_{Y(r-1)} \\ P_{Xr} \\ P_{Yr}
\end{Bmatrix}
$$

$$
= \{F_{B1} \quad F_{B2} \quad \cdots \quad F_{Bk}\}^T \tag{3-74}
$$

Substitute equation (3-63) into (3-74), we have

$$
[K]_{gY}\{\{H\}^{(e)} + \{X_\theta\}^{(e)} - \{H_c\}\} + [K]_{gP}\{P_Y\}^{(e)} = \{F\}_{glo} \tag{3-75}
$$

That is

$$
[K]_{gY}\{H\}^{(e)} + [K]_{gP}\{P_Y\}^{(e)} = \{F\}_{glo} - [K]_{gY}\{\{X_\theta\}^{(e)} - \{H_c\}\} \tag{3-76}
$$

Define

$$
\{F_B\}_G^{(e)} = \{F\}_{glo} - [K]_{gY}\{\{X_\theta\}^{(e)} - \{H_c\}\} \tag{3-77}
$$

So equation (3-76) can be rewritten as

$$[K]_{gY}\{H\}^{(e)} + [K]_{gP}\{P_Y\}^{(e)} = \{F_B\}_G^{(e)} \tag{3-78}$$

Equation (3-78) is the finite element equation for the cantilever in the global coordinate system *OXY*.

3.1.3 Finite Element Matrix for PZT

Figure 3-4 shows the basic configuration of the whole system. The local coordinate system for PZT itself is oxy. The global coordinate system is OXY. Firstly, we derive the finite element matrix in oxy. For computation convenience, the element matrix is needed to be transferred from local coordinate system oxy to global coordinate system OXY. All the derivations for PZT are similar to that for cantilever. Here and after, the cantilever is with one end fixed on the slider body, and the other end is free.

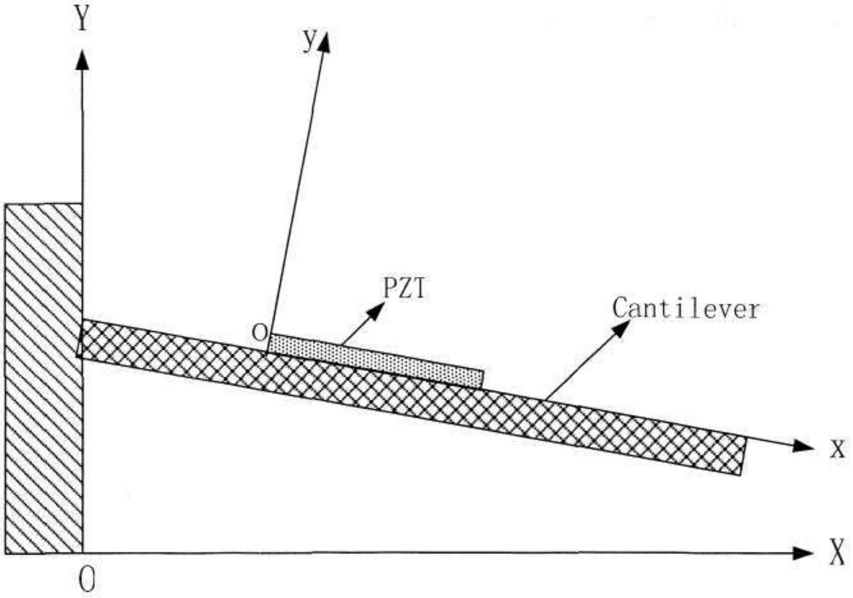

Fig. 3-4 Configuration of whole system

In this session, some basic equations for PZT will be introduced. Then the derivation of the finite element matrix for it in the local coordinate system is derived. To unify the finite element matrix of the PZT in the same coordinate system as the finite element matrix of the air bearing and cantilever, the coordinate system transformation will be carried out at last.

3.1.3.1 Constitutive Equation of PZT

Under small field conditions, the constitutive relations in time domain for a PZT are (IEEE Standard, 1987):

$$D_i = e^{\sigma}_{ij} E_j + d^{d}_{im} \sigma_m \qquad (3\text{-}79)$$

$$\varepsilon_k = d^{c}_{jk} E_j + s^{E}_{km} \sigma_m \qquad (3\text{-}80)$$

These two equations can be written as a matrix form as

$$\begin{bmatrix} D \\ \varepsilon \end{bmatrix} = \begin{bmatrix} e^{\sigma}\, d^{d} \\ d^{e}\, s^{E} \end{bmatrix} \begin{bmatrix} E \\ \sigma \end{bmatrix} \qquad (3\text{-}81)$$

Here, E is the applied electric field, D is the electric displacement, ε is the strain vector, σ is the stress vector. So there are four unknown valuables (E, D, ε and σ) in Equation (3-81), here we only solve the equation in about the vertical direction. Use h and p to substitute ε and σ, Equation (3-81) can be rewritten as

$$\begin{bmatrix} D \\ h \end{bmatrix} = \begin{bmatrix} e^{\sigma}\, d^{d} \\ d^{e}\, s^{E} \end{bmatrix} \begin{bmatrix} E \\ p \end{bmatrix} \qquad (3\text{-}82)$$

Equation (3-82) shows that the PZT material is a coupling material between electrical valuables (E, D) and mechanical valuables (h, p).

3.1.3.2 Finite Element Matrix

Put the PZT in the global coordinate system, and apply Galerkin method to equation (3-82). Assume $\overline{E}$, $\overline{D}$, $\overline{h}$, $\overline{p}$ are the solutions, we have,

$$\int_L [\frac{d}{dx}(\overline{D(x)} - e^{\sigma}\overline{E(x)} - d^{d}\overline{p(x)})]N(x)dx = 0 \tag{3-83}$$

and

$$\int_L [\frac{d}{dx}(\overline{h(x)} - d^{e}\overline{E(x)} - s^{E}\overline{p(x)})]N(x)dx = 0 \tag{3-84}$$

Equation (3-83) and (3-84) are applicable to the whole system, they also hold for each element, so we get

$$\int_{L^{(e)}} [\frac{d}{dx}(D^{(e)}(x) - e^{\sigma}E^{(e)}(x) - d^{d}p^{(e)}(x))]N_i^{(e)}(x)dx = 0\text{, i=1, 2, 3 …r} \tag{3-85}$$

$$\int_{L^{(e)}} [\frac{d}{dx}(\overline{h^{(e)}(x)} - d^{e}\overline{E^{(e)}(x)} - s^{E}\overline{p^{(e)}(x)})]N_i^{(e)}(x)dx = 0\text{, i=1, 2, 3 …r} \tag{3-86}$$

Here,

$$D^{(e)} = \sum_{i=1}^{r} N_i^{(e)} D_i = \lfloor N \rfloor \{D\}^{(e)} \tag{3-87}$$

$$E^{(e)} = \sum_{i=1}^{r} N_i^{(e)} E_i = \lfloor N \rfloor \{E\}^{(e)} \tag{3-88}$$

$$h^{(e)} = \sum_{i=1}^{r} N_i^{(e)} h_i = \lfloor N \rfloor \{h\}^{(e)} \tag{3-89}$$

$$p^{(e)} = \sum_{i=1}^{r} N_i^{(e)} p_i = \lfloor N \rfloor \{p\}^{(e)} \tag{3-90}$$

$$\{D\}^{(e)} = [D_1\ D_2\ \dots\ D_r]^T \tag{3-91}$$

$$\{E\}^{(e)} = [E_1\ E_2\ \dots\ E_r]^T \tag{3-92}$$

$$\{h\}^{(e)} = [h_1\ h_2\ \dots\ h_r]^T \tag{3-93}$$

$$\{p\}^{(e)} = [p_1\ p_2\ \cdots\ p_r]^T \tag{3-94}$$

Using the same method of derivation and transformation for the cantilever element matrices, the final element matrices for the PZT are

$$\begin{aligned} [K]_D\{D\}^{(e)} + [K]_{E1}\{E\}^{(e)} + [K]_{P1}\{P\}^{(e)} = \{F_1\}^{(e)} \\ [K]_H\{H\}^{(e)} + [K]_{E2}\{E\}^{(e)} + [K]_{P2}\{P\}^{(e)} = \{F_2\}^{(e)} \end{aligned} \tag{3-95}$$

Or

$$[K]_D\{D\}^{(e)}+[K]_H\{H\}^{(e)}+([K]_{E1}+[K]_{E2})\{E\}^{(e)}+([K]_{P1}+[K]_{p2})\{P\}^{(e)}=\{F_1\}^{(e)}+\{F_2\}^{(e)} \tag{3-96}$$

where

$$D=2\pi\omega I \tag{3-97}$$

Here, I is the output current of PZT, ω is the frequency of current. So equation (3-96) can be also rewritten (3-98), which is reference to the global coordinate system.

$$\begin{aligned}&2\pi\omega[K]_D\{I\}^{(e)}+[K]_H\{H\}^{(e)}+([K]_{E1}+[K]_{E2})\{E\}^{(e)}+([K]_{P1}+[K]_{p2})\{P\}^{(e)}\\&=\{F_1\}^{(e)}+\{F_2\}^{(e)}\end{aligned} \tag{3-98}$$

Up to now, we have derived the element matrix for cantilever, air bearing and PZT respectively, as Equation (3-23), (3-78) and (3-98). In the following sections, the coupling field problem is discussed and the solution schemes are shown.

3.2 Solution Schemes

The equation (3-23), (3-78) and (3-98) are written again as below,

$$[K_{PH^3}^{iq}]^{(e)}\{P\}^{(e)}-[K_P^{iq}]^{(e)}\{H\}^{(e)}=[F_R]^{(e)} \tag{3-99}$$

$$[K]_{gY}\{H\}^{(e)}+[K]_{gP}\{P\}^{(e)}=\{F_B\}_G^{(e)} \tag{3-100}$$

$$\begin{aligned}&2\pi\omega[K]_D\{I\}^{(e)}+[K]_H\{H\}^{(e)}+([K]_{E1}+[K]_{E2})\{E\}^{(e)}+([K]_{P1}+[K]_{p2})\{P\}^{(e)}\\&=\{F_1\}^{(e)}+\{F_2\}^{(e)}\end{aligned} \tag{3-101}$$

From these matrix equations, it is obviously seen that the any variation of the air bearing will cause variation on the cantilever and PZT film simultaneously. At the same time, any variations of the cantilever or PZT film will also cause the air bearing to be changed into another state. Air bearing, cantilever and PZT film are internally affected each other and they consist of a whole system which includes three coupling fields inside. It is required for us to solve the above three equations simultaneously to get an accurate result of a specified state for the system. Based on these finite element matrices, an element with three degrees P, H and I are fabricated to model the system. This element satisfies equation (3-99), (3-100) and (3-101) simultaneously. For solving the linear matrix equations, Newton-Raphson iteration method is used. The FE codes were written majorly in MATLAB language, and some of the codes were written in Fortran language. The second-order line element with 3 nodes is used as the cantilever element. Figure 3-5 shows the flow chart of the finite element program. At the beginning, the known parameters are input to the FE program. The known parameters include dimensions, material properties of cantilever and PZT, fluid related parameters for air bearing etc. The detailed mechanical parameters are different from case to case and will be given separately in respective case study. The mean free path of air is 63.5nm. Table 3-1 shows the material properties of PZT. The parameters in this table will be used throughout all our theoretical analysis in this thesis.

Table 3-1 Material properties of PZT (Fuji ceramic, C-601)

$E_{11}=E_{22}(N/m^2)$	$E_{33}(N/m^2)$	$v_{12}=v_{23}=v_{31}$	$\overline{\rho}(kg/m^3)$
6.7×10^{10}	5.0×10^{10}	0.33	7800

****

$d_{31}(C/N)$	$d_{33}(C/N)$	$d_{15}(C/N)$	$Z_1(F/m)$	$Z_2(F/m)$
-210×10^{-12}	500×10^{-12}	730×10^{-12}	2.12×10^{-8}	2.03×10^{-8}

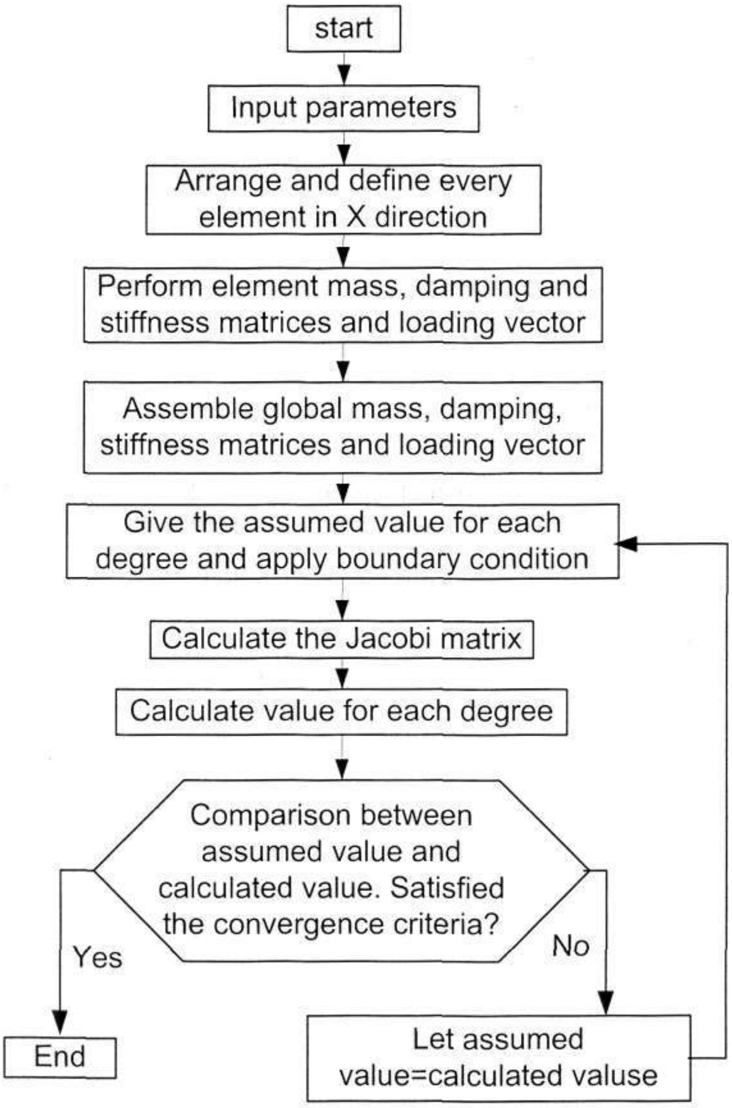

Fig. 3-5 Flow chart of program

3.3 Verification of FE Program

In the above sections, the derivations of finite element matrices and the solution scheme have been shown. Being lack of existing research to solve the coupling field problem among PZT, cantilever and air bearing, it is hard to compare existing results with the results calculated from our FE program to validate its correctness. The only way is to use the FE program to solve the simplified models and compare the calculated results from our own developed FE program with existing results from CML air bearing design program to verify its correctness.

CML air bearing design program was developed by the Computer Mechanics Laboratory, in the department of Mechanical Engineering of University of California, Berkeley. It is currently widely used in the hard disk drive industry for slider design. So the pressure results from CML program is used here for our comparisons. As we know in the slider design, only the pressure on the air bearing surface plays important role. Look at part (A) of Figure 3-6, it shows a simple but typical 3-rail slider design. The pressure distribution along the slider surface shown in part (A) with inclined line will be obtained by CML, and the pressure distribution along the PZT cantilever will be obtained by our own FE program. Two points are needed to be pointed out here are, 1) in the CML program, the obtained pressure varies along the slider width direction, which is the actual behavior in hard disk drives, and 2) the pressure assumes to be kept same along the cantilever width direction. These assumptions would hold as the current slider of hard disk drive flies at a nano-scale. Under such a low flying height of PZT cantilever, the pressure variations along the cantilever width direction are less than 1%, i.e. the pressure along the edge of cantilever is about 1% less than that along the center line of cantilever. This small variation will be ignored during the slider design in current HDD industry. So, in our study, the pressure along the center line AB and that along center line CD are compared and analyzed. These comparisons will be introduced in detailed in the following sections. Moreover, in CML, the air bearing could be modeled as 1st order or 2nd order or F-K Boltzmann slip model. But in the real design, the air bearing F-K Boltzmann model is frequently used especially for low flying height design, which is also adopted as the slider design standard in HDD industry. The General setup and Run setup for the CML simulation are shown in figure 3-7 and 3-8 respectively. Figure 3-8 shows a dialog with the disk rotation speed in RPM (round per minutes) and related air parameters. In our analysis, the ambient pressure is 10325 Pa, the mean free path (MFP) of air is 63.5 nm and the viscosity of air is $1.806\times10^{-5}\,Ns/m^2$. For more detailed information on CML simulation package, we could check with its latest version help files from computer mechanics laboratory of U.C. Berkeley.

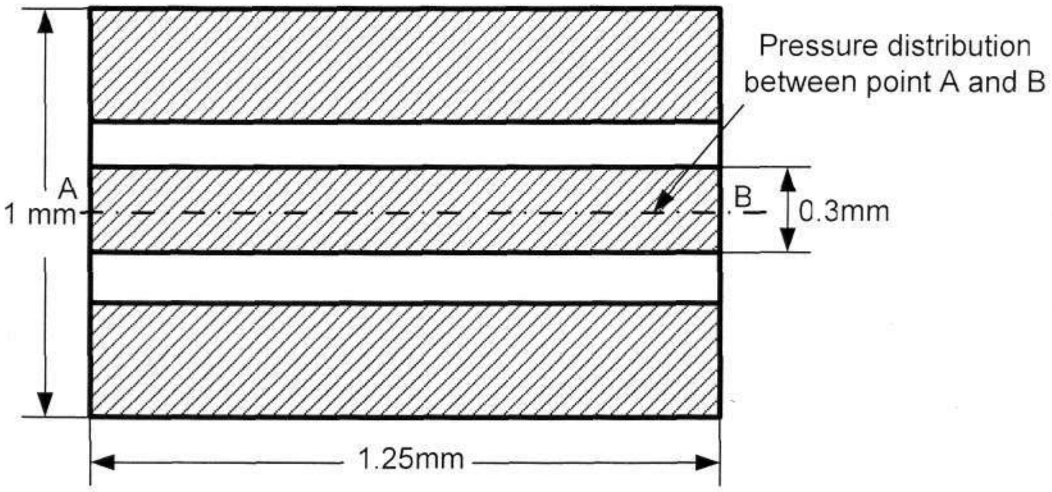

(A) 3-rail slider design

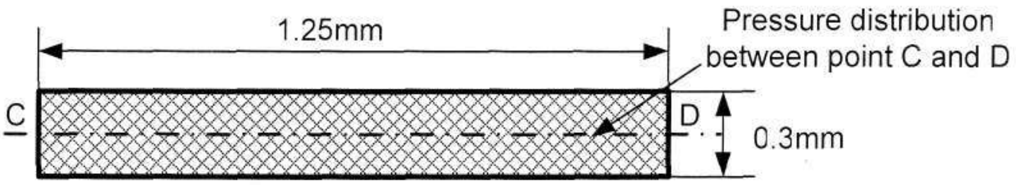

(B) PZT cantilever flying above disk surface, with predetermined flying height

Fig. 3-6 Sketch of a traditional 3-rail slider design and a PZT cantilever

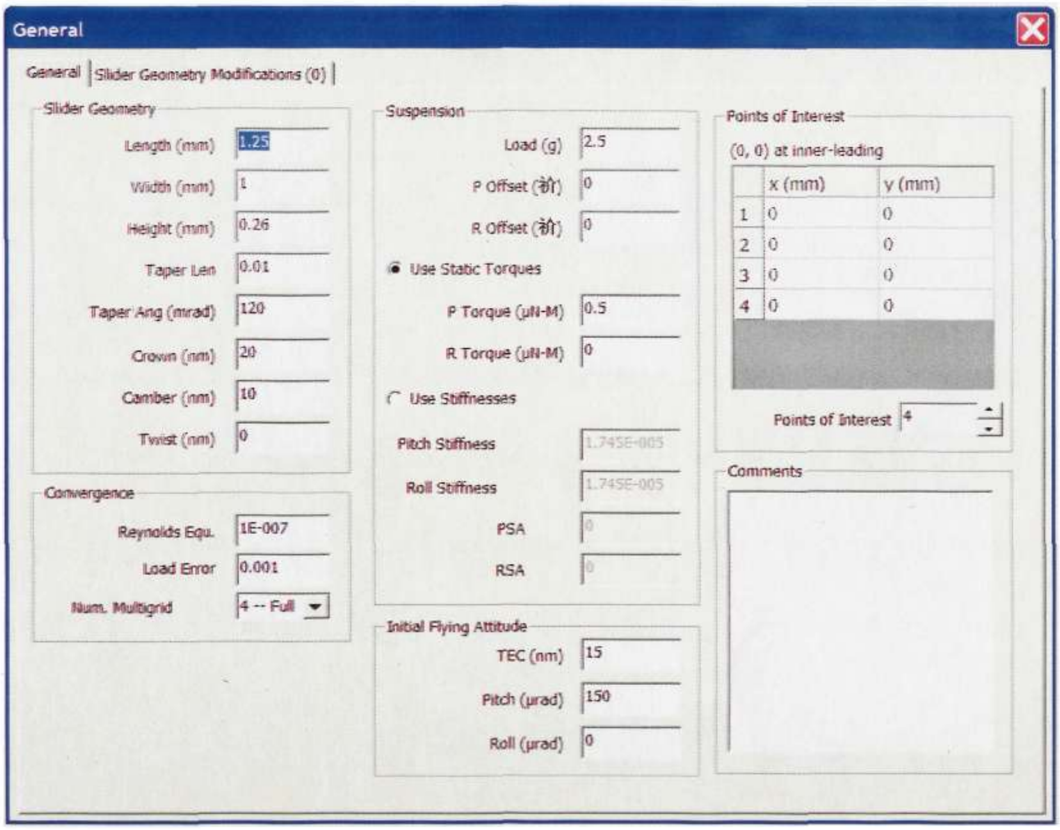

Slider Geometry
Length (mm) 1.25
Width (mm) 1
Height (mm) 0.26
Taper Len 0.01
Taper Ang (mrad) 120
Crown (nm) 20
Camber (nm) 10
Twist (nm) 0

Convergence
Reynolds Equ. 1E-007
Load Error 0.001
Num. Multigrid 4 -- Full

Suspension
Load (g) 2.5
P Offset ([illegible]) 0
R Offset ([illegible]) 0
● Use Static Torques
P Torque (µN-M) 0.5
R Torque (µN-M) 0
○ Use Stiffnesses
Pitch Stiffness 1.745E-005
Roll Stiffness 1.745E-005
PSA 0
RSA 0

Initial Flying Attitude
TEC (nm) 15
Pitch (µrad) 150
Roll (µrad) 0

Points of Interest
(0, 0) at inner-leading

	x (mm)	y (mm)
1	0	0
2	0	0
3	0	0
4	0	0

Points of Interest 4

Comments

Fig. 3-7 CML General setup

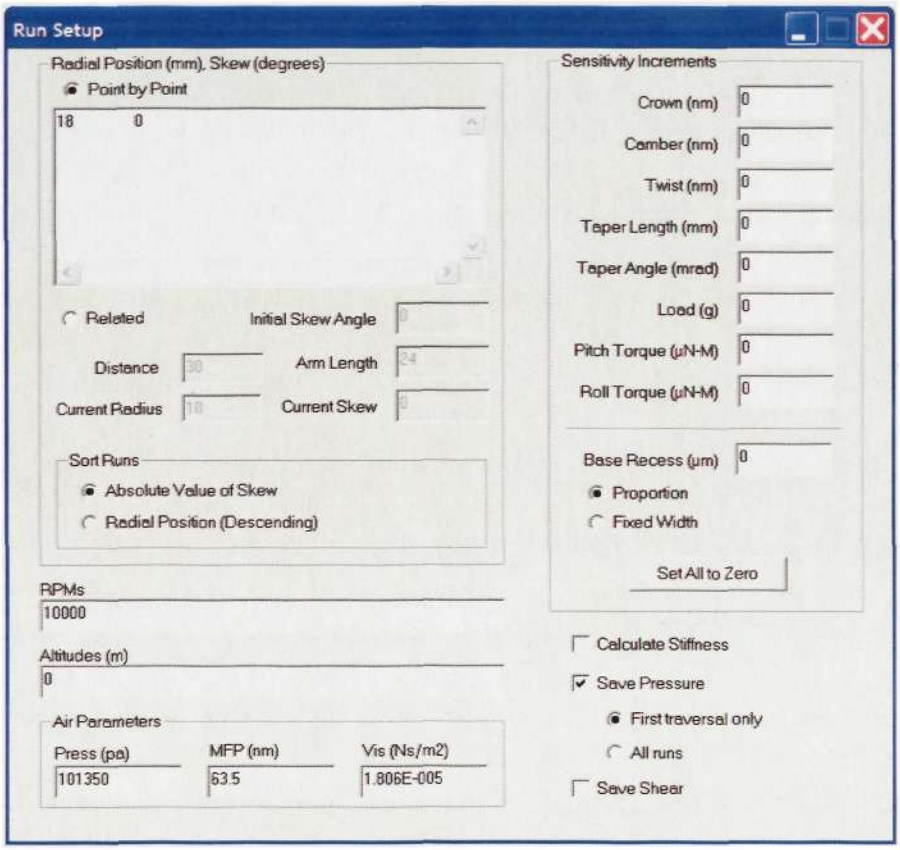

Radial Position (mm), Skew (degrees)
● Point by Point
18 0
○ Related
Initial Skew Angle 0
Distance 30
Arm Length 24
Current Radius 18
Current Skew 0

Sort Runs
● Absolute Value of Skew
○ Radial Position (Descending)

RPMs
10000

Altitudes (m)
0

Air Parameters

Press (pa)	MFP (nm)	Vis (Ns/m2)
101350	63.5	1.806E-005

Sensitivity Increments
Crown (nm) 0
Camber (nm) 0
Twist (nm) 0
Taper Length (mm) 0
Taper Angle (mrad) 0
Load (g) 0
Pitch Torque (µN-M) 0
Roll Torque (µN-M) 0

Base Recess (µm) 0
● Proportion
○ Fixed Width

☐ Calculate Stiffness
☑ Save Pressure
● First traversal only
○ All runs
☐ Save Shear

Fig. 3-8 CML Run setup

3.3.1 Verification of FE Package through Simplified Model with only Air Bearing

Figure 3-9 shows a cantilever together with a patch of PZT flying above air bearing. Under air pressure, the cantilever would deform and the there would be an output of PZT through conversed piezoelectric effect. FE package has been developed to simulate this system. In this system, $\theta_1,\theta_2,\cdots;\theta_k$ are calculated separately for considering the deformation of the cantilever. Here, $\theta_1,\theta_2,\cdots;\theta_k$ is the angle between the horizontal and the tangent of respective point on the cantilever. As there is no existing research on the coupling field system's calculation and result into be difficult to validate our FE package's correctness if we consider all three fields in the system simultaneously. To verify the correctness of the package, several simplified models are used and studied. In this section, the simplified model includes only the air bearing. Features of the first simplified model are, 1) only the air bearing is taken into account, 2) the cantilever is regarded as rigid body, that means there would be no deformation of it under air bearing pressure and 3) no input electrical voltage to the PZT, 4) the cantilever is smooth, without the step on its free end. To simulate such a simplified model, several parameters of FE package are required to be fixed, 1) let the input of PZT voltage be zero, that is to let E=i=w=0 in Figure 3-9, and 2) in every calculation, the angle of each cantilever element θ will keep same during the whole process of computation, that is to let $\theta_1=\theta_2=\cdots=\theta_k=\cdots$ in Figure 3-9. So the whole system will be simplified to be shown in Figure 3-10. Consequently, what we need to solve is air bearing FK model. Figure 3-9 shows sketch of the system if all the three fields (fluid, electrical and mechanical) are included in the consideration. The air pressure distribution on the cantilever calculated from our own developed FE package and CML air bearing design program is shown in Figure 3-12. In our analysis, version 6 of CML is used. The length of cantilever is 1.25 mm. We chose the industry standard slider form $(1.25mm \times 1mm \times 0.26mm)$ for the comparison.

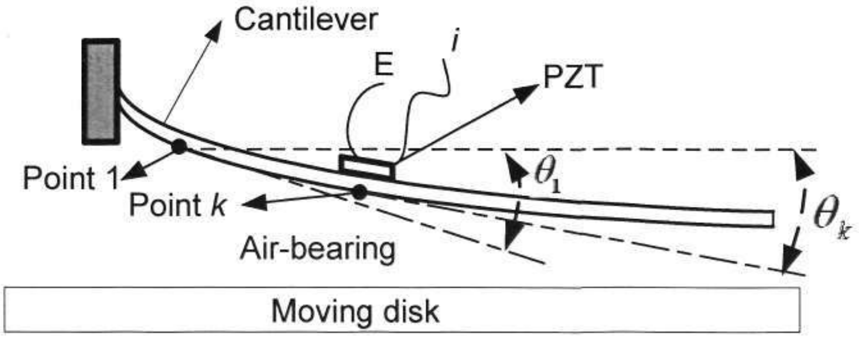

Fig. 3-9 Sketch of system (air bearing, cantilever and PZT)

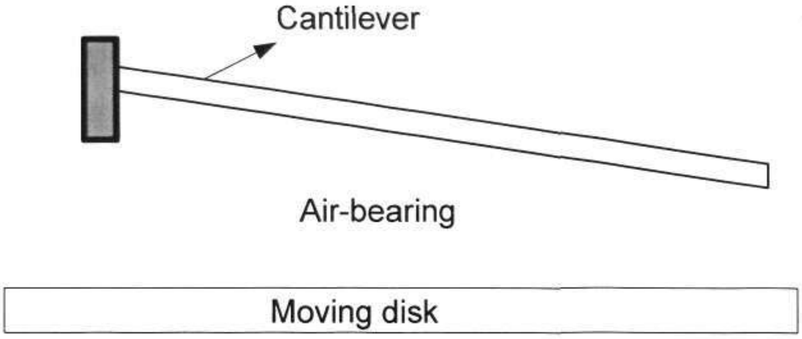

Fig. 3-10 Sketch of system (only air bearing is considered,

i.e. $\theta_1 = \theta_2 = \cdots = \theta_k = \cdots$ and E=i=0)

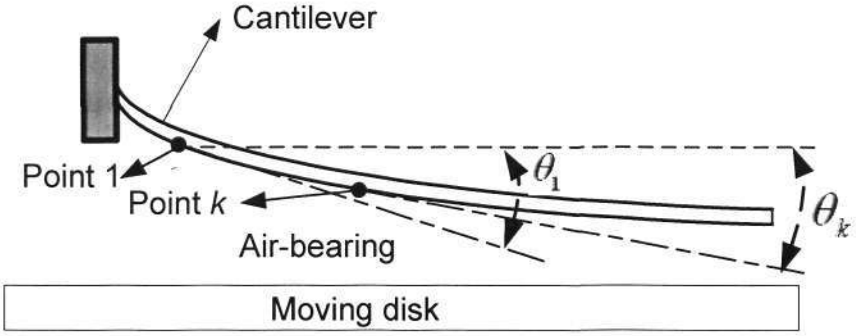

Fig. 3-11 Sketch of system (air bearing and cantilever)

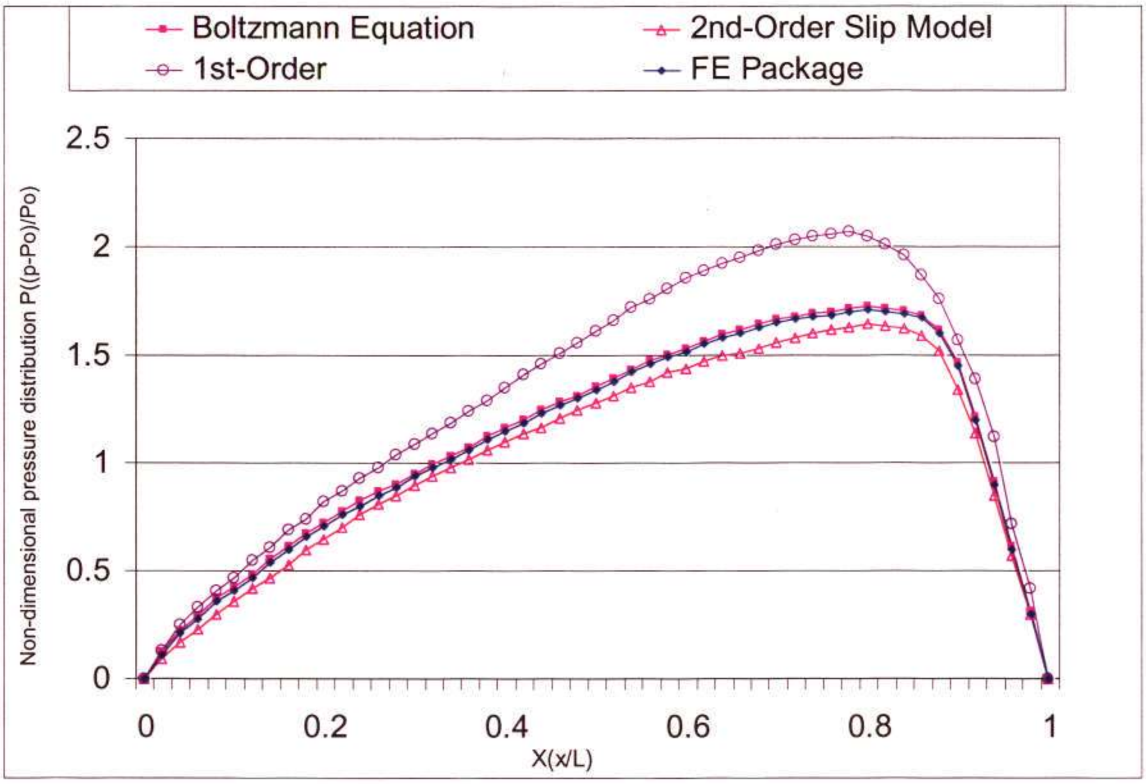

Fig. 3-12 Comparison of pressure distribution for Kn=1.250

From Figure 3-12, the results calculated from FE package are very close to that from Boltzmann equation. This means that the FK model is accurate to model the air bearing with large Knudsen number, as well as that the FE package is correct to carry out the calculation. It can also be obviously seen that the 1st-order slip model overestimates the pressure distribution along the cantilever while the 2nd-order slip model underestimates it. Even the calculated results shows a little difference between our FE package and other existing methods, it is obviously seen that 1) all results are very close each other, 2) results from FE package is between that from 1st slip model and 2nd-order slip model. All these show that this FE package can be use to simulate the simplified model correctly shown in Figure 3-10.

In this simplified model, the comparison of pressure distribution along length of slider was used to validate our developed FE program. Except that, the overall vertical air bearing stiffness is also obtained and compared with existing results. In slider design, the local air bearing stiffness is defined for an individual position on the air bearing surface. And the overall vertical stiffness is defined for the slider as a whole in the vertical direction. Figure 3-13 shows a sketch of slider flying above rotating disk, in which local stiffness for individual position and overall vertical stiffness for the whole slider are defined. In our FE package, assume that the overall force on the cantilever is F_1 when slider is flying at flying height FH_1. When the flying height becomes FH_2, the overall force on the cantilever becomes F_2. So we could retrieve the overall vertical stiffness of the air bearing by equation (3-102).

$$k = \left| \frac{F_2 - F_1}{FH_2 - FH_1} \right| \tag{3-102}$$

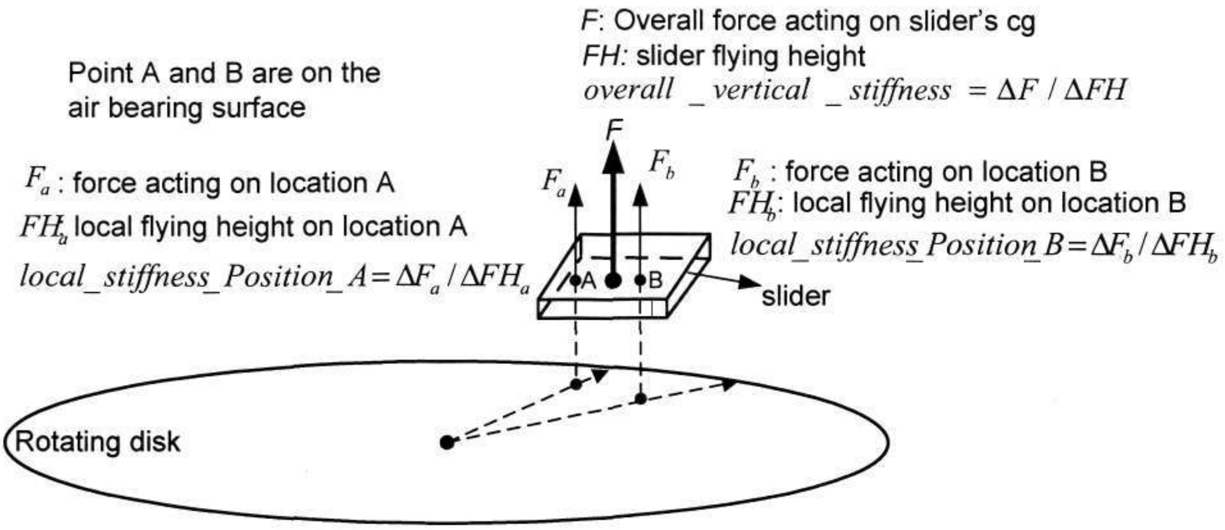

Fig. 3-13 Sketch of slider flying above rotating disk (slider enlarged for clearly seen, cg is abbreviation of center of gravity)

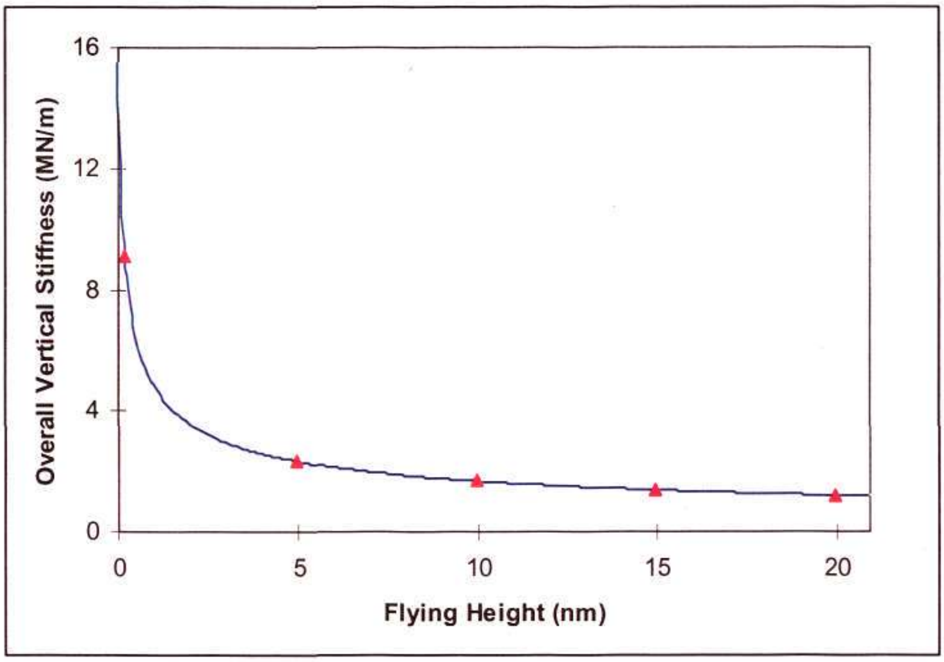

Fig. 3-14 Overall vertical stiffness of air bearing (triangle: from FE package; line: Brian's)

Figure 3-14 shows the overall vertical stiffness comparison results between our FE package and Brain's. It could be obviously seen that a very close matching between these two results. On one side, this good matching shows the correctness of our FE package, on the other side, this means that our FE package could be used to predict or analysis the aerodynamic properties of the air bearing effectively and accurately.

3.3.2 Verification of FE Package through Simplified Model with Cantilever and Air Bearing

In the above section, the comparison results show that the developed FE program has the capability of simulating the simplified model with only air bearing very well. On one hand, the pressure distribution obtained from FE program is very close to that obtained from the CML simulation package. On the other hand, the overall vertical air bearing stiffness matches very well with the previous research result. In this section, the finite element package will be validated by considering one more complicated model, in which the air bearing and cantilever will be taken into account. In this model, 1) angle of each element, θ, will not be kept to be the same, and 2) there is no input voltage into PZT, that means $E=i=0$. The cantilever will deform due to the interaction between cantilever and air bearing. As there is not a completely existing program to solve such a model, we compare the pressure distribution obtained from FE package with that from the CML simulation package. Figure 3-15 shows the comparison results.

From Figure 3-15, it is obviously seen that the calculated results from FE package for this simplified model are more close to the 2nd-order slip model than others. Even that, it is very clear that the difference between different models is very small. All these show that the FE package can be also used to simulate such a simplified model shown in Figure 3-11. Comparing Figure 3-12 and 3-15, it could be obviously seen that the pressure is lower of the air bearing after we consider the deformation of the cantilever. This fact is coincided with the physical phenomenon that the pressure decreases when the flying height increases. From this side, the correctness of the FE package is also proved.

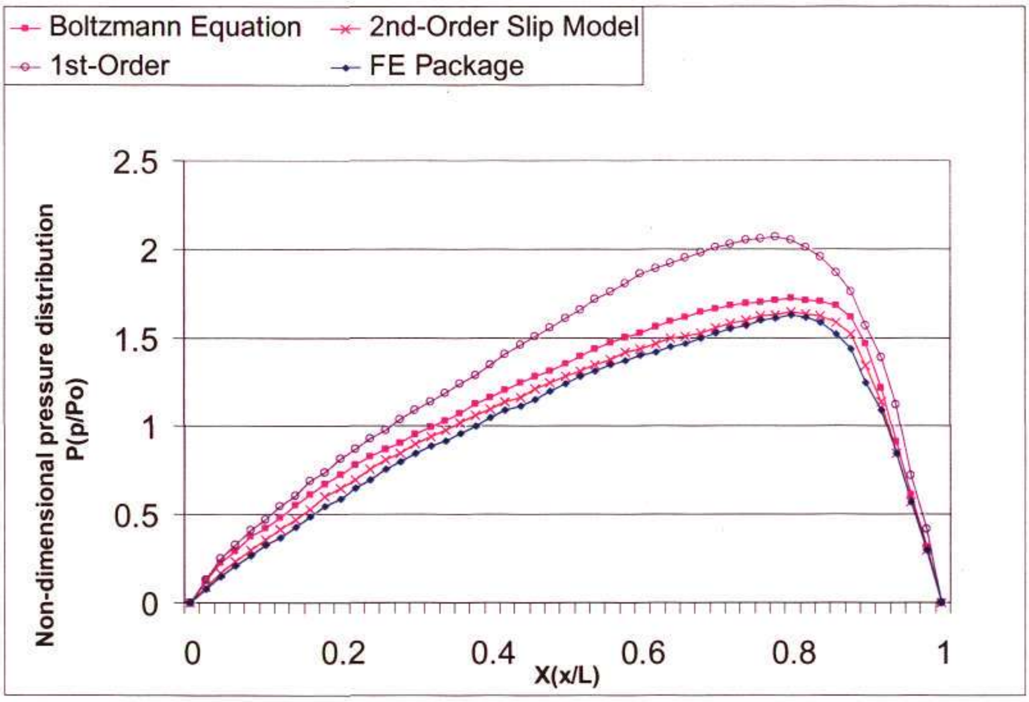

Fig. 3-15 Comparison of pressure distribution for Kn=1.250

3.3.3 Pressure Distribution with All Three Fields

In the above sections, the correctness of our FE program has been verified by two simplified models through comparing the results obtained from FE package with that from existing research and design program CML. As the air bearing surface are a 2-dimensional area, and our FE program could not realize a full capability of industrial slider design. But it is good enough for us to carry out new slider design, in which a patch of PZT, one cantilever and air bearing are integrated together. In the following section, the FE package will be applied to simulate the whole system with three fields, air bearing, cantilever and PZT. Figure 3-16 shows the non-dimensional pressure distribution of different conditions. From this figure, obviously it can be seen that the pressure is a little lower for the whole system compared with the system discussed in previous section. The decrease of pressure is the result of the vibrating cantilever and deformation of itself. Even more, the difference is not more than 10% among each system.

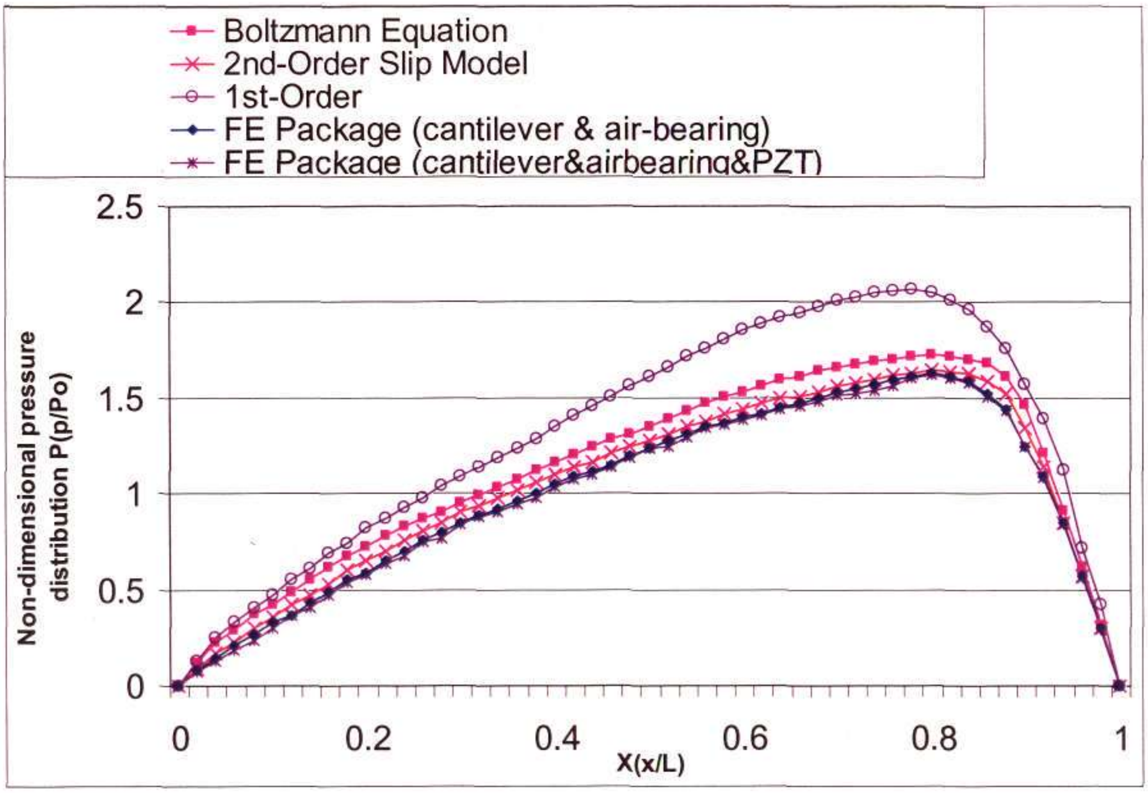

Fig. 3-16 Comparison of pressure distribution for Kn=1.250

From the above comparisons in Section 3.1-3.3, it is obviously seen that the FE package developed by ourselves can be used to simulate the coupling field system effectively and accurately. In the next chapter, it will be used to be a tool for further study on the in-situ flying height measurement of the slider.

3.4 Conclusions

In the above study, derivation of the finite element matrix for air bearing, cantilever and PZT film has been successfully carried out. Based on these matrices, the finite element model has been built up for the sensor flying above the disk surface. A FE program written in MATLAB has been developed and verified by several simplified model. From compared results between FE package and existing researchers', it could be concluded:

1) The FE package could be used to calculate the air bearing pressure distribution in a very close result with Boltzmanns equation.
2) The pressure distribution calculated from FE package is very close to that from Boltzmann's equation when we only consider air bearing in the system. And it would be close to that from 2nd order Reynold's equation when we consider two fields (air bearing and cantilever) or three fields (air bearing, cantilever and PZT) in the system.
3) The FE package could be also used to predict or analysis the dynamic properties of air bearing. For example, the stiffness of air bearing has been achieved by our FE package, which shows a matching result calculated from other research.
4) In our study, the air bearing has been modeled by using a one-dimensional Reynolds equation, and the pressure variation along the slider width direction has not been taken into account, which is a simplification of the real system. In real system, the air passes through the slider in its width direction unevenly due to the skew angle effect. This results into the pressure variation in the transverse direction. The current simplification assumes that air flow passes evenly through the slider in its width direction. This would make the slider's FH a little bigger than the actual FH due to more air passing through the slider. This bigger FH results into lower pressure on the slider. In this sense, air pressure on ABS is a little under-estimated. This phenomenon is obviously shown in the Figure 3-12, 3-15 and 3-16 etc.

Chapter 4

Virtual Testing of In-Situ Flying Height Measurement Capability of New Slider Design

In the previous chapters, the proposed slider design with a sensor (PZT cantilever) for in-situ flying height measurement capability has been introduced and the finite element model for the sensor flying above disk surface has been developed. In this chapter, virtual testing of the in-situ flying height measurement capability of new slider design will be carried out by ANSYS and our developed FE program respectively. Comparisons between both of the results obtained from these two methods are also shown.

4.1 Virtual Testing of In-Situ FH Measurement Capability using ANSYS

Figure 4-1 shows the simplified structure of the proposed slider design. In this design, the slider body will mainly be used to determine the flying height of the slider. The flying height is the distance between the step on cantilever and the rotating disk.

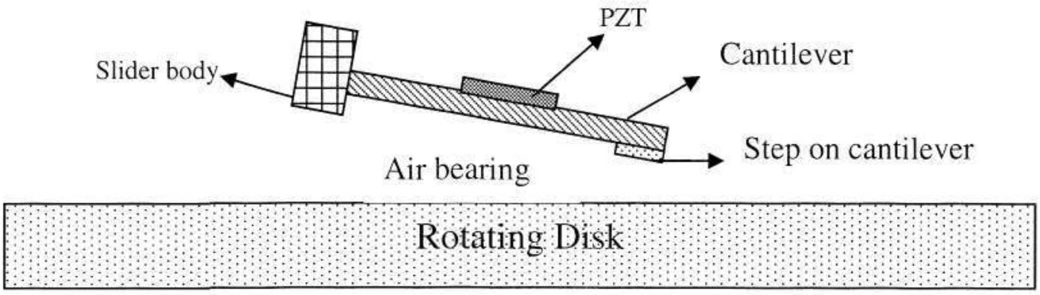

Fig. 4-1 Simplified structure of proposed slider

The sensor which is consisting of a cantilever and a patch of PZT film is used to sense the flying height. When a certain voltage with a desired frequency is input to the PZT film during HDD's working state, there will be three fields involved, electrical (PZT), mechanical (cantilever) and fluid (air bearing). ANSYS was chosen to be the tool for building a finite element model for this coupling field system. As there is no existing element in ANSYS to simulate the coupling fields between PZT, cantilever and air bearing, so we solve these three fields' coupling field problem by two steps, 1) solve coupling field problem between air bearing and cantilever, then 2) solve coupling field problem between cantilever and PZT. In the first step, the air bearing is modeled as a set of springs, which are assumed to be linear in our study. The spring constants of all these springs are obtained by solving the coupling field problem between the air bearing and the cantilever. In section 4.1.1, we will describe the finite element model that will be used to obtain the spring constants. After we get the spring constants for all springs, the air bearing will be substituted by the whole set of springs. Then the whole system will consist of the PZT, cantilever and the springs. With the help of ANSYS, we can do the Harmonic Analysis for this simulated mechanical system. The finite element model for PZT, cantilever and springs will be introduced in Section 4.1.2.

4.1.1 Finite Element Model of Cantilever and Air bearing

In this section, we will build a finite element model for the cantilever and air bearing. This model will be used for obtaining the spring constants of the springs. After we get the spring constants for all the springs, the air bearing will be represented by the set of springs. The problem background, definition, and finite element modeling of the cantilever and air bearing by ANSYS will be introduced in the following parts.

4.1.1.1 Problem Background

After air bearing is modeled by a set of springs, O_1, O_2, … , O_n, the sketch of the coupled system among air bearing, PZT and cantilever can be shown as Figure 4-2. Here n is the quantity of the cantilever elements. The spring constants of these springs will be obtained by perturbation method. Here, the flying height *h* is the distance from the tip of the cantilever to the disk. Figure 4-3 shows a sketch of spring with one end fixed and the other end free.

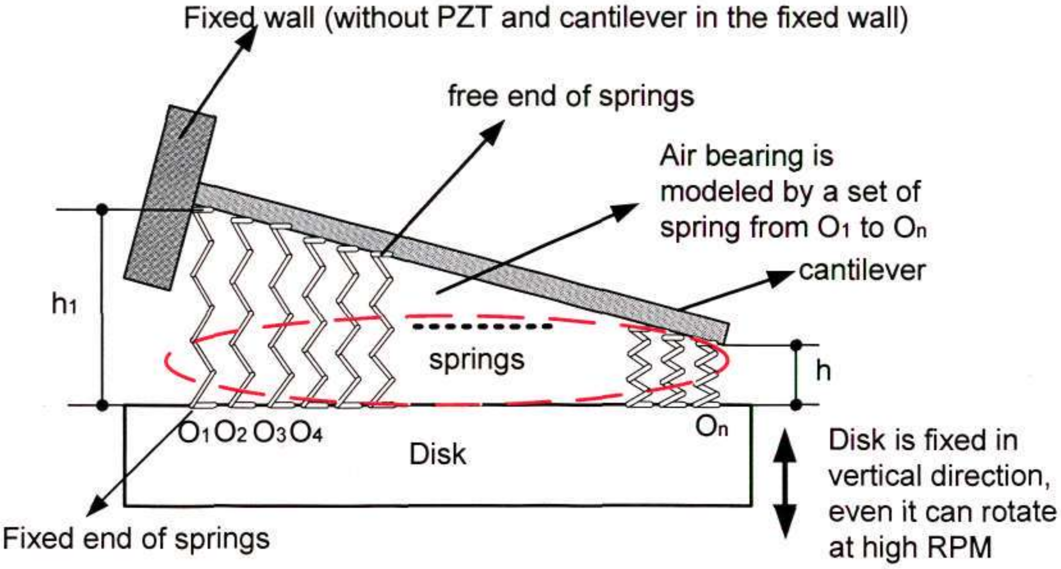

Fig. 4-2 Sketch of PZT, cantilever and springs

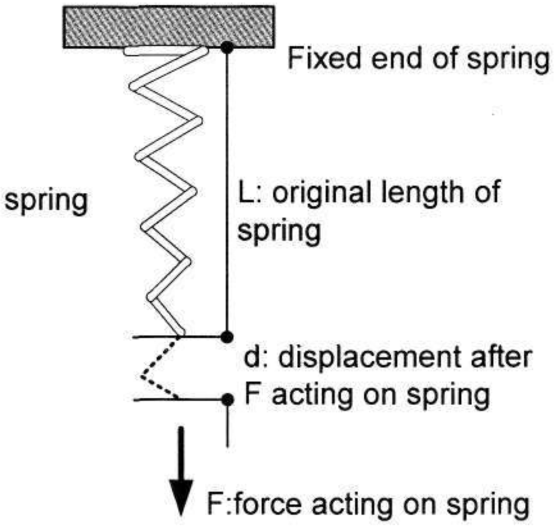

Fig. 4-3 Sketch of spring (one end fixed and the other end free)

In this model, the key point is to get all the spring constants, $K_1, K_2, ..., K_n$ for the set of springs, $O_1, O_2, \ldots, O_n$. From the basic relationship of the spring displacement and force, we can easily obtain the spring constant as shown in Equation 4-1, where d is the displacement after the force F acts on the spring, and K is the spring constant. Here, we assume d is small enough to keep the spring function in its linear scale. When we use the perturbation method to obtain the spring constant, the spring constant is assumed to be kept the same within a very small FH variation.

$$K = F / d, \tag{4-1}$$

4.1.1.2 Problem Definition

In the real working state of hard disk drive, air bearing is formed between disk surface and slider, the disk is considered as fixed in the vertical direction with regards to the slider, since the disk is much thicker and heavier than the slider. If we use a set of springs to represent the air bearing, the fixed end of springs is considered on the disk surface, which is also shown in Figure 4-2. Here, we will use the spring *O₁* as an example to show the way for us to obtain the spring constant. If the slider is flying at a prescribed height, the local flying height on the position of *O₁* is h_1. At this moment, the force acting on O₁ is F_1. If a very small perturbation happens on the slider, or if the local flying height on the position of *O₁* changes a very small value Δh_1, this small change of local flying height will result into a very small change of the force acting on *O₁*. Suppose the change of force is ΔF_1. Based on equation (4-1), we can calculate the spring constant of *K₁* as

$$K_1 = \Delta F_1 / \Delta h_1 \tag{4-2}$$

4.1.1.3 Finite Element Model by ANSYS and Results

Based on the description above, a finite element model is built to realize the analysis using ANSYS. BEAM54 is selected as the cantilever element and FLUID141 is selected as the air bearing element. The procedure to obtain these spring constants is described here. Firstly, the air bearing force $F_1, F_2, F_3 \cdots F_n$ along the cantilever elements are obtained under a prescribed flying height *h,* shown as in Figure 4-4. Some of the mechanical parts are omitted since most of them have been introduced in Figure 4-2. Then the forces $F_1, F_2, F_3 \cdots F_n$ are loaded on the beam elements along the cantilever. At this moment, the cantilever has a small deformation. Under this state, one more very small displacement Δh_1 is added on the cantilever. This Δh_1 could be upward or downward direction. Then a static analysis is carried out on the air bearing. After this analysis, we obtain another group of force $F_1^{'}, F_2^{'}, F_3^{'}, \cdots F_n^{'}$ which is acting on the beam elements. Based on Equation (4-2), we could get the spring constants of O_1 as shown in Equation (4-3). For our analysis, several trials using Δh_1 from 0.05 to 0.5 have been carried out. The spring constants from different trials are close. Here, we choose Δh_1=0.1 nm. Using the same method, the other spring constants for O_1 , O_2 , … , O_n can be obtained.

$$k_1 = (F_1 - F_1^{'}) / \Delta h_1 \tag{4-3}$$

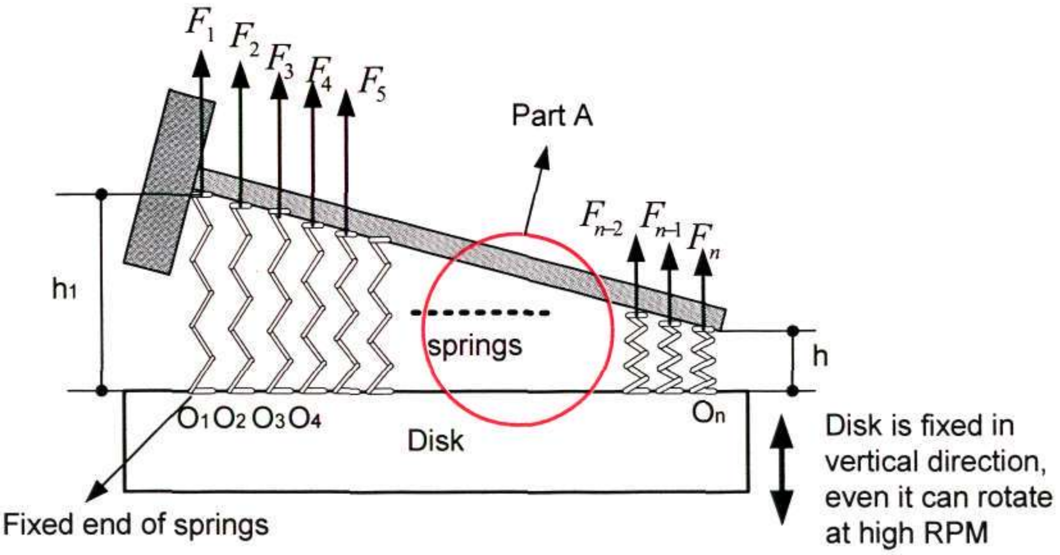

Fig. 4-4 Air bearing force acting on cantilever

To model the air bearing, Fluid141 is chosen. Figure 4-3 shows the sketch of a part of the finite element model built in ANSYS.

We can see from Figure 4-2 that the element of air bearing shares the same node as that of cantilever on their contact surface. In our analysis, we assume, 1) the number of cantilever elements is equal to the number of springs, 2) the n^{th} spring is made from the air between the disk surface and the n^{th} cantilever. The velocity of the moving disk has great influence on this analysis. The FE model of part A in Figure 4-4 is shown in Figure 4-5. The boundary of the FE model is set on the disk surface and the left end of the cantilever. Elements on the boundary are fixed and no any linear and rotational displacements and there is no any moment in any directions.

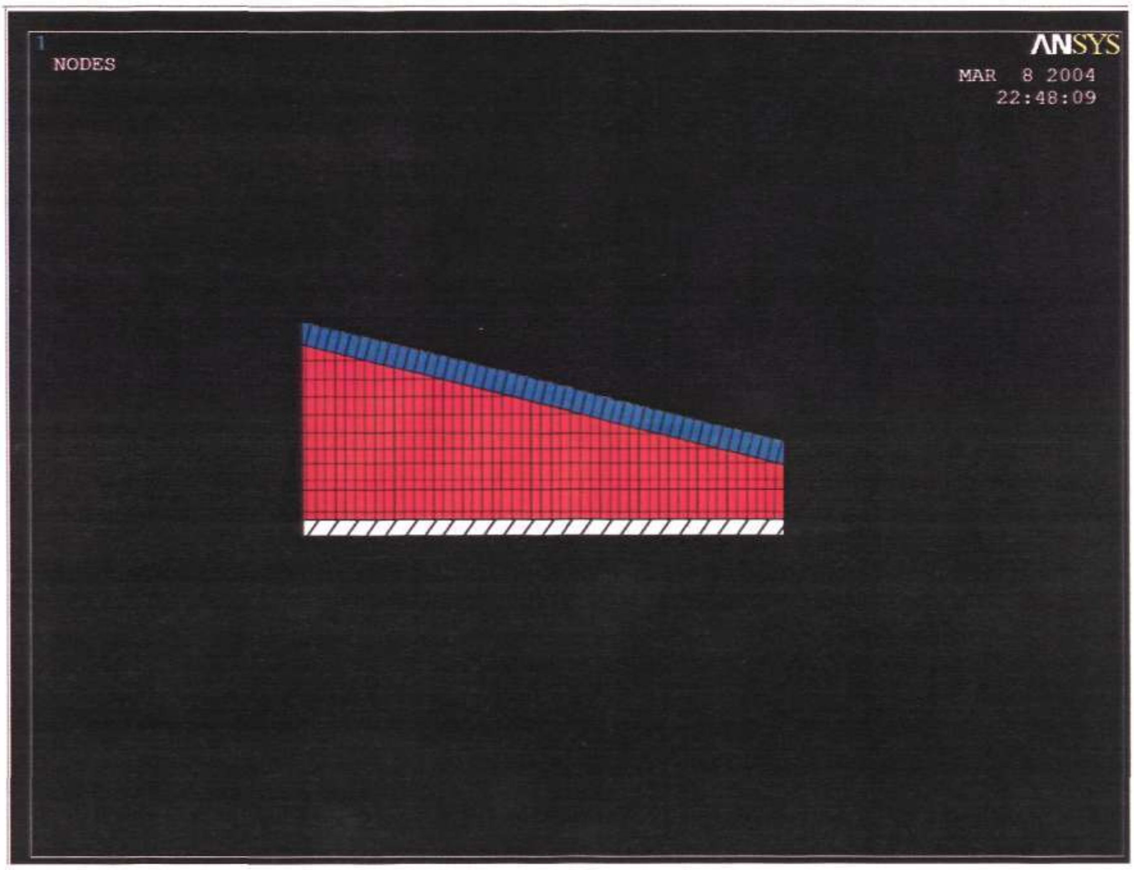

Fig. 4-5 FE model corresponding to the part A of Figure 4-4 (BEAM54 elements are in blue and the FLUID141 elements are in red)

In this case study, the material of cantilever is selected as industrial slider material, which is a mixed of Al_2O_3 and MgO_2. The material properties of the cantilever are shown in Table 4-1. The air properties are shown in Table 4-2. Here, the cantilever is divided into 5000 BEAM54 elements. The quantity of 5000 is a good choice and it is enough for our analysis because the calculated spring constant from the ANSYS FE model is close to the values if more elements are considered in the FE model. The calculated spring constant is shown in Table 4-3 when the disk is rotating at the speed of 15 m/s. It is obviously seen that the spring constants on tip of the cantilever are close each other when quantity of elements are 5000 and above. But the computation time is longer when quantity of elements is bigger. So we choose 5000 as the quantity of cantilever elements in our study.

Table 4-1 Material properties of cantilever

Length	Width	Thickness	Young's Modulus	Density
0.5 mm	0.05 mm	0.015 mm	390 GPa	$2690 Kg/m^3$

Table 4-2 Properties of air (ambient temperature and humidity)

Mean free path	Viscosity	Ambient pressure	Thermal conductivity	Density
63.5 nm	1.806e-5	101325 Pa	0.0257 W/(mK)	$1.205 Kg/m^3$

Table 4-3 Spring constant under different quantity of beam elements

(Disk velocity= 15m/s)

Quantity of Beam Elements	500	1000	1500	2000	3000	4000	5000	5500	6000
Spring constant on the tip of cantilever (N/m)	11323	11989	12497	12858	13114	13211	13231	13239	13241

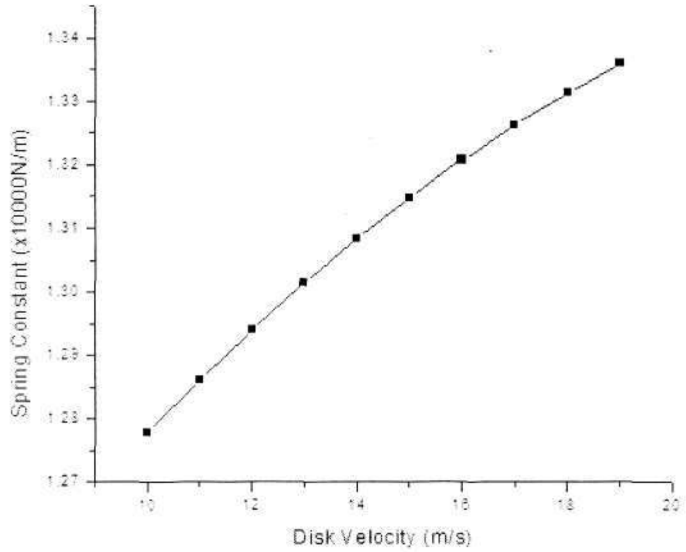

Fig. 4-6 Spring constant of O_{5000}

Figure 4-7shows the obtained spring constant of O_1 under different velocity of moving disk.

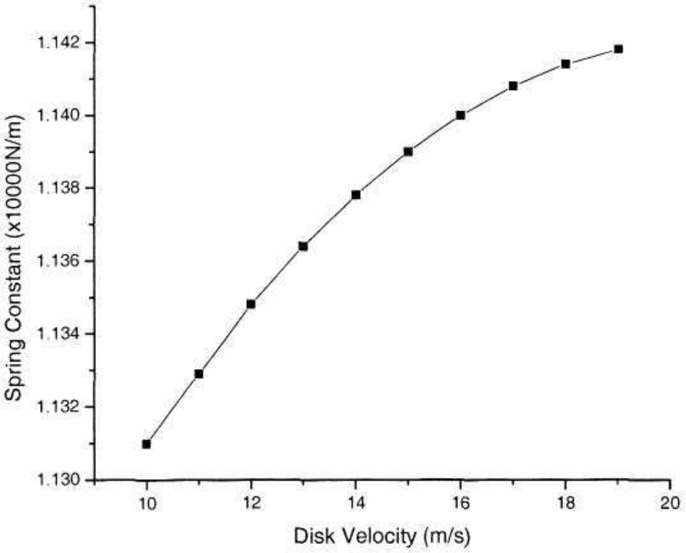

Fig. 4-7 Spring constant of O_1

Figure 4-8 shows the obtained spring constant of O_{2500} under different velocity of moving disk.

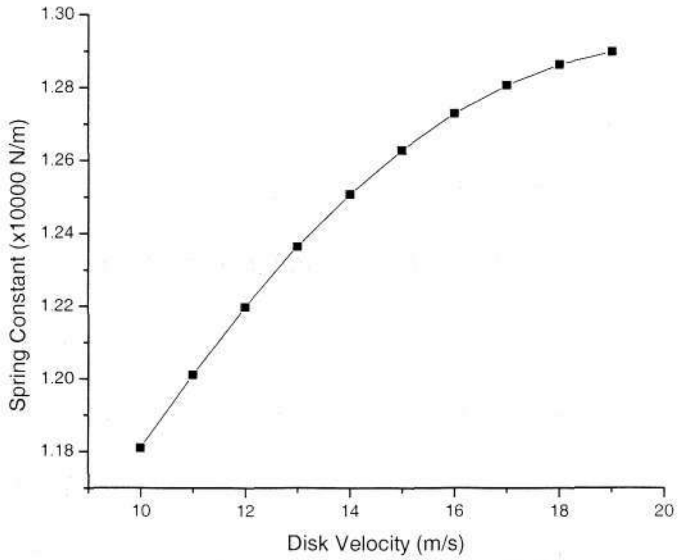

Fig. 4-8 Spring constant of O_{2500}

From Figure 4-6 to Figure 4-8, it is obviously seen that the spring constant becomes bigger when the velocity increases. Here only the spring constants of three springs have been shown, but the other springs behave similarly like the above three springs. After we got all these spring constants under different velocity, the air bearing can be substituted by these springs. The following part will be focused on the finite element model about the PZT, cantilever and the air bearing, in which the air bearing was substituted by the springs.

4.1.2 Finite Element Model for PZT, Cantilever and Air Bearing

In above section, the way to get the spring constants for the springs has been shown. In a special case, some simulation results of the spring constants have also been achieved. Using these spring constants, the air bearing can be represented as a set of springs. This air bearing model makes us be capable of carrying out the further research easily, due to the powerful capability of ANSYS in solving the coupling field problem between electrical (PZT) and structure (cantilever and spring). The finite element model was built, in which the cantilever was divided into 5000 elements. For PZT, the SOLID45 was selected. SOLID45 is a built-in element in ANSYS, which is useful in solving the coupling field problem between structure and electrical. In ANSYS, one method to solve the coupling field problem is the sequential method. The detailed information about this method can be found in the ANSYS documentation. Here Figure 4-9 only shows the data flow for this sequential method. It is extracted from the Help files built in ANSYS. AATT, VATT, PHYSICS, READ and LDREAD are predefined commands built in ANSYS. For more detailed you could check the latest version of ANSYS help. AATT and VATT are used to associate element attributes with the selected, unmeshed area and volumes respectively.

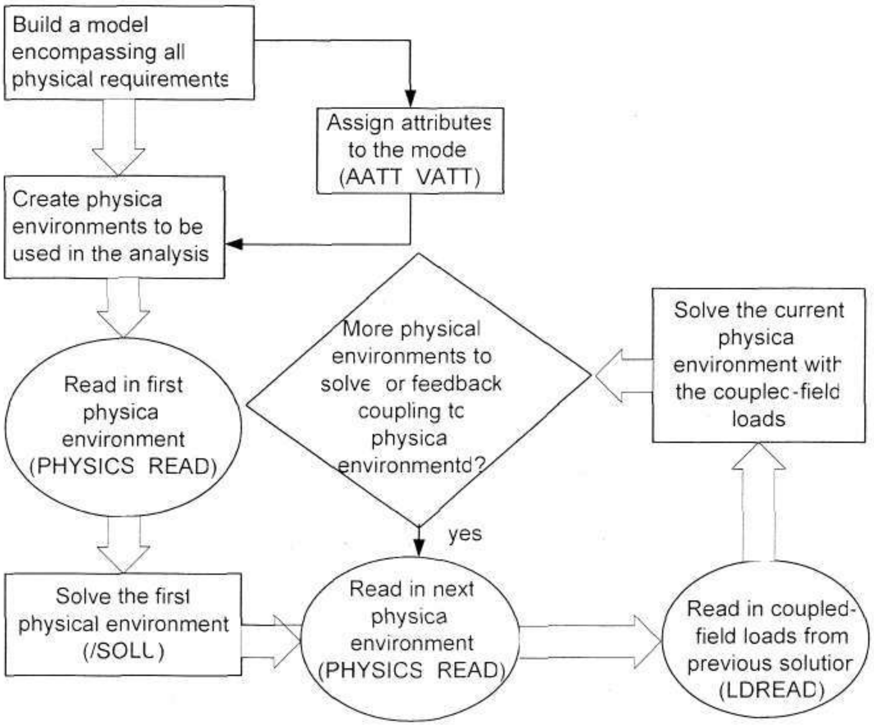

Fig. 4-9 Data flow for sequential method of ANSYS

For PZT, SOLID45 was chosen in the following analysis. The density of this PZT is 7800 (kg/m^3). In our computation, the coupling field problem of the structure (cantilever and spring) and electrical (PZT) was solved. To predict the dynamic sustained dynamic behavior of the cantilever, the harmonic analysis was carried out.

In the analysis, the cantilever's parameters are same as that shown in Table 4-1. The PZT is coated on the cantilever. Figure 4-10 shows the position on which the PZT coated on the surface of the cantilever.

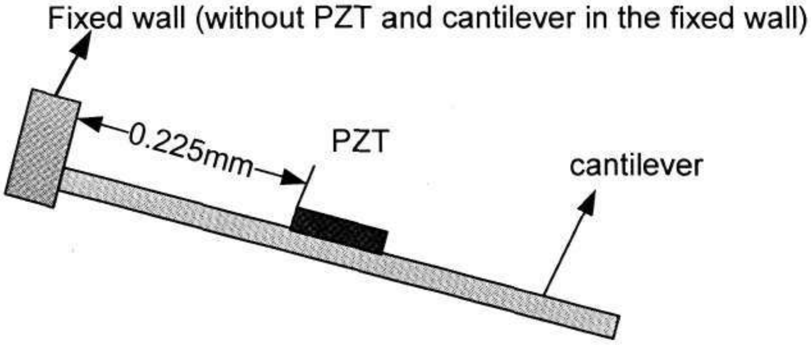

Fig. 4-10 Sketch view of PZT and cantilever

The dimension of PZT is shown in Table 4-4.

Table 4-4 Parameters of PZT

Length	Width	Thickness	Density
0.5 mm	0.05 mm	0.002 mm	$7800Kg/m^3$

With the help of ANSYS, the harmonic analysis was carried out. In this analysis, an alternating voltage was input into the PZT. The frequency of the alternating voltage changes from 91300 Hz to 91500 Hz. This range of frequency is selected because the natural frequency of the above mentioned cantilever is near 91460 Hz. The natural frequency of this cantilever is calculated with ANSYS too. Figure 4-11 shows the electrical impedance, or the output of the PZT, changes with the frequency under different flying heights. In this case of simulation, the velocity of the moving disk is 10 m/s. Figure 4-12 to Figure 4-16 shows different magnified part for Figure 4-11.

From Figure 4-11, we can see that the electrical impedance of PZT is quite large when in a certain range of frequency. It can reach almost 138 ohm near 91460 Hz. Figure 4-16 shows the electrical impedance changes with flying height when frequency is equal to 91306 Hz. The slope shown in Figure 4-19 is 1.048 ohm/nm.

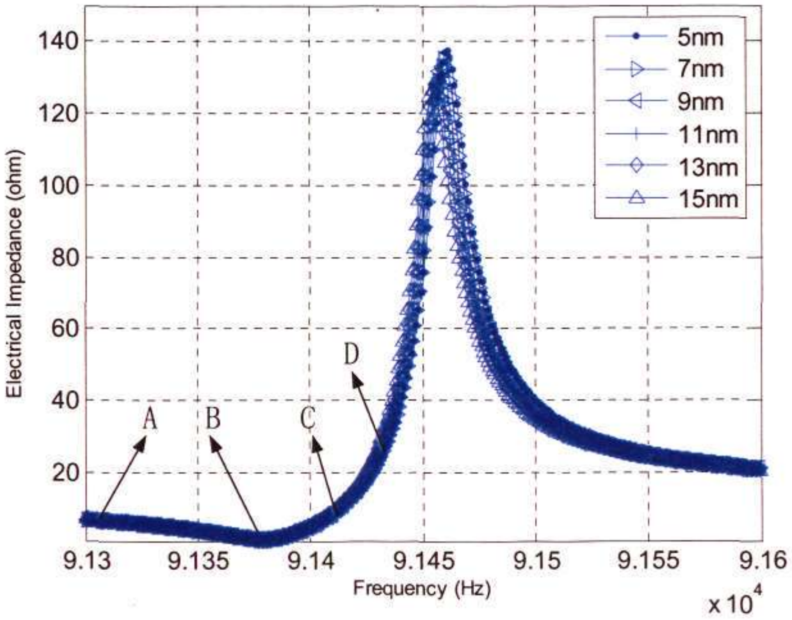

Fig. 4-11 Ze-FH under different frequency

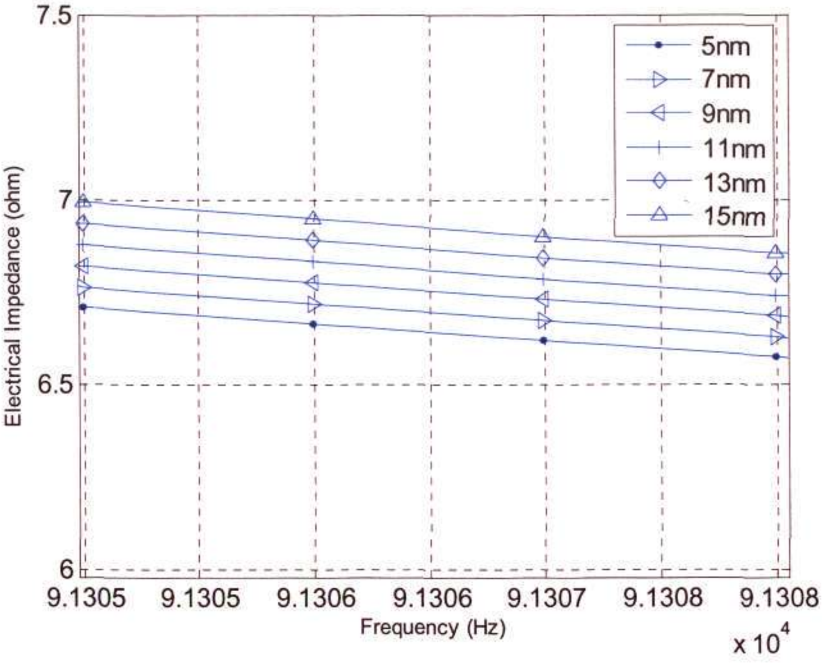

Fig. 4-12 Part A

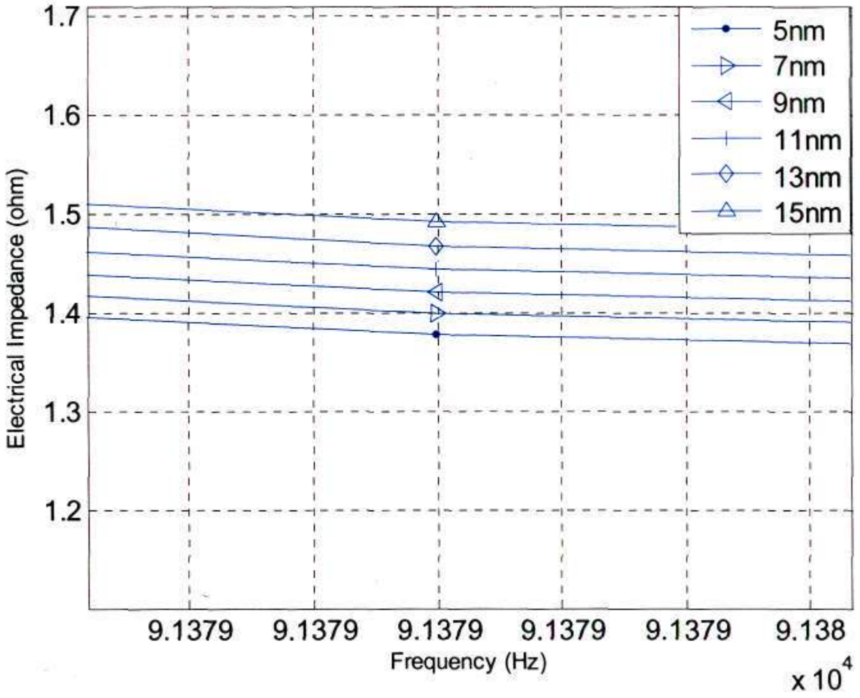

Fig. 4-13 Part B

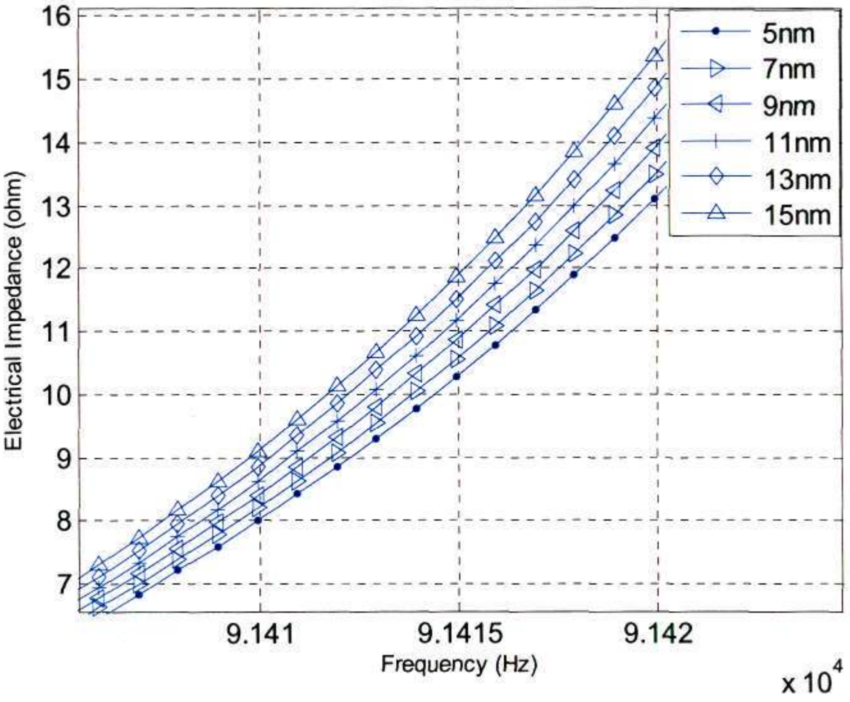

Fig. 4-14 Part C

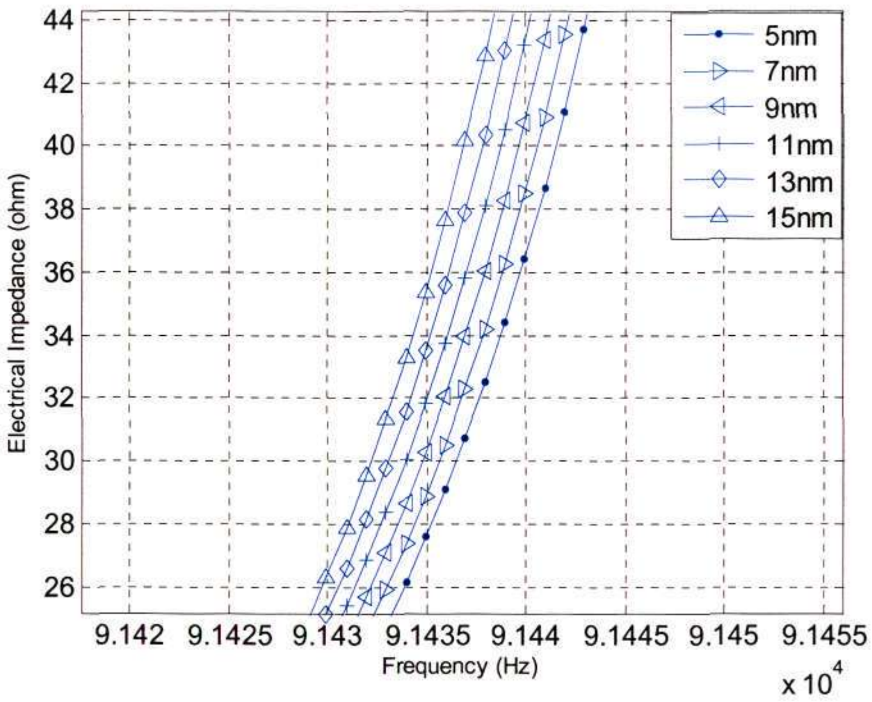

Fig. 4-15 Part D

Figure 4-16, 4-17, 4-18 and 4-19 show electrical impedance changes with flying height when the frequency of the input voltage is equal to 91306 Hz, 91379 Hz and 91415 Hz and 91438 Hz respectively. The corresponding slope of each line is also shown in the figures.

From these figures, we can see that there is a good linearity between the electrical impedance and flying height when the frequency is pre-calibrated to be not close to the natural frequency of the cantilever. The sensitivity is 0.017, 0.0113, 0.173 and 1.048 *ohm/nm* under different driven frequency of voltages. As the exciting frequency reaches near the fundamental natural frequency, the sensitivity becomes larger. This fact is shown in Figure 4-17. But for frequency far from the fundamental natural frequency of cantilever, the sensitivity is smaller. Even though, all these figures have indicated a good linearity between electrical impedance and flying height. The feasibility of using such an active cantilever to realize in-situ flying height measurement has been approved. So the electrical impedance, as a signal, is very useful for in-situ flying height measurement.

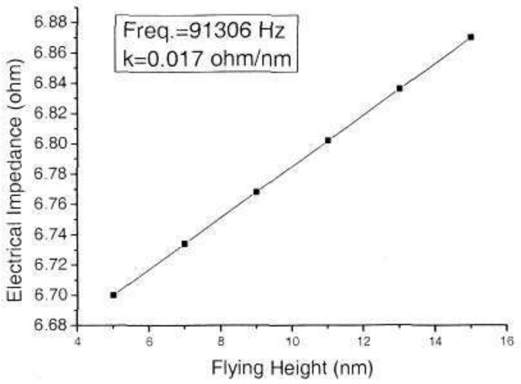

Fig. 4-16 Ze-FH (Freq. =91306Hz)

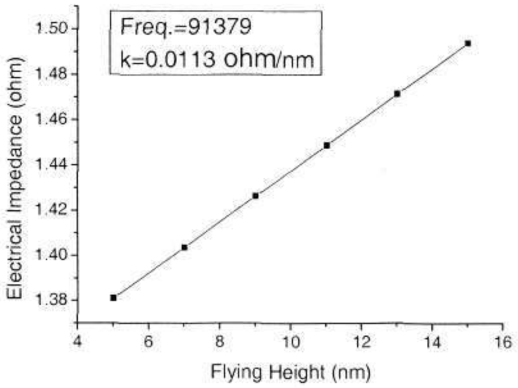

Fig. 4-17 Ze-FH (Freq. =91379Hz)

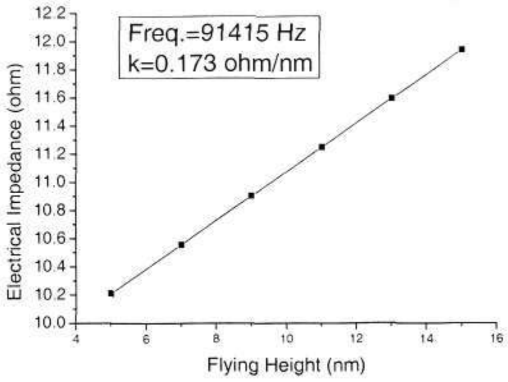

Fig. 4-18 Ze-FH (Freq. =91415Hz)

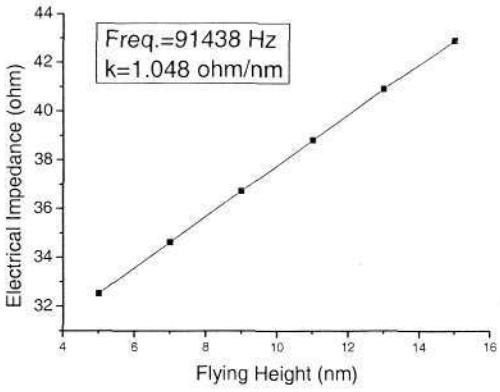

Fig. 4-19 Ze-FH (Freq. =91438Hz)

From the above results, we know that there is a good linearity between the electrical impedance and flying height. And the sensitivity can reach 1.048 ohm/nm when the cantilever is 0.5 mm length. In Table 4-5, the sensitivities of the cantilever with different length are shown near its first fundamental frequency. The parameters of the cantilever except for the length are all the same as which were used in the above. The same PZT is used in these different calculations.

Table 4-5 Sensitivity of cantilever with different length

Length (mm)	0.6	0.55	0.50	0.45	0.40
Sensitivity (ohm/nm)	1.08 (freq.=93731 Hz)	1.06 (freq.=92656 Hz)	1.048 (freq.=91438 Hz)	0.98 (freq.=90689 Hz)	0.93 (freq.=89354 Hz)

In Table 4-5, we can see that the sensitivity of the cantilever increases when the length of the cantilever increases. For the currently used slider in hard disk drives, the total length of it is usually 1.25 mm, so we cannot make a cantilever with too large length. So we need negotiate between sensitivity and length when carry out the slider design with this concept.

4.2 Virtual Testing of In-Situ FH Measurement Capability using FE Program

In the above section, finite element modeling of cantilever, PZT and air bearing has been carried out using ANSYS. The simulation results show there is a good linear relationship between output electrical impedance and flying height. The sensitivity could reach 1.408ohm per nanometer. Theoretically, the system consisting of cantilever, PZT and air bearing includes three coupling fields. These fields are interacted each other. Any variation for one of the fields will cause the variation of other fields. ANSYS solves this coupling field problem by two step described above. Fore more accurate study of the system, as well as the study of in-situ flying height measurement capability of the slider, the three fields should be solved simultaneously. The following part will introduce the solutions to these coupling fields problem by our developed FE program.

The input voltage for PZT is fixed at 0.1 volt and sweeping frequency is from 91350 Hz to 91550 Hz. The sweep frequency is chosen based on the natural frequency of cantilever which is about 91446 Hz. All these parameters are input to FE package. Figure 4-20 shows the relationship between flying height and electrical impedance based on the frequency change. Figure 4-21 shows the zoom-in view of part of Figure 4-20, which makes it more clearly. Figure 4-22 to Figure 4-31 show relationship between electrical impedance and flying height in a certain frequency. Inside these figures, the calculated results are shown as dotted point. Inside the same figure, a curve fitting line (or called as trend line) is used to shown the relationship between electrical impedance and flying height. The equations show the fitting relationship between these two variables in a certain frequency. The R square is an indicator from 0 to 1 that reveals how closely the estimated values for the trend line correspond to the actual data. A trend line is most reliable when its R square value is at or near 1. At the same time, a large R square value means a more linear relationship between the two variables. Table 4-6 (A)-(C) shows summary of all these relationships. From these tables, it is obviously seen that the relationship between electrical impedance and flying height is almost linear in the frequency range from 91350 to 91400 Hz. The sensitivity becomes larger along the frequency axis. It can reach about 0.9465 ohm/nm as the R square is 0.9991. This large R value means that there is a good reliability and linearity between electrical impedance and flying height. As the voltage driving frequency reach 91410Hz and 91415 Hz, which are near the natural frequency of cantilever, the sensitivity can reach higher, but the R square values become smaller. These smaller R values indicate the linear relationship between electrical impedance and flying height is not very good. From this point of view, to keep the sensor in a good linear working situation, one must do a tradeoff between sensitivity and linearity. Further observation shown in Figure 4-20 indicates that there are signs of nonlinearity in the curve for greater flying heights. This nonlinearity is probably the result of a lower pressure on the cantilever beam with bigger flying height. This bigger flying height results into a lower stiffness of the air bearing. Low stiffness causes the cantilever beam larger vibration, which exceeds our assumptions of small motion of the PZT cantilever, and it leads to nonlinearity.

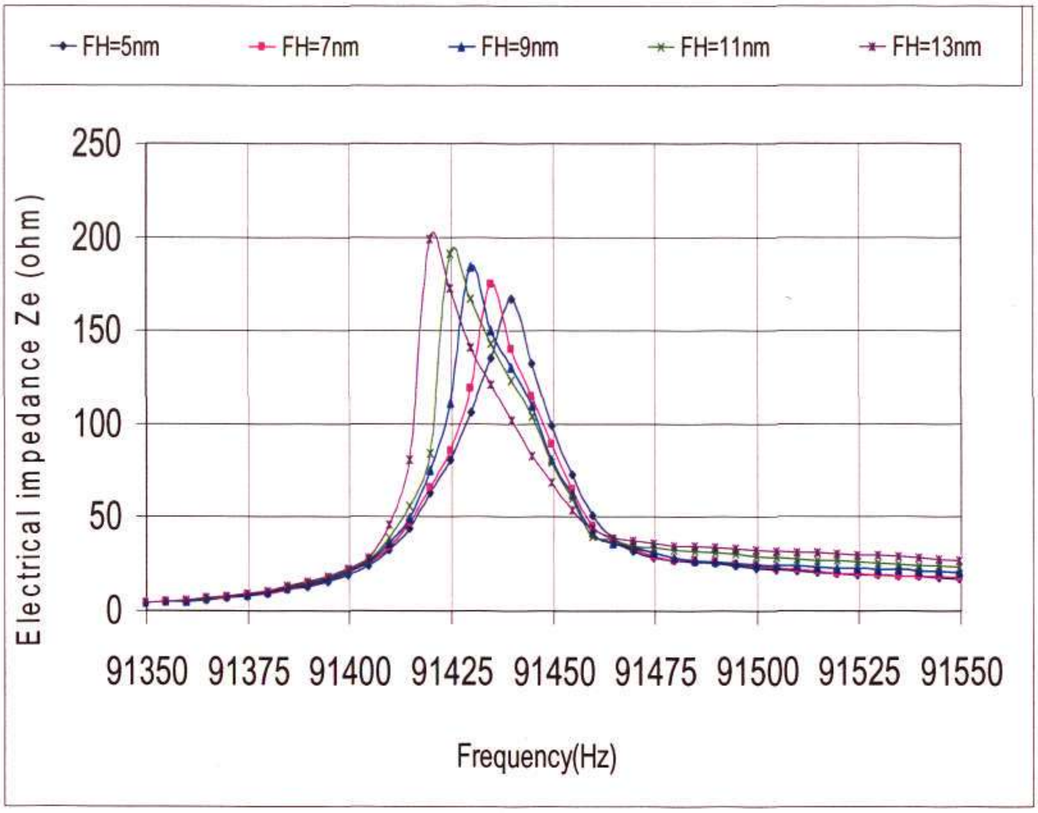

Fig. 4-20 Ze Vs Frequency under different flying height

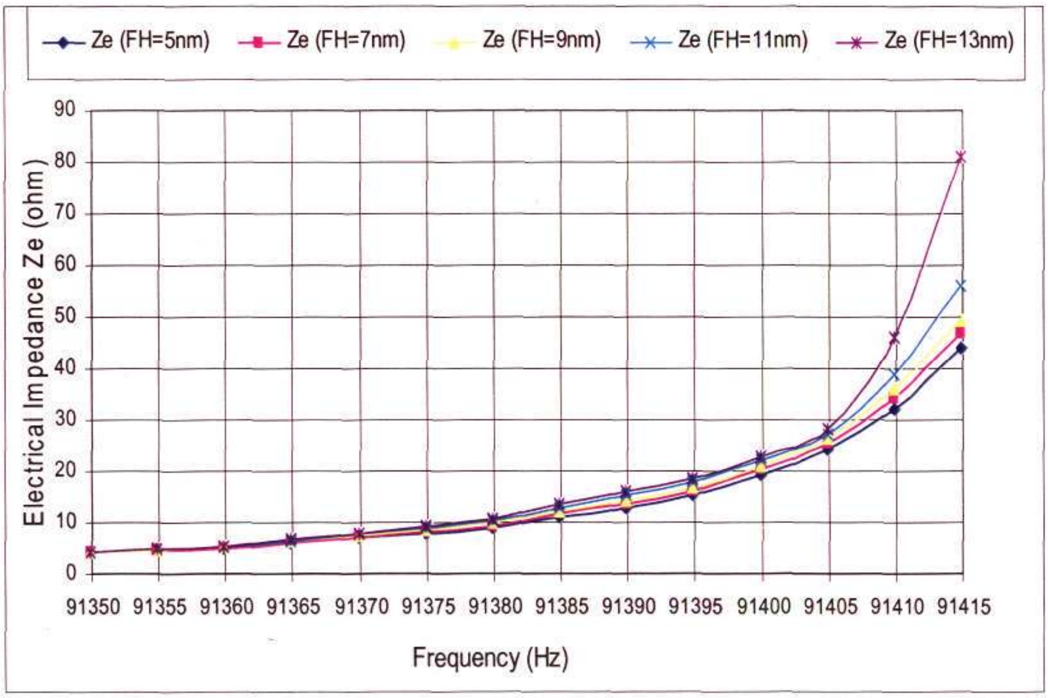

Fig. 4-21 Zoom in view

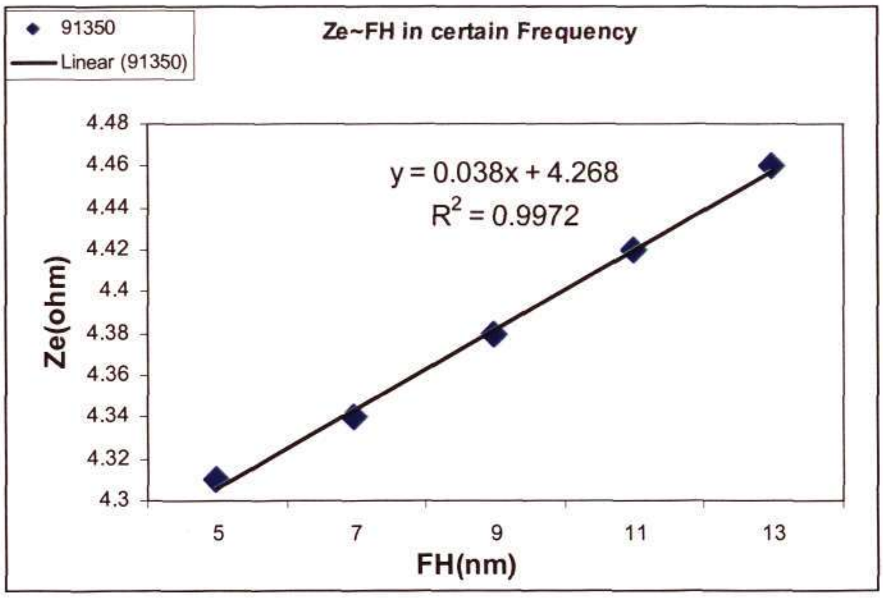

Fig. 4-22 Ze~FH in frequency=91350Hz

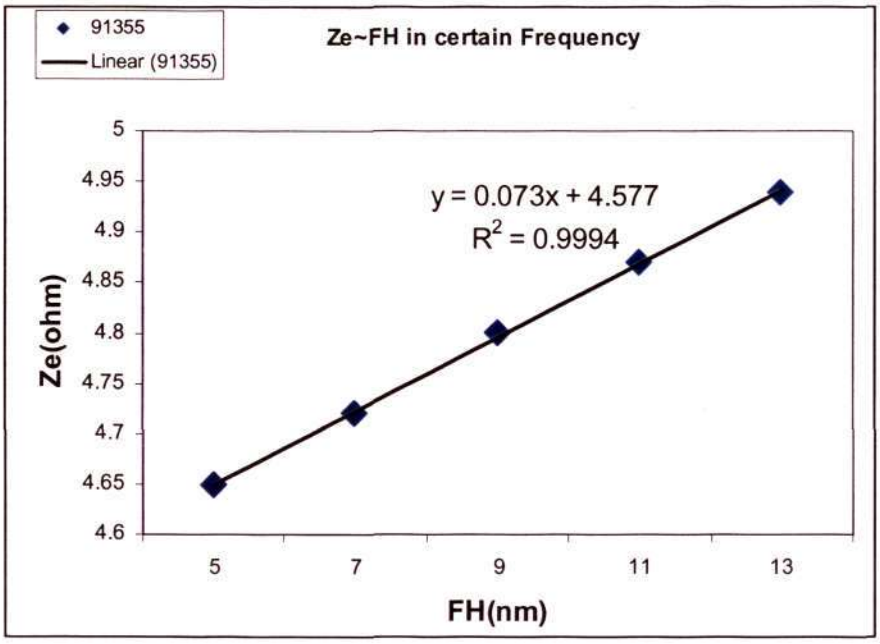

Fig. 4-23 Ze~FH in frequency=91355Hz

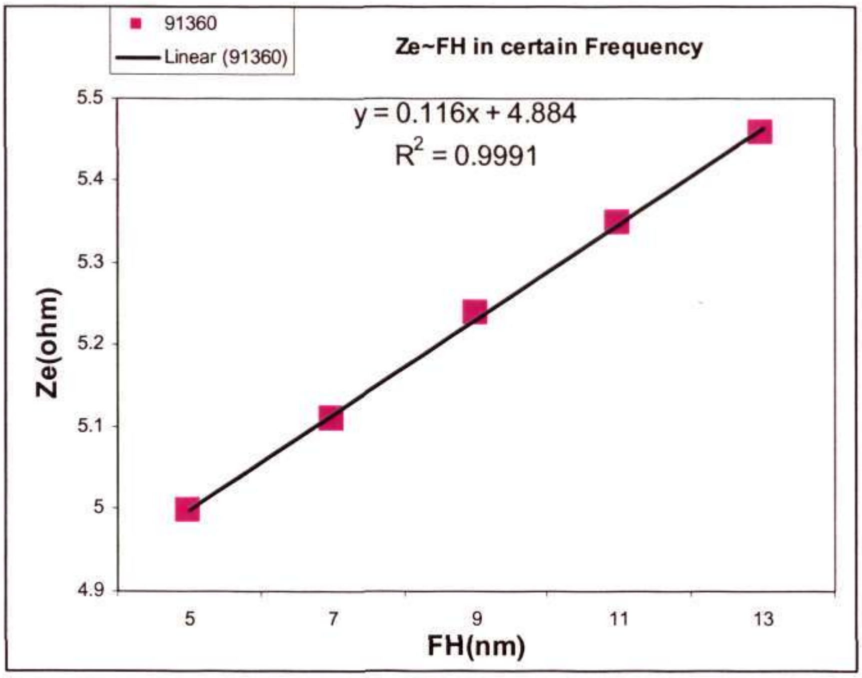

Fig. 4-24 Ze~FH in frequency=91360Hz

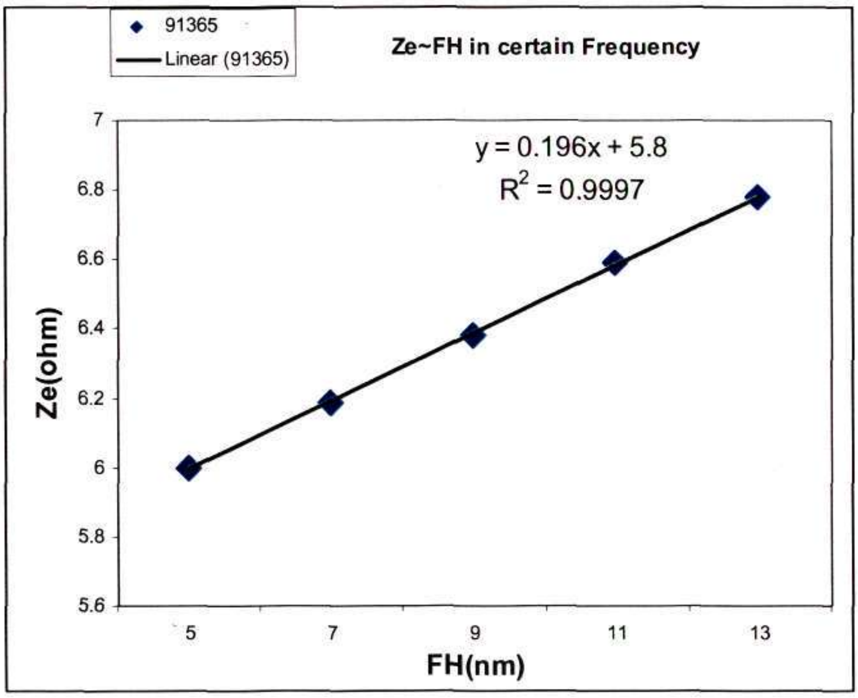

Fig. 4-25 Ze~FH in frequency=91365Hz

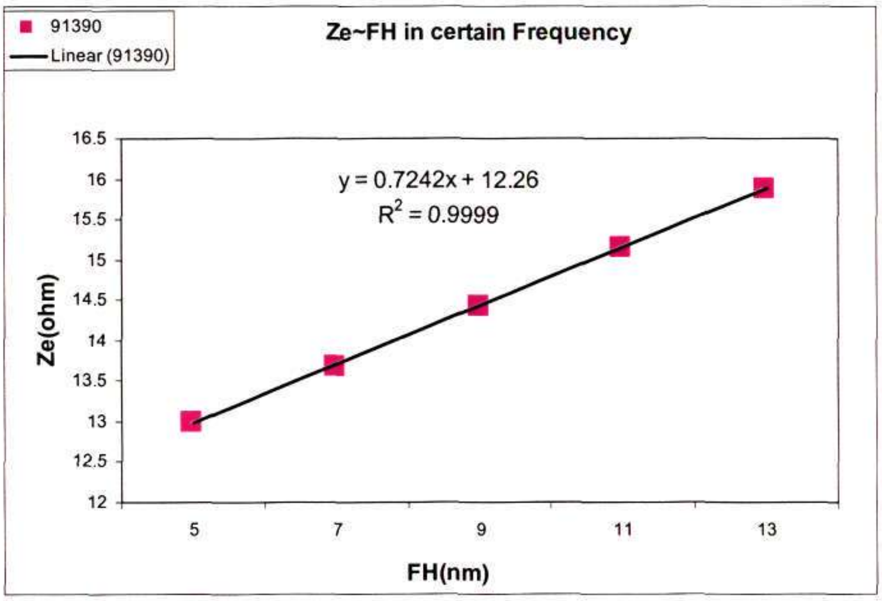

Fig. 4-26 Ze~FH in frequency=91390Hz

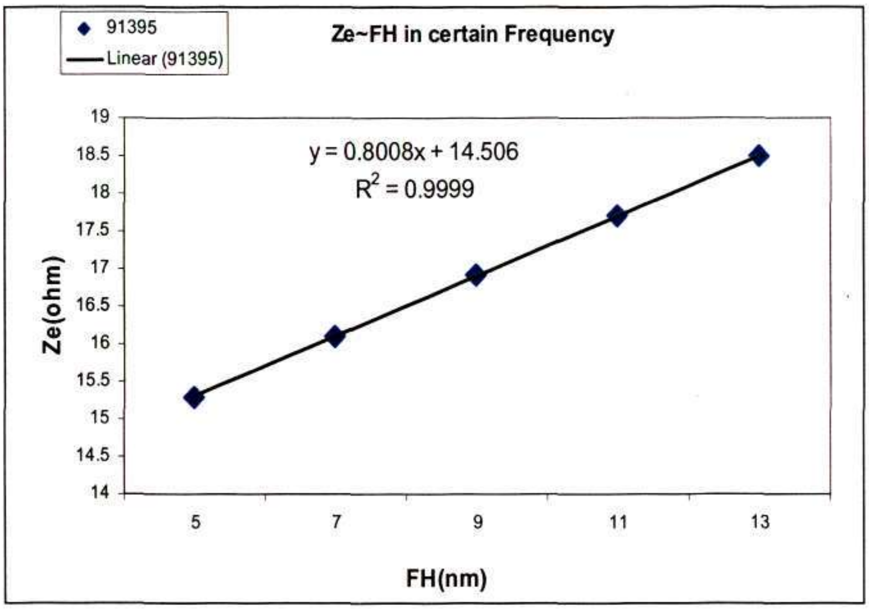

Fig. 4-27 Ze~FH in frequency=91395Hz

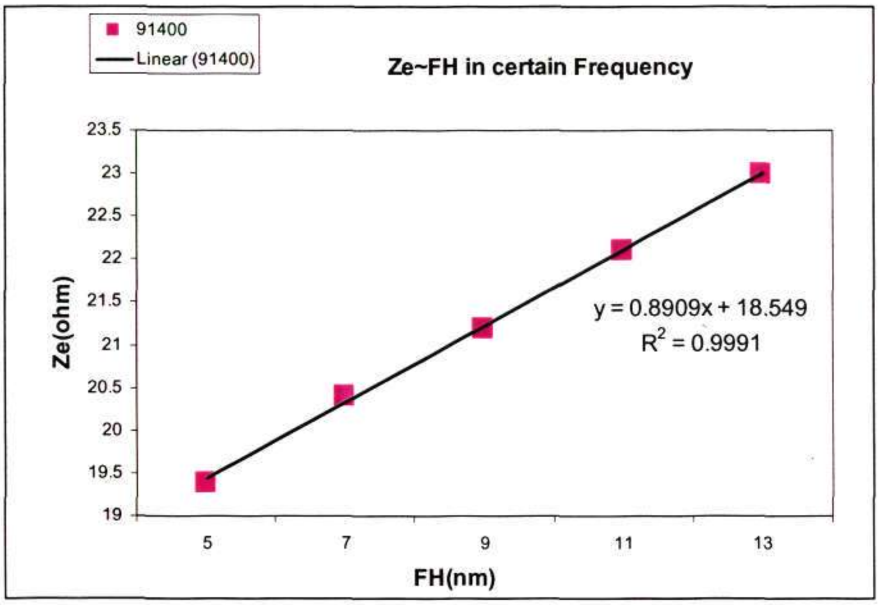

Fig. 4-28 Ze~FH in frequency=91400Hz

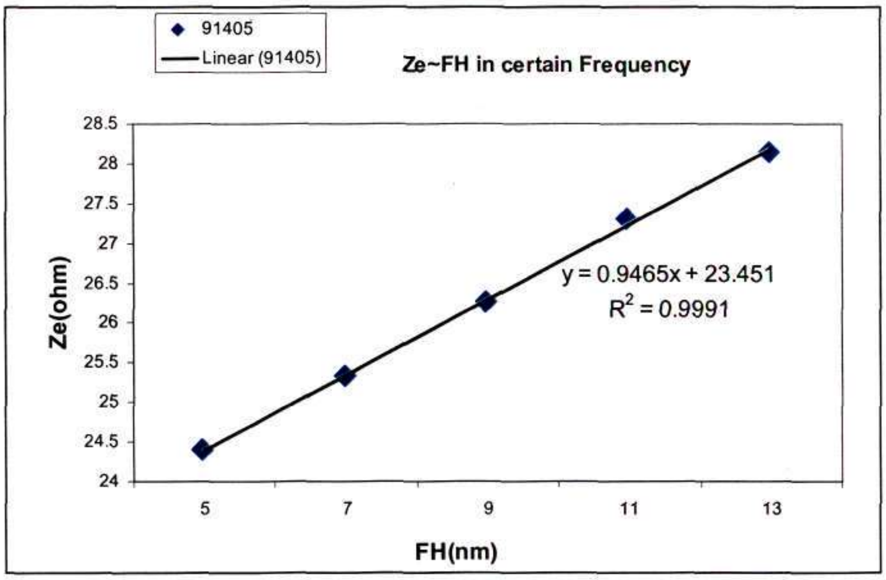

Fig. 4-29 Ze~FH in frequency=91405Hz

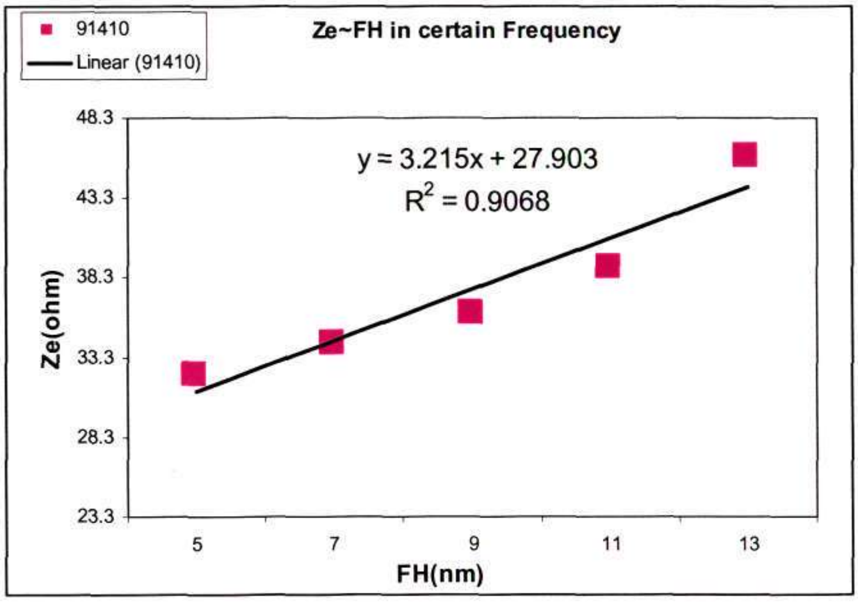

Fig. 4-30 Ze~FH in frequency=91410Hz

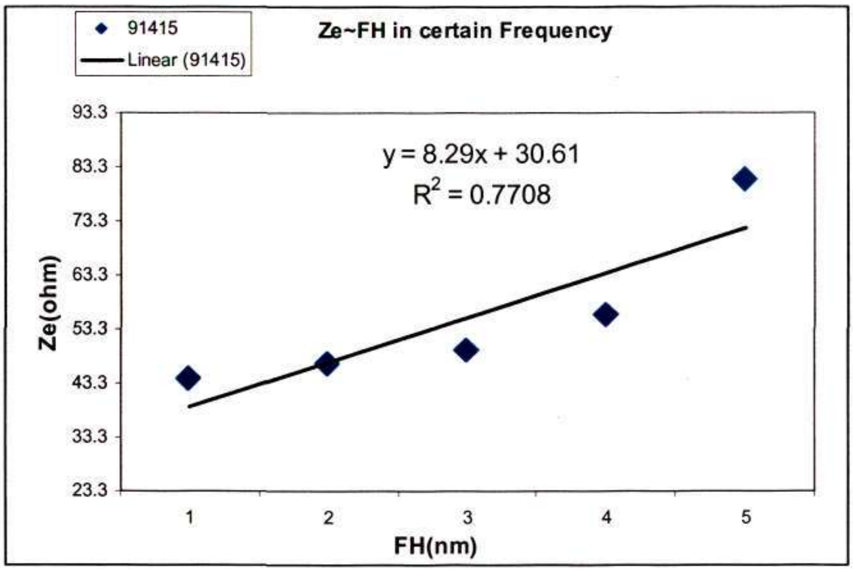

Fig. 4-31 Ze~FH in frequency=91415Hz

Table 4-6 (A) Summary of results (1)

Frequency	91350 Hz	91355 Hz	91360 Hz	91365 Hz
Relationship (x=FH, y=Ze)	y=0.038x+4.268	y=0.073x+4.577	y=0.116x+4.884	y=0.196x+5.8
R^2	0.9972	0.9994	0.9991	0.9997
Sensitivity (ohm/nm)	0.038	0.073	0.116	0.196

Table 4-6 (B) Summary of results (2)

Frequency	91390 Hz	91395 Hz	91400 Hz	91405 Hz
Relationship (x=FH, y=Ze)	y=0.7242x+12.26	y=0.8008x+14.506	y=0.8909x+18.549	y=0.9465x+23.451
R^2	0.9999	0.9999	0.9991	0.9991
Sensitivity (ohm/nm)	0.7242	0.8008	0.8909	0.9465

Table 4-6 (C) Summary of results (3)

Frequency	91410 Hz	91415 Hz
Relationship (x=FH, y=Ze)	y=3.215x+27.903	y=8.29x+30.61
R^2	0.9068	0.7708
Sensitivity (ohm/nm)	3.215	8.29

The comparisons of the sensitivity of the PZT cantilever obtained from ANSYS and that obtained from our developed FE program are shown in Figure 4-32 and 4-33. On the one hand, it is obviously seen that the sensitivity obtained from the FE program is lower than that obtained from ANSYS if the driven frequency is same. The difference is about 4%. This difference is suspected to be caused by, 1) the three coupling fields are solved simultaneously in FE program, and they are solved step by step in ANSYS, and 2) the air bearing model used in FE program is FK model instead of general fluid model, and the air bearing is regarded as compressible air in FK model, but air bearing is regarded as uncompressible air in ANSYS. On the other hand, the magnitude from FE program is larger than that from ANSYS. This is obviously caused by the compressible effect which has been considered in the FE program. The interaction between compressible air and cantilever is larger than that between normal air and cantilever.

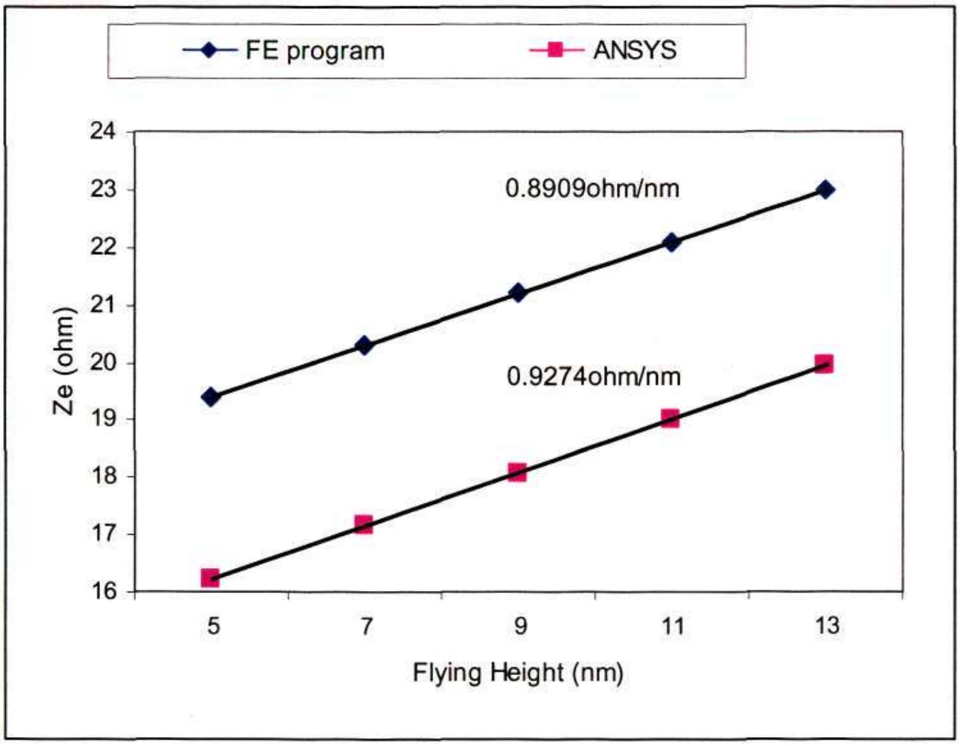

Fig. 4-32 Ze~FH (Freq. = 91400 Hz)

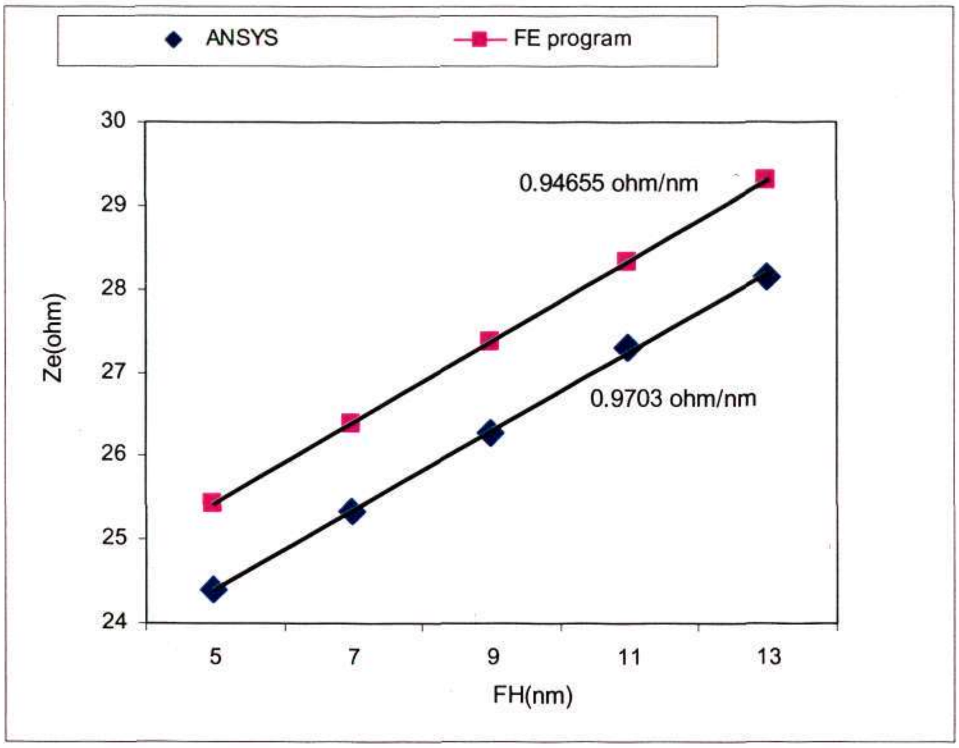

Fig. 4-33 Ze~FH (Freq. = 91405 Hz)

4.3 Conclusions

From above study, it can be concluded that:

1) FE package has been used to study the capability of the sensor, which consists of a cantilever and a patch of PZT. The results show that the sensor is capable of realizing in-situ flying height measurement. The calculated results show there is a good linear relationship between the output electrical impedance and flying height.
2) The sensitivity of this sensor becomes large as the voltage driving frequency become large. It can reach about 0.9465 ohm per nanometer when the sensor keeps a good linearity at the same time. The study also shows that the sensitivity will be larger when frequency is closer to natural frequency of cantilever, but the linearity is not very good when the driving frequency is near resonant frequency.
3) There are signs of nonlinearity between flying height and electrical impedance when the driving frequency is close to the resonant frequency of the cantilever. So we must do a tradeoff between sensitivity and linearity when we choose the working frequency for the sensor.
4) There is a little difference between results form FE program and ANSYS, this difference reaches about 4%.

Chapter 5

Virtual Testing of In-Situ Mechanical Impedance Measurement Capability of New Slider Design

It is well known that mechanical behavior of head disk interface (HDI) plays an important role when designing a hard disk drive. For example, the mechanical impedance and the stiffness of air bearing could give us a clear view of the whole dynamic performance of the hard disk drives. Especially in the failure analysis for a hard disk drive, it is urgently required that we could know these mechanical properties before we tear down the failed hard disk drive. So an in-situ measuring mechanical impedance or stiffness of air bearing is come into being and will be introduced in this Chapter.

One major reason of lack of understanding of mechanical behavior of air bearing is the difficulties of currently measuring this property when the hard disk drive is in operation state. Typically, the first mode of natural frequency of the air bearing at its lowest FH is around 100K Hz. At such a high frequency, the velocity at the tip of the cantilever can only be measured with Laser Doppler Vibrometer considering the very small space available for installing any conventional motion sensor, not mentioning the fatal loading effect may well be caused by these sensors. As for measuring the force existing at the same interface, in addition to the same constraints existing for motion measurement, the high operating frequency actually prohibits the use of any existing load cell. Few attempt of measuring this force has ever been reported in literature.

In Chapter 4, the proposed slider design with in-situ flying height measurement capability has been presented. It demonstrated that the electrical impedance of the PZT is closely linearly correlated with flying height. Originated from the application of this cantilever together with the PZT, SSA method is introduced and the four-pole model is built for head disk interface. The four-pole model gives us a way to measure the mechanical impedance of the air bearing. Figure 5-1 shows the sketch of the slider design. In this slider, the flying height is determined by the major part of the slider – slider body. The cantilever, together with PZT is mainly used to measure mechanical impedance of air bearing.

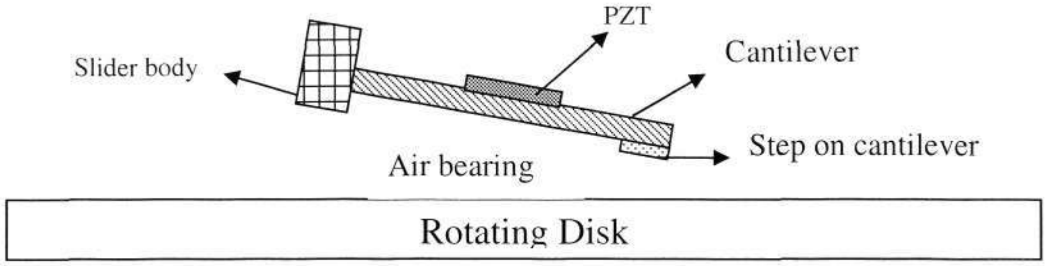

Fig. 5-1 Sketch of slider flying above rotating disk

In order to detect the mechanical impedance of air bearing at the centre of step, simultaneous sensing and actuation (SSA) method is used, which has been introduced in Chapter 2. In this method, the input and output variables of the sensing mechanism are connected with a transduction matrix. Once the transduction matrix is identified, the output variables could be calculated from the input variables.

So, the transduction matrix, which correlates with air bearing and the cantilever together with PZT film, will be firstly identified through numerical simulations. The force and velocity at centre of step are then obtained and thus the mechanical impedance of air bearing is calculated. In this study, we will focus on the force and velocity acting on the centre point of the step. This is another form of studying the mechanical impedance of air bearing at the centre point of the step.

5.1 Four-pole Model of PZT Cantilever and Air Bearing

As described earlier, the cantilever together with PZT film, shown in Figure 5-2, acts as a two-port device. The input port is where the electrical voltage is supplied. The output port is the centre of step on the cantilever.

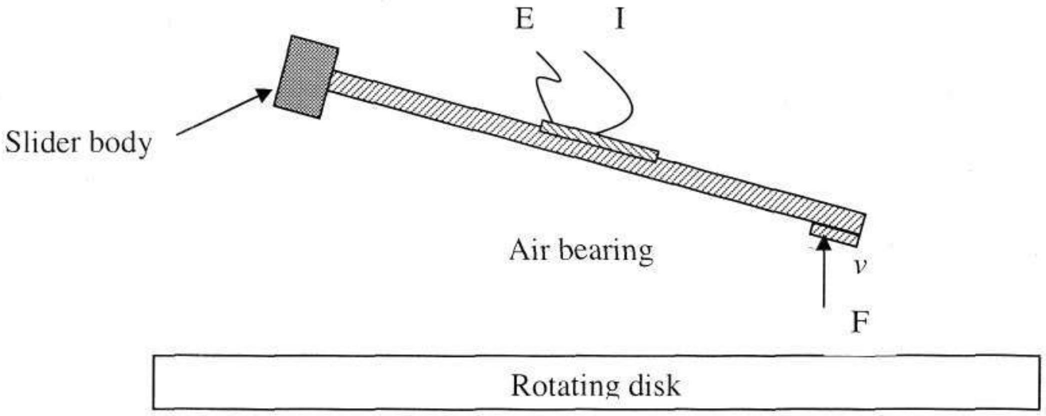

Fig. 5-2 Head disk interface with novel slider design

The four-pole model of transducer system is shown in Figure 5-3. The input variables are voltage and current of the PZT, while the output variables are output force and velocity at tip of the cantilever. The four-pole is like a black box. The PZT film and the cantilever are hidden in the black box. The input and output variables are connected with a transduction matrix T as in Equation 5-1, which is the characteristic of the sensor.

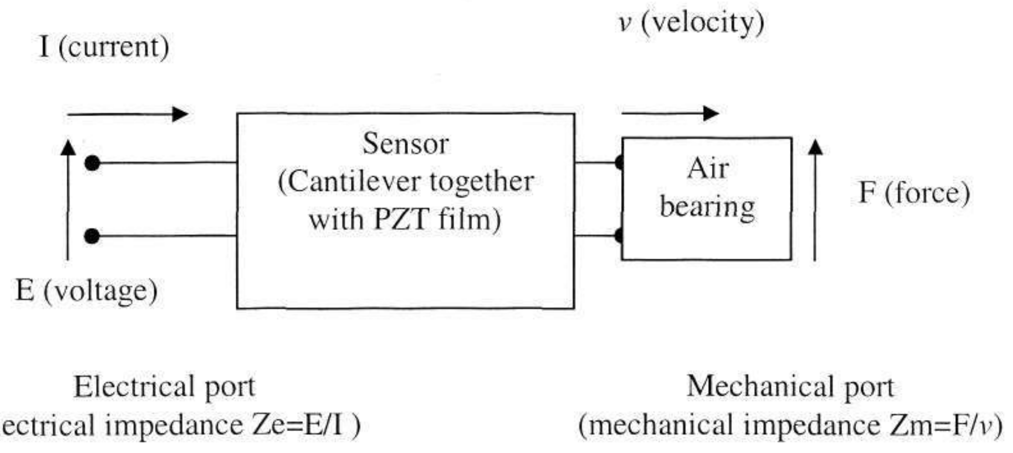

Fig. 5-3 Transduction system of cantilever with PZT film

$$\begin{bmatrix} E \\ I \end{bmatrix} = [T]\begin{bmatrix} F \\ v \end{bmatrix} = \begin{bmatrix} T_{11} & T_{12} \\ T_{21} & T_{22} \end{bmatrix}\begin{bmatrix} F \\ v \end{bmatrix}, \tag{5-1}$$

Here, E is the input voltage of the PZT,

I is the input current of the PZT,

F is the output force at centre of step on the cantilever,

v is the output velocity at centre of step on the cantilever.

It is clear that there is no internal energy resource in the transducer system of the cantilever together with PZT. Furthermore, from the construction of the transducer, it is reasonable to assume the system is linear. Thus, the transfer function must satisfy the following condition:

$$T_{11}T_{22} - T_{12}T_{21} = 1. \tag{5-2}$$

Once the transduction functions T_{ij} are made known from Equation 5-1 and Equation 5-2, it can be seen that the force and velocity at the output port of the transducer can be evaluated by

$$\begin{bmatrix} F \\ v \end{bmatrix} = \left[T^{-1}\right]\begin{bmatrix} E \\ I \end{bmatrix} = \begin{bmatrix} T_{22} & -T_{12} \\ -T_{21} & T_{11} \end{bmatrix}\begin{bmatrix} E \\ I \end{bmatrix}. \tag{5-3}$$

And the mechanical impedance could be evaluated from electrical impedance Z_e by equation (5-4) as shown below.

$$Z_m = \frac{F}{v} = \frac{T_{22}E - T_{12}I}{-T_{21}E + T_{11}I} = \frac{T_{22}Z_e - T_{12}}{-T_{21}Z_e + T_{11}} \tag{5-4}$$

In general, each of the 4 elements of the transduction matrix, T_{ij}, is a complex function of frequency. The modulus and phase of these transduction functions indicate the amplitude ratio and the phase difference between an input variable and an output variable of the transducer respectively.

For a whole system including cantilever, PZT film and air bearing, as the transducer is designed to operate at its resonance frequency, nearly all input energy is controlled to transmit at this frequency. As such, transduction functions for the actuating mechanism of the cantilever together with PZT should be studied at the operating frequency only. Therefore, the transduction matrix, T_{ij}, contains only 4 complex numbers, which are the specific values of the general transduction matrix at the operating frequency. Simultaneously, the identification of the transduction matrix is also simplified to identify the four-pole parameters at the operating frequency only. In the following section, the identification method of transduction matrix is given.

5.2 Transduction Matrix of Cantilever together with PZT

As discussed in the last section, the head disk interface could be modeled as a two-port system when the proposed slider design is flying above the disk. The input port is on the PZT side, the output port is on centre of step on the cantilever. These two ports represent the ABS's mechanical behavior, as shown in Figure 5-2. The method to identify the transduction matrix of cantilever together with PZT is given in this section.

From Equation 5-1 and 5-2, we can see that it takes only three independent equations for the identification of the transduction matrix. Under this consideration, we create two operating conditions to get the independent equations.

Firstly, we let the cantilever fly statically. That means the output force at centre of step of cantilever, F, is set to be zero. Thus Equation 5-1 becomes

$$\begin{bmatrix} E \\ I \end{bmatrix} = \begin{bmatrix} T_{11} & T_{12} \\ T_{21} & T_{22} \end{bmatrix} \begin{bmatrix} 0 \\ v \end{bmatrix} = \begin{bmatrix} T_{12}v \\ T_{22}v \end{bmatrix}. \tag{5-5}$$

With the measurement of the voltage, the current and the velocity, T_{12} and T_{22} are identified:

$$T_{12} = \frac{E}{v}\Big|_{F=0}\text{, and} \tag{5-6}$$

$$T_{22} = \frac{I}{v}\Big|_{F=0}. \tag{5-7}$$

Next, we let the cantilever is under force. Under this condition, v is set equal to zero.

$$\begin{bmatrix} E \\ I \end{bmatrix} = \begin{bmatrix} T_{11} & T_{12} \\ T_{21} & T_{22} \end{bmatrix} \begin{bmatrix} F \\ 0 \end{bmatrix} = \begin{bmatrix} T_{11}F \\ T_{21}F \end{bmatrix} \tag{5-8}$$

With the measurement of the voltage, the current and the force, T_{11} and T_{21} are identified:

$$T_{11} = \frac{E}{F}\Big|_{v=0}\text{, and} \tag{5-9}$$

$$T_{21} = \frac{I}{F}\Big|_{v=0}\,. \tag{5-10}$$

As there is few research on such a SSA method and it is hard to carry out experiment, finite element method (FEM) is used to model this system and get the transduction matrix. In the last two chapters, a FE procedure has been developed and only a minor modification is required to carry out the analysis of the four-pole model.

Figure 5-4 shows the one-dimensional finite element model of the flying cantilever together with PZT film above the rotating disk. In this FE model, some features, parameters and boundary conditions are:

1) the cantilever is divided into 40 elements, including total 41 nodes, shown in circles,

2) the PZT is divided into 4 elements, including 5 nodes, which are interconnected with cantilever's elements, the common elements are shown as star,

3) node (39), (40) and (41) are the elements to form the step of cantilever,

4) the input port is the PZT elements, including nodes from (19) to (23),

5) output port is at node (40),

6) node (1) is fixed,

7) length of cantilever and PZT is 0.5mm and 0.05mm respectively,

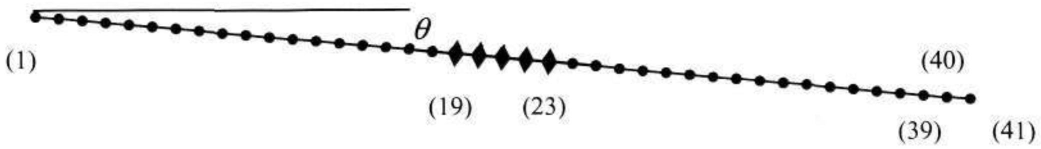

Fig. 5-4 Finite element model of cantilever and PZT in one-dimensional

From the derivation from Equation (5-6) and (5-9), the elements inside the transduction matrix could be achieved. Under the first condition, T_{12} and T_{22} could be achieved by letting a sine voltage (amplitude is 0.01 volt) being applied to the input port of PZT while the output port node (40) be free (F=0). Thus the response current I and v could be obtained. Wit Equation (5-6) and (5-7), T_{12} and T_{22} are identified. Figure 5-5 and 5-7 show the T_{12} and T_{22} respectively. Under the second condition, T_{11} and T_{21} could be achieved by letting a sine voltage (amplitude 0.01 volt) being applied to the PZT while the output port node (40) be fixed. T_{11} and T_{21} are identified and shown in Figure 5-6 and 5-8 respectively.

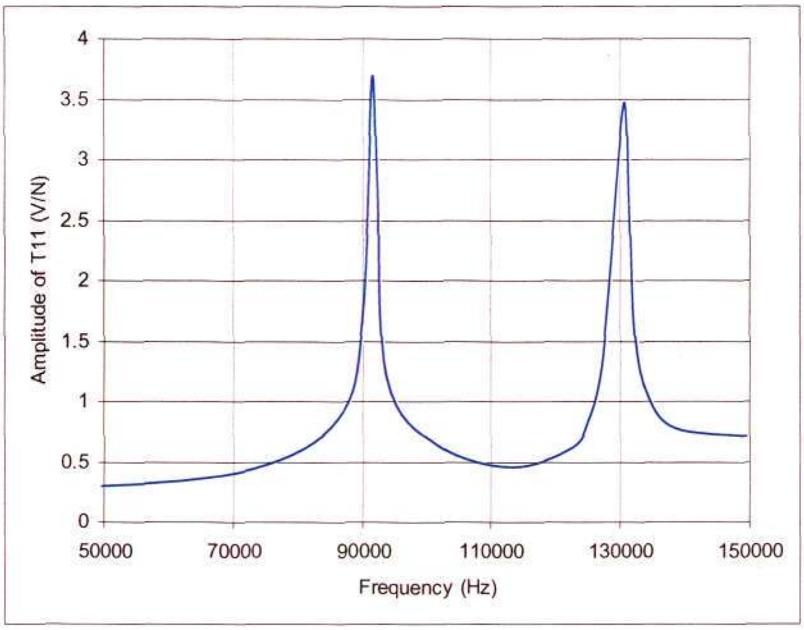

Fig. 5-5 Amplitude of T_{11}

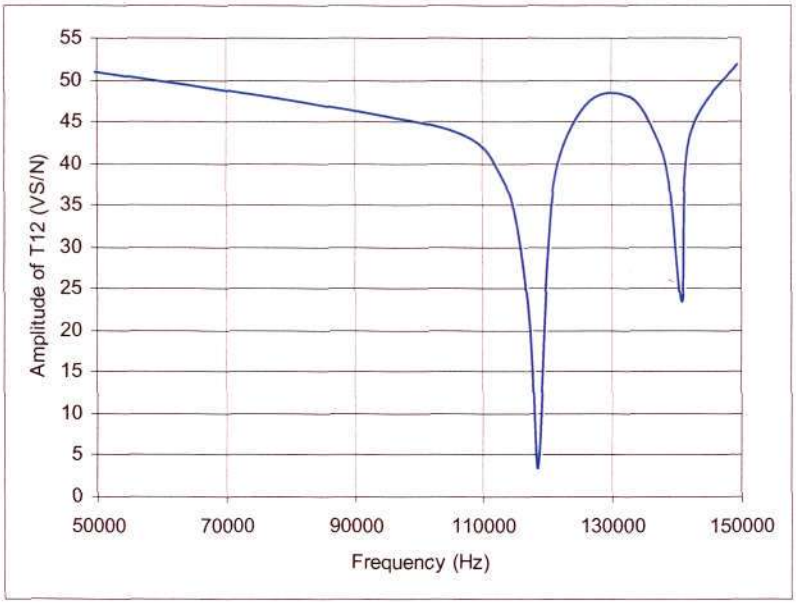

Fig. 5-6 Amplitude of T_{12}

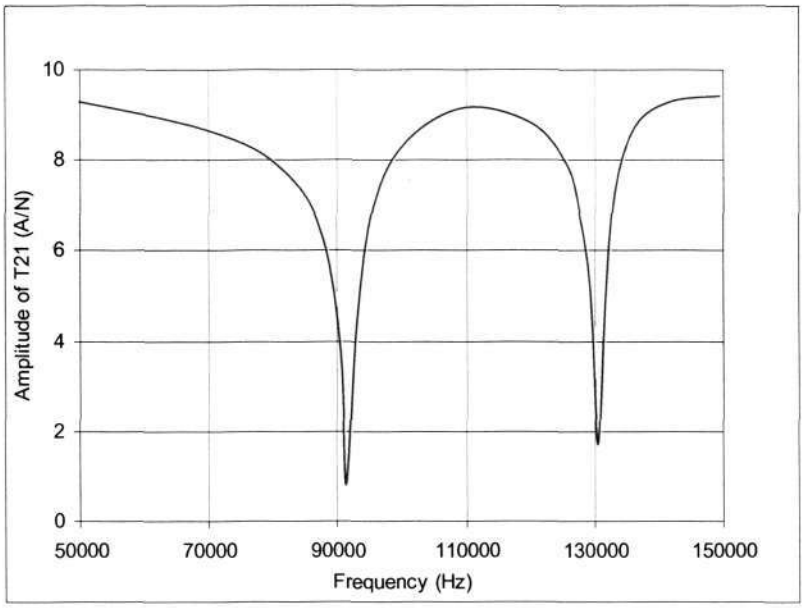

Fig. 5-7 Amplitude of T_{21}

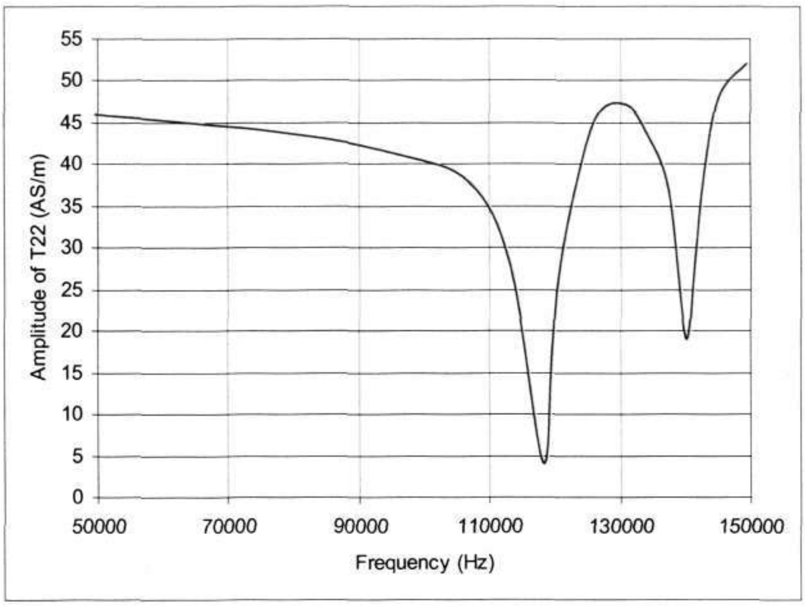

Fig. 5-8 Amplitude of T_{22}

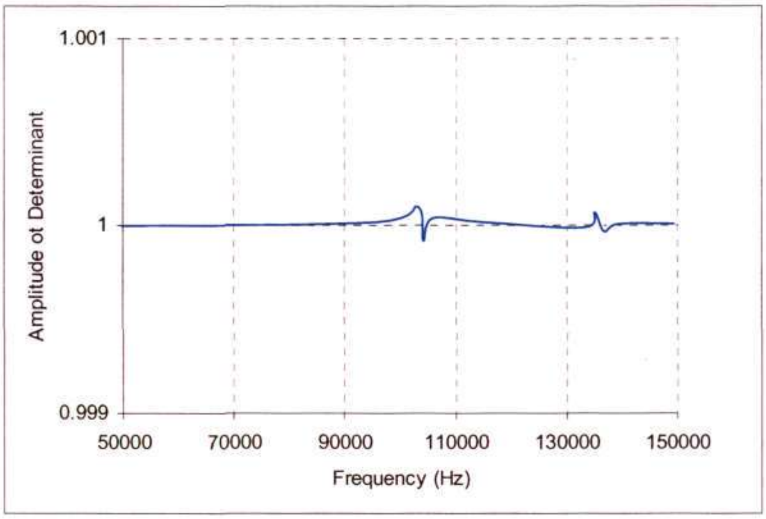

Fig. 5-9 Amplitude of determinant

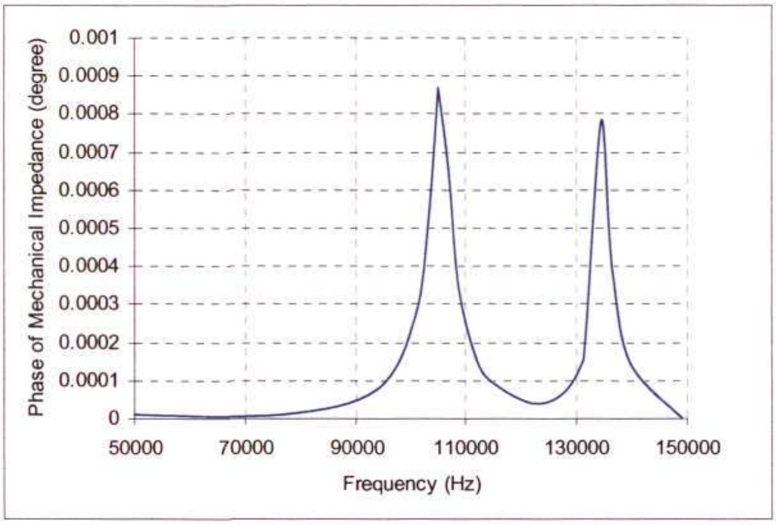

Fig. 5-10 Phase of determinant

From Figure 5-5 to 5-8, the four elements inside the transduction matrix have been retrieved by our finite element package. Figure 5-9 and 5-10 shows that the determinant of transduction matrix is nearly unit. It has 2 peaks near the natural frequency of cantilever. The cantilever, together with the patch of PZT, has been proved to be effectively and correctly modeled by four-pole model. The performance of this model is good. From the above study, we could see that the four elements inside the transduction matrix are shown as Equation (5-11) to (5-14) respectively. Units for T_{11}, T_{12}, T_{21}, T_{22} are $V/N, V\cdot s/N, A/N, A\cdot s/N$ respectively.

$$T_{11} = 1.347 + 0.453i \tag{5-11}$$

$$T_{12} = 39.346 - 13.455i \tag{5-12}$$

$$T_{21} = -1.455 + 0.454i \tag{5-13}$$

$$T_{22} = 41.932 - 11.783i \tag{5-14}$$

So the transduction matrix could be rewritten as equation (5-15).

$$T = \begin{bmatrix} 1.347 + 0.453\cdot\mathrm{i} & 39.346 + -13.455\cdot\mathrm{i} \\ -1.455 + 0.454\cdot\mathrm{i} & 41.932 - 11.783\cdot\mathrm{i} \end{bmatrix} \tag{5-15}$$

From the above study, the mechanical impedance could be retrieved by the input electrical impedance as Equation (5-4) if the transduction matrix has been identified. In the next section, we will carry out the measurement of mechanical impedance at the centre of the step node (40) of cantilever by this four-pole model.

5.3 Measurement of Mechanical Impedance of Air Bearing

From this above study, the transduction matrix for the four-pole model of the sensor (including cantilever together with the patch of PZT) has been obtained. In this method, the sensor will be used to measure the mechanical impedance of air bearing. In Figure 5-1, when the slider is flying above the disk surface, air bearing is formed between slider and the disk. The mechanical impedance of air bearing is defined as the ratio of force over velocity at the centre of the step of the cantilever, $Z_m = F/v$. To measure the mechanical impedance of air bearing, a certain voltage (amplitude is 0.01 V) is applied to the PZT. Measuring the electrical impedance from the PZT, then we could get the mechanical impedance of the air bearing by the transduction matrix. Figure 5-11 shows the results comparing with that from Paul's [64].

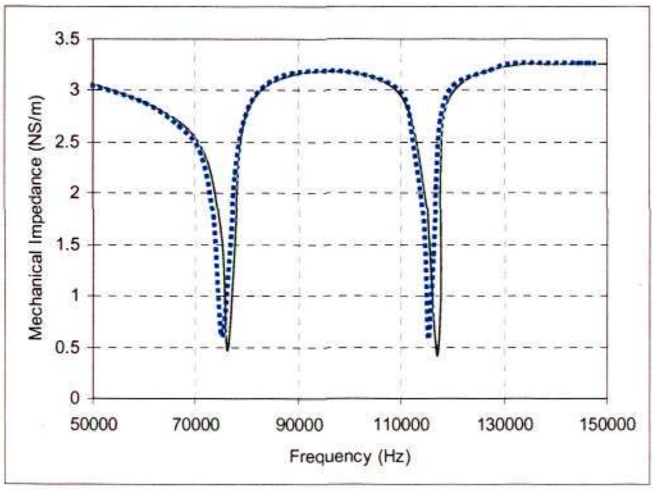

Fig. 5-11 Mechanical impedance of air bearing with pitch angle $\theta = 2\mu rad$

In this figure, the dot line shows the results retrieved from four-pole model and the bold line shows results from Paul. The shapes of these two curves are close each other, while there is some difference around the resonant frequency. There are three sources of the difference. The first one is the model of finite element models. As this is only a one-dimensional model, but the actual structure of this sensor and air bearing are in tri-dimensional. The second is the average process of force calculation on the step of node (40). The last one is the average process of the velocity on the step on node (40). Figure 5-12 and 5-13 shows the comparison results when we change the pitch angle of cantilever from 2urad to 3urad, 4 urad respectively. Difference between calculated from four-pole model and existing one becomes large around the peak when the pitch increases. Large difference may come from these two facts, 1) increasing pitch will increase the interaction between cantilever and air bearing, 2) increasing interaction will increase the vibration of the cantilever, thus increases the nonlinearity in the system. However, the curves are enough to verify the SSA method and the usage of the four-pole model for the cantilever together with the PZT. From this comparison, it is obviously seen that the sensor (cantilever together with PZT) offers us a good and effective way to realize in-situ mechanical impedance measurement of air bearing in hard disk drive.

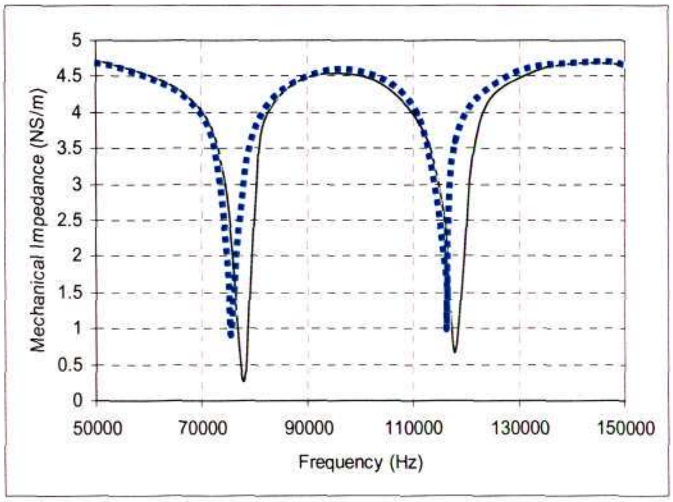

Fig. 5-12 Mechanical impedance of air bearing with pitch angle $\theta = 3\mu rad$

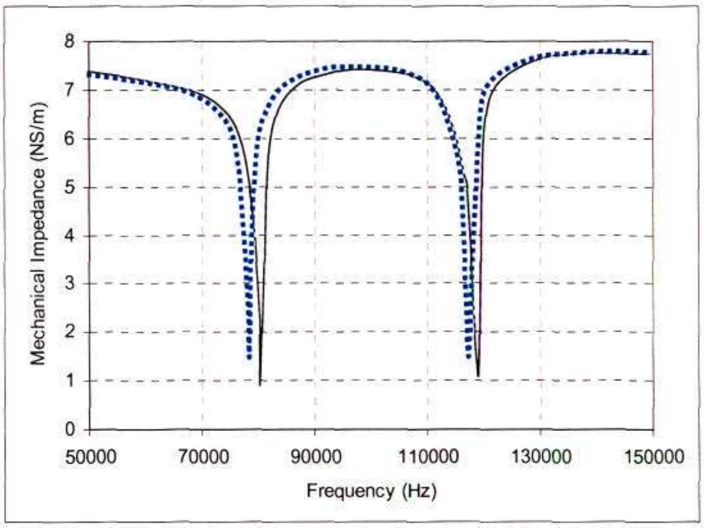

Fig. 5-13 Mechanical impedance of air bearing with pitch angle $\theta = 4\mu rad$

The traditional methods for mechanical impedance measurement of air bearing are mainly carried out by LDV, in which a special experimental setup is required. And these methods could not fulfill the in-situ mechanical impedance measurement when the disk drive is in the working state. In our new method, the mechanical impedance of air bearing could be obtained even the hard disk drive is in the working state. There is no complex measurement setup used in this new method. Thus, the PZT cantilever gives us a convenient and effective way to fulfill the in-situ mechanical impedance measurement of air bearing.

5.4 Realization of New Slider Design for Actual Testing

In the study from Section 5.1 to 5.3, and the study in Chapter 4, we focused on the virtual testing or numerical simulation on the in-situ measurement capability of flying height and mechanical impedance for the new slider design. All these virtual testing results have successfully proved the proposed slider to be a novel design with in-situ measurement capability of flying height and mechanical impedance of ABS. To carry out a further study of the new slider design in reality, MEMS fabrication of the new slider has been carried out. At the same time, an experimental setup has been designed to carry out actual test for the slider. The fabrication of MEMS-based slider includes eight main steps:

1) The thin walls are formed by a deep reaction ion etching (DRIE) method.

2) The bottom electrode is deposited by sputtering and patterned by a lift-off process.

3) A PZT thin film is deposited by sol-gel spin coating with commercial Mitsubishi E-Series solution and patterned by wet etching.

4) The upper electrode is deposited and patterned by the same method as that was used on the bottom electrode.

5) A layer of silicon dioxide is deposited on top of slider.

6) The shadow step of ABS is formed by DRIE.

7) The cantilever and slider are released from its front side by DRIE process.

8) The cantilever and slider are released by DRIE from back side by DRIE process.

Table 5-1 shows fabrication process of the slider. Refer to appendix for more detailed.

Table 5-1 Main fabrication process flow of MEMS-based slider

Sequence.	Fabrication	Thickness (um)	Deposition Method	Etching Method
1	Wafer cleaning			
2	Forming thin walls	5		DRIE
3	S_iO_2 deposition	0.5	Thermal oxide	
4	Bottom electrode	Ti (0.05)/ Pt (0.15)	Sputtering	Lift-off
5	PZT	0.7	Sol-gel	PZT etching solution
6	Upper electrode	Ti (0.05)/ Pt (0.15)	Sputtering	Lift-off
7	S_iO_2 deposition	0.5		
8	Back side S_iO_2 etching	0.5		Wet etching
9	Shadow step of ABS etching	0.5		DRIE
10	Front S_iO_2 etching	1(=0.5+0.5)		Wet etching
11	Front bulk Si etching	145(=150-5)		DRIE
12	Back bulk Si etching	150(=300-150)		DRIE

The fabrication detailed and results are shown in the appendix of this thesis. This slider fabrication has not been successful due to the limitation of lab equipments and time. The other reasons of the uncompleted MEMS fabrication will be also shown in the appendix. This uncompleted slider fabrication caused that the in-situ measurement capability of new slider design is validated by virtual testing, but not by actual testing. Even the slider fabrication is not complete, the technique and the experience during MEMS fabrication indeed will be of considerable interest to the following researchers.

5.5 Conclusions

From the above study, the mechanical impedance of air bearing has been obtained by the sensor, which consists of a cantilever and thin film of PZT. The results obtained from our FE package have a good consistency with others'. This consistency validates that the PZT cantilever can be used as a useful sensor to study the mechanical behavior of air bearing accurately. Comparing with current tools or methods (LDV, etc), the PZT cantilever shows much better than other tools because 1) lighter loading effect, 2) real-time measurement and 3) simpler measurement system. In section 5.4 description of a rough scheme of the MEMS-based slider fabrication has been given, which will indeed be interest to the following researchers even this slider fabrication is not completed due to limitation of lab equipments and time.

Chapter 6

Conclusions and Remarks

6.1 Conclusions

As a key parameter in the hard disk drive design, the flying height is usually designed as small as possible to increase the areal density of the disk. The smaller the flying height could be obtained, the larger areal density the disk drive could be achieved. On one hand, the flying height is decreased to improve the disk capacity. On the other hand, small flying height will increase the possibility of head disk interaction. The head disk interaction will cause the disk drive to fail and it must be avoided. A good way to avoid the head disk interaction is to control the flying height. To control flying height, it should be known firstly. Flying height measurement in HDD has been studied in detailed and it was carried out off-line by many traditional methods. Unfortunately, there is lack of study on the in-situ flying height measurement due to its complexity, which is a complex project with multiple subjects (fluid, vibration, electrical and mechanical structure, etc) involved.

In this study, a simultaneous sensing and actuation (SSA) method has been developed to study the in-situ flying height measurement capability of a new slider design. In this new slider design, a flexible cantilever is built to carry the read/write head at its tip. The flexible cantilever, of which a PZT film coated onto its top surface, is flying above the disk surface when HDD is in the working state. The flying cantilever, PZT film and air bearing have been simulated as a finite element model using ANSYS. In this study, the air bearing is simulated as lots of spring elements by assuming this kind of air bearing follow the governing equation of FK model. By applying several assumptions and boundary conditions which are similar to actual working conditions to the finite element model, the PZT cantilever is actuated by a small voltage under a prescribed frequency. The flying height has been proved and has been obtained from the input electrical impedance of PZT. The sensitivity could reach 1.048ohm per nanometer. From this study, the new slider design has been proved to be capable of in-situ flying height measurement capability. As ANSYS could not simulate the PZT, cantilever and air bearing simultaneously, a well established finite element procedure is developed which simultaneously includes the cantilever, PZT and air bearing. To develop this finite element procedure, the finite element matrix for cantilever, PZT and air bearing has been successfully derived respectively. Several simplified model has been used to validate the correctness of the developed FE procedure. The pressure distribution of air bearing obtained from this procedure agrees quite well with the other researches' results. Using this procedure, the in-situ flying height capability of the new slider design has been studied and the results also have shown that there is good relationship between the input electrical impedance of PZT and flying height.

Beside the study of the in-situ flying height measurement capability of the new slider design, the study of the in-situ measurement of mechanical impedance of air bearing has been successfully carried out by using this finite element procedure. In this study, the

PZT cantilever is viewed as a four-pole device which possesses a unique transduction matrix correlating the electrical input variables of the PZT and the mechanical output variables at the tip of the cantilever. The transduction matrix is identified by the well established finite element procedure. Thus, the mechanical impedance of air bearing on the tip of PZT cantilever is obtained from the input voltage and current of the PZT. So, we attained a useful and effective tool to study the mechanical behavior of the air bearing for the new slider design.

With a good study on the in-situ flying height measurement and in-situ mechanical impedance measurement, the new slider has been designed in detailed with a PZT cantilever inside it. The new designed slider has been fabricated by MEMS technique. Before the fabrication, the mask design has been carried out for the new slider. There are 8 layers inside this design, so 8 masks are required. With so many layers and masks, to align them to be coincident is a difficulty due to the small dimension of themselves. The feature dimension of these masks is 5 um. And more, the solution of PZT could only be bought from Japan, it will spend about 3-5 month for the order. When we are going to fabricate this new slider, the project's time limit is also coming. At last, the fabrication of the slider could not go on well and the fabricated slider could not run well. Even that, the new slider has shown a good performance with in-situ flying height measurement capability by virtual testing and numerical simulation, and the mask design shows effective during fabrication. These would greatly help others about the new slider fabrication from design aspect. All in all, the below items briefly summarize the main contributions, achievements and limitations from the PhD study.

1. It was the first time in the world that the SSA method was introduced and applied in hard disk drive design. The four-pole model of the cantilever together with PZT film has been built by finite element method. The performance of the cantilever with PZT film as a sensor for in-situ flying height measurement has been validated and it shows a good performance. By a well calibrated transduction matrix of the four-pole model being obtained by simulation, the mechanical impedance of the air bearing on tip of cantilever has been achieved by the input voltage and current of the PZT.

2. Based on the novel proposed slider, a finite element model including the cantilever, PZT film and air bearing has been built. In this FE model, it was the fist time in the world that the interaction between solid slider and air bearing was taken into account during slider design. The electrical impedance, which is the signal from the PZT, has been extracted and analyzed under different frequencies. From this work, we find out there is a good linear relationship between the electrical impedance and the flying height. The sensitivity can reach 1.048 ohm per nanometer when the driving frequency of voltage is not close to the natural frequency of cantilever.

3. Based on the traditional slider design in current industry, a new slider design has been proposed and designed. In this novel slider, a cantilever with PZT film coated onto its surface is used to fulfill the in-situ flying height measurement.

4. Different models of Reynolds equation have been discussed in detail. We can see that the FK model can predict the slider's behavior more accurately. Based on the FK model, the coupling field system between the fluid (air bearing) and structure (cantilever) has been solved by a self-developed finite element procedure. This procedure was written in MATLAB language. This finite element procedure gives us an effective tool for studying the in-situ flying height capability of the new slider.

5. The new slider has been designed and validated by numerical simulation. The fabrication of this slider is based on MEMS technology. A prototype is fabricated. Although it could not be fabricated well due to stringent condition required for slider fabrication, it shows a good research direction of the MEMS-base slider.

6. The limitation of this study is that we have not successfully fabricated a complete slider, with which the validation of our theoretical model and analysis could be carried out by physical experiment. The design, causes of failure fabrication and recommendations have been described in detailed in the Appendix, Attempt to Design and Fabricate the New Slider.

6.2 Remarks

This project is a multi-physics project, which includes fluid, vibration, electrical, thermal and mechanical structure or more. At the same time, even the SSA method has been attracted many research attentions and widely used in monitoring system etc, it is firstly applied in hard disk drive, which is a complex mechanical device. Thus, in the beginning of the PhD study, a lot of effort has been spent on the finite element modeling for the coupling field system including cantilever (mechanical), PZT (electrical) and air bearing (fluid). With this effort, the proposed slider design with in-situ flying height capability has been proved and it shows a good performance. Moreover, the in-situ mechanical impedance measurement capability has been validated by the finite element method. Even that, the following topics will be required to a further investigation:

1. All the work completed in this PhD study is one-dimensional and two dimensional, to attain more accurate results and learn more detail about the in-situ flying height measurement, the work will be suggested to be extended to be three-dimensional. The derivation of finite element matrix of the cantilever and the air bearing is suggested to be carried out in three dimensions.

2. In this PhD study, a finite element model for cantilever, PZT film and air bearing has been developed and analyzed numerically. Although simplified model has been used to validate this finite element model, it is suggested to carry out a practical model to validate this model in the future. For the objective of optimal design of the slider, a more robust and practical model is suggested to be studied.

3. Based on the SSA method, the four-pole model has been built for the cantilever, PZT film and air bearing. Using the transduction matrix of the four-pole model, it is easy for us to extract the mechanical impedance of the air bearing by the input electrical impedance. But it is not precisely enough for the optimal design of slider and measurement of air bearing's mechanical impedance, a practical model is needed and suggested to achieve more research effort.

References

[1] Arick. Menon, "Interface tribology for 100 Gb/in^2," Tribology International 33, pp299-308, 2000

[2] Lu, S., Hu, Y., O'Hara, M. and Bogy, D.B., Bhatia, C.S., and Hsia, Y.T., "Air bearing design, optimization, stability analysis and verification for sub-25nm flying," IEEE Transactions on magnetics, Vol. 32, No.1, pp103-109, 1996

[3] Menon AK, Gupta BK. "Nanotechnology: a data storage perspective," DataTech, 2:13-24, 1999

[4] Beskok, A. and Karniadakis, G.E., "Simulation of heat and momentum transfering complex microgeometries," Journal of Thermophysics and Heat Transfer, Vol. 8, No. 4, pp647-655, 1994

[5] Beskok, A., Karniadakis, G.E. and Trimmer, W. "Rarefaction, compressibility and thermal creep effects in micro-flows," DSC-Vol. 57-2, 1995 IMECE, Proceedings of the ASME Dynamic Systems and control Division, ASME, pp877-892, 1995

[6] Beskok, A., Karniadakis, G.E. and Trimmer, W., "Rerefaction and Compressibility Effects in Gas Microflows," Transactions of the ASME, Journal of Fluids Engineering, Vol. 118, pp448-456, 1996

[7] Beskok, A., "Simulation and models for gas flows in microgeometries," Ph.D thesis, Brown University, 1996

[8] Best, G.L., Horne, D.E., Chiou, A., and Sussner, H., "Precise Optical Measurement of Slider Dynamics." IEEE Trans. On Magn. Vol. 22. No. 5. p. 1017, Sep. 1986

[9] Bhatnagar, P.L., Gross, E.P. and Krook, M., "A model for collision processes in gases. I. Small amplitude processes in charged and neutral one-componetn systems," Physical Review, Vol. 94, No. 3, pp511-525, 1954

[10] Bird, G.A., "Molecular gas dynamics and the direct simulation of gas flows," Clarendon Press. Oxford, 1994

[11] Bo Liu, Gang Sheng, Wei Hua and Zhimin Yuan, "A dual stage slider-suspension design for nano-spacing recording," Report from Institute of High Performance Computing, 10 Kent Ridge Crescent, Singapore, 2001

[12] Brian H. Thornton and David B. Bogy, "Nonlinear aspects of air-bearing modeling and dynamic spacing modulation in sub-5-nm air bearings for hard disk drives," IEEE Transactions on Magnetics, Vol. 39, No. 2, March 2003

[13] Brunner, R.K., Harder, J.M., Haughton, K.E. and Osterlund. A.G., "A Gas Film Lubrication Study. Part III," IBM J. Res. Develop., Vol. 3. No. 3. p. 260, July 1959

[14] Burgdorfer, A. "The influence of the molecular mean free path on the performance of hydrodynamic gas lubricated bearings," ASME, J. Basic Eng., Vol. 81, pp94-100, 1959

[15] Busch-Vishniac, I.J., "Electromechanical Sensors and Actuators," Springer, New York, 1999

[16] Cercignani, C. and Daneri, A., "Flow of a rarefied gas between two parallel plates," Journal of Applied Physics, Vol. 34, No. 12, pp 3509-3513, 1963

[17] Cercignani, C., "Mathematical methods in kinetic theory," Second edition, Plenum Press, 1990

[18] Zhu, L. Y., "Measurement and Analysis of the Slider Disk Spacing in Magnetic Recording Disk Files." Ph. D. Dissertation, University of California, Berkeley, CA, 1989

[19] Miu, D. K., Bouchard, G.,Gogy, D.B., and Talke, F.E., "Dynamic Response of a Winchester-Type Slider Measured by Laser Doppler Interferometry." IEEE Trans. On Magn. Vol. 20. No. 5. p. 927, Sep 1984

[20] Berg, L. J. and Buettner, D.C., "Head/Disk Spacing Changes During Track Accessing in Magnetic Recording Hard-Disk Drives." Adv. Info. Storage Syst., Vol. 4. p. 169, 1992

[21] Shi, W-K., Zhu, L.Y., and Bogy, D.B., "Use of Readback Signal Modulation to Measure Head/Disk Spacing Variations in Magnetic Disk Files." IEEE Trans. On Magn., Vol,23, No. 1, p. 233, Jan 1987

[22] Klaas B. Klaassen, Jack C.L. van Peppen, "Head-Medium Clearance and Lateral Track Registration of a Recording Head as Measured from the Readback Signal," IEEE, Transactions on Magnetics, Vol. 37, No.1, January 2001

[23] Janmshid Bozorgi, Muhammad A. Hawwa, Wei Guo, and Yan Yan, "Performance Requirements of Microactuated Suspensions in Hard Disk Drives," Journal of Information Storage and Processing Systems, Vol. 2, pp293-302, 2002

[24] Kenji Suzuki, Ryutaro Maeda, Jiaru Chu, Takahisa kato, and Masayuki Kurita, "An Active Head Slider Using a Piezoelectric Cantilever for In-Situ Flying Height Control," IEEE, Trans, AP5-01 – AP502, 2002

[25] Liu B, Zhu Y L, Li Y H and Leng Q F, "Experimental study of slder-disk interface in nanometer spaced head-disk interface," Proc. Asian Symp. On Information Storage Technology, Singapore, Feb 1999

[26] Tanimoto K, Itoh J, Ohtsubo Y, Kubota Y and Sekimura M, "A study of beam type contact heads for HDDs," Adv. Info. Storage Syst., pp39-54, July 1997

[27] Lin, C., and Sullivan, R. F., "An Application of White Light Interferometry in Thin Film Measurements," IBM Journal of Research and Development, Vol. 16, No. 3, pp. 269-276., 1972

[28] Lieskovsky, V. M., "Optical Interference Thchniques for Spacing Measurements in 50 to 300 Microinch Range," Proc, MESUCORA 63 Congres International Paris, France, 1963

[29] Mitsuya, Y., and Kaneko, R., "Molecular Mean Free Path Effects in Gas-Lubricated Slider Bearings (2nd Report; Experimental Studies)," Bulletin of the JSME, Vol. 24, No. 287, pp. 301-308, 1981

[30] Mitsuya, Y., and Ohkubo, T., "High Knudsen Number Rarefaction Effects in Gas-Lubricated Slider Bearings for Computer Flying Heads," ASME Journal Of Tribology, Vol. 109, No. 2, pp. 276-282, 1987

[31] Ono, K., Kogure, K., and Mitsuya, Y., "Dynamic Characteristics for Air-Lubricated Slider Bearings under Submicron Spacing Condition," Bulletin of the JSME, Vol. 22, No 173, pp. 1672-1677, 1979

[32] E. Schreck, R. Kimball, and R.Sonnenfeld, "Magnetic read back microscopy applied to laser-texture characterization in standard desktop disk drives," IEEE Trans. Magn., Vol. 34, pp1777, 1998

[33] L. Chen, D.B. Bogy, and B. Strom, "Thermal dependence of MR signal on slider flying state: 3-D heat transfer model and comparison with experimental results," in INTERMAG 2000, Canada, April 9-13, 2000

[34] Fleicher, J. M., and Lin, C., "Infrared Laser Interferometer for Measuring Air-Bearing Separation," IBM Journal of Research and Development, Vol. 18, No. 6, pp. 529-533, 1974

[35] Nigam, A., "A visible Laser Interometer for Air Bearing Separation Measurement to Submicron Accuracy," ASME Journal of Lubrication Technology, Vol. 104, No. 1, pp. 60-65, 1982

[36] T.C. McMillan and F.E. Talke, "Ultra Low Flying Height Measurements Using Monochromatic and Phase Demodulated Laser Interferometry," IEEE Transactions on Magnetics, Vol. 30, No. 6, November 1994

[37] T. Ohkubo, J.Kishigami "Accurate Measurement of Gas-Lubricated Slider Bearing Separation Using Visible Laser Interferometry," Transactions of the ASME, Vol. 110, pp148-155, Jan1988

[38] Warwick Clegg, Xinqun Liu, Bo Liu, Amei Li, Chongtow Chong, and David Jenkins, "Normal Incidence Polarization Interferometry Flying Height Testing," IEEE Transactions on Magnetics, Vol. 37, No. 4, July, 2001

[39] Ohkubo, T., Kishigami, J., "Accurate Measurement of Gas-Lubricated Slider Bearing Separation Using Visible Laser Interferometry," Transactions of the ASME, Vol. 110, January, pp. 148-155, Jan 1988

[40] Ohkubo, T., Hayashi, T., and Mitsuya, Y., "Accurate Measurement and Evaluation of Dynamic Characteristics of Flying Head Slider for Large Capacity High-Access Performance Magnetic Disk Storage," Digest of Intermag'87 GB-08, 1987

[41] Hegde S., Scranton R., and Yarmchuk E., "Capacitance Measurement and Control of the Fly Height of a Recording Slider," U.S. Patent Office, #4931887, 1990

[42] Richard Sonnenfeld, "Fly Height, Pitch, and Crown Measurements of Hard-disk Sliders by Capacitance Stripe," IEEE Transactions on Magnetics, Vol. 28, No. 5, September 1992

[43] Richard Sonnenfeld, "Capacitance Methods in Head-Disk Interface Studies," IEEE, Transactions on Magnetics, Vol. 29, No. 1, January 1993

[44] R.J. Wallace, "Reproduction of magnetic recording signals," Bell Syst. Tech. J., pp1145-1173, Oct, 1971

[45] K. B. Klaassen and J.C.L. van Peppen, "Slider-disk clearance measurements in magnetic disk drives using the readback transducer," IEEE Trans. Instrum. Meas., Vol. 43, pp121-126, Apr. 1994

[46] K.B. Klaassen, R.E. Eaton, and J.C. L. Van Peppen, "Effect of thin-film disk texture on magnetic recording signals," J. April. Phys., pt. 2A, Vol. 73, No. 10, pp5554-5556, May 1993

[47] Cha, E., Chiang, C. and Lee, J.K., "Flying height change during seek operation for TPC sliders," IEEE Transactions on magnetics, Vol. 31, No. 6, pp2967-2969, 1995

[48] Chang, C.J., Schuler, C.A., Humphrey, J.A.C., and Greif, R., "Flow and heat transfer in the space between two corotating disks in an axisymmetric enclosure," Transactions of the ASME, Journal of Heat Transfer, Vol. 111, pp625-632, 1989

[49] Chen, C.S., Lee, S.M. and Sheu, J.D., "Numerical analysis of gas flow in microchannels, " Numerical Heat Transfer, Part A, Vol. 33, pp749-762, 1998

[50] Choi, D.H. and Yoon, S.J., "Static analysis of flying characteristics of the head slider by using an optimization technique," ASME Journal of Tribology, Vol. 116, pp90-94, 1994

[51] Churchill, S.W., Viscous flows, Butterworth Publishers, 1988

[52] Deng, Z.S., Mitsuya, Y. and Ohka, M., "Flying characteristics of head sliders when traveling over magnetic disk surfaces," Advanced in Information Storage Systems, Vol. 9, pp77-91, 1997

[53] Fukui S. and Kaneko R., "Analysis of ultra-thin gas film lubrication based on linearized Boltzmann equation: first report-derivation of a generalized lubrication equation including thermal creep flow," ASME Journal of Tribology, Vol. 110, pp253-262, 1988

[54] Fukui, S. and Kaneko, R., "Experimental investigation of externally pressurized bearings under high Knudsen number conditions," ASME Journal of Tribology, Vol. 110, pp144-147, 1988

[55] Harman, W. W., and Lytle, D. W., "Electrical and Mechanical Networks," Mcgraw-Hill, New York, 1962

[56] Ling, S. –F, and Xie, Y., "Monitoring structural integrity using a piezoelectric inertial actuator cum sensor," Journal of Sound and Vibration, Vol. 247, No. 4, 731-737, 2001

[57] Ling, S. –F., and Xie, Y., "Detecting mechanical impedance of structures using the sensing capability a piezoceramic inertial actuator," Sensors and Actuators A, Vol. 93, No. 3, 23-249, 2001

[58] Ling, S. –F, and Tang, Y. –J., "A new modal testing technique for miniature structures," Proceedings of the international modal analysis conference – IMAC-XIX, Kissimmee, USA, 1478-1482, 2001

[59] Ling, S. –F., and Xie, Y., "Mechanical impedance detection utilizing sensing capability of piezoceramic inertial actuator," Proceedings of the international modal analysis conference – IMAC, Vol. 2, 1901-1905, 2000

[60] Yanling Yin, S.-F. Ling, Yong Liu, A Dynamic Indentation method for characterizing soft incompressible viscoelastic materials, *Materials Science & Engineering A*, in press.

[61] Hou, X. "A new transducer for measuring mechanical impedance," Ph.D thesis, School of Mechanical & Aerospace Engineering, Nanyang Technological University, 2004

[62] O.J. Ruiz and D.B. Bogy, "A comparison of slider bearing simulations using different models," IEEE, Transactions on Magnetics, Vol. 24, No. 6, Nov, 1988

[63] Huebner Kenneth H., "The finite element method for engineers," New York: Wiley, 1982

[64] Paul W. Smith, Wilfred D. Iwan, "Dynamic Figures of Merit for the Design of gas-lubricated slider Bearings," Adv. Info. Storage Syst., Vol. 3, 1991, ISSN 1053-184X, ISBN 0-7918-0023-7, 1991

Appendix

Attempt to Design and Fabricate the New Slider

In Chapter 3-5, we have shown the in-situ flying height measurement capability of a conceptual slider, which consists of a cantilever and a patch of PZT. The PZT is mounting onto the surface of cantilever. Based on this novel concept, the design and realization of the slider will be introduced and discussed in this appendix. Inside this slider, a novel sensor consisting cantilever and PZT will be merged into slider. To realize this slider, MEMS technology is used. At the same time, the structure of the slider, the deposition of PZT, thermal analysis during fabrication, slider ABS design and results of in-situ flying height measurement will be introduced. Then the fabrication details and results will be shown. In our study, the ABS design is carried out by CML. The in-situ flying height measurement capability is studied by FE package which we have successfully developed and validated in Chapter 4 and 5.

A.1. Slider Design

A.1.1 Structure of Slider

Based on the previous study of the new sensor and related slider knowledge, the new slider would possess the in-situ flying height measurement capability. To realize this purpose, the slider should process the below features:

(1) A cantilever, together with a patch of PZT coated onto its surface is formed inside the slider.

(2) The cantilever is much thinner and more flexible than other parts of slider.

(3) The flying attitude of slider is mainly determined by the ABS on the slider body except cantilever and PZT.

(4) The ABS on cantilever has little influence on the flying attitude.

(5) The flying attitude of the slider body hardly changed when the cantilever deforms.

Regarding to these features, the structure of the slider is shown from Figure 1 to Figure 4. Figure 1 shows the schematic of structure of slider in three-dimensional view. From this figure, we see that the slider comprises 1) a primary passive air bearing slider that flies at about several or several tens nanometers spacing and establishes a stable platform on disk surfaces, 2) a cantilever together with a patch PZT coated onto its surface. Two vertical slots are used to define the cantilever. This cantilever together with PZT acts as a sensor for in-situ flying height measurement. PZT thin film is deposited on top of this cantilever. This cantilever can be called as an unimorph cantilever with PZT thin films.

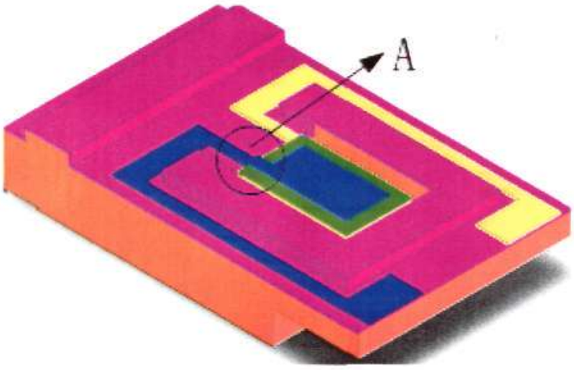

Fig. 1 3D view

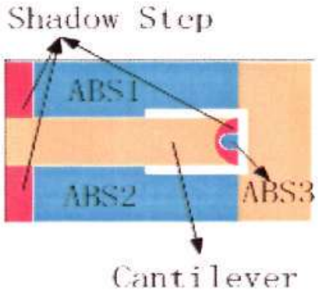

Fig. 2 Bottom view

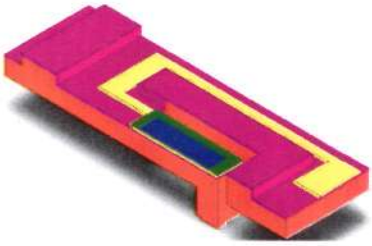

Fig. 3 Cross session view

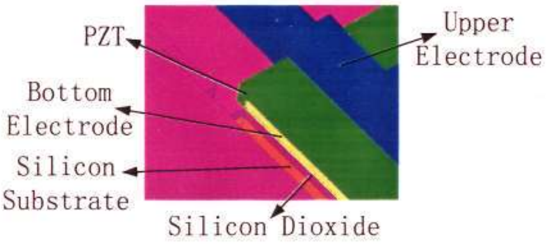

Fig. 4 Zoom-in view of part A

The dimension of the slider will be same as that of industrial standard pico slider, whose dimension is $1.25\times1.0\times0.3$ mm. In this small dimension, the MEMS technology is the most effective way to be used to fabricate the slider. The following part will introduce some key techniques and some related analysis during MEMS fabrication.

A.1.2 PZT Deposition

From description of above session, we know that the thin film of PZT is coated onto the surface of cantilever. In our fabrication, the commercial PZT (115/52/48) sol-gel solution is used for buildup the PZT thin film. This solution can be achieved from Mitsubishi Material Corporation. The concentration of the PZT solution is 15 wt%. %1 PT (120/100) solution is also used for depositing a seeding layer. Firstly, PT, as a seeding layer, is spin coated at 500 rpm for 3 seconds and 300 rpm for 15 seconds, and then pyrolyzed on the 350 ${}^{0}C$ hotplate for 1 minute. Subsequently, the PZT sol-gel solution is spin-coated on the silicon wafer at 500 rpm for 3 seconds and then 3000 rpm for 30 seconds. Then the film is given a pyrolysis heat treatment on the hotplate at about 300~400 ${}^{0}C$ for 5 minutes in air to remove the residual organics and promote chemical reaction. The process of PZT coating and pyrolysis is repeated 3~4 times, and then PZT film is annealed in the furnace in O_2 atmosphere at 700 ${}^{0}C$ for 15 minutes to make the thin film become crystallized. Usually each layer is deposited with a thickness 80 nm. The process of spin-pyrolysis-crystallization is repeated 1~5 times until the desired thickness of the PZT film is obtained. Figure 5 shows the whole process of PZT thin film.

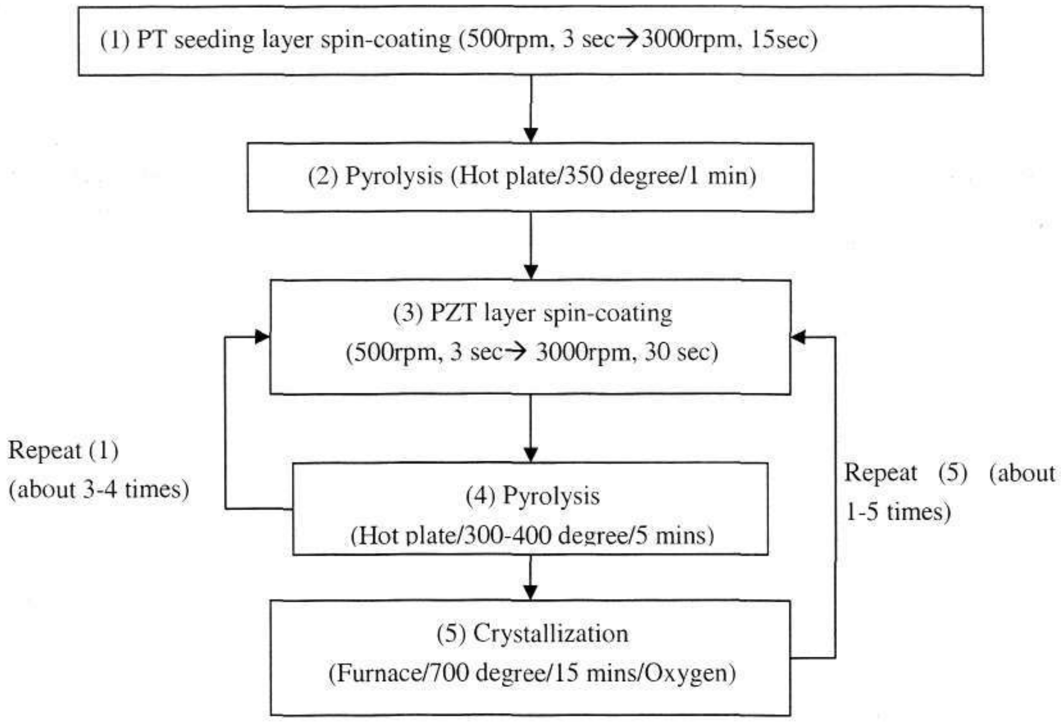

Fig. 5 Deposition of PZT thin film

After the PZT thin film has been deposited on the wafer, a photoresistive (AZ9260) layer will be coated onto the wafer and the pattern of PZT mask will be transferred to the surface of photoresistive. Subsequently, the wafers will be wet etched by the solution 40% HF/36% HCL/H_2O=1.5/10/30. This chemical solution etches PZT quite quickly without any etching of platinum. That means that the etching process will stop when the solution reaching the bottom platinum electrode. However, over-etching or under-etching will occur if the reaction is not monitored closely. The etching time depends on the concentration of the solution. In our process, 1 minute will be sufficient to etch away PZT. In this PZT deposition, the annealing temperature will reach 700^oC, this high temperature will cause high residual stress inside slider due to temperature effect. So we need carry out the thermal analysis, which will be introduced in the following session, to achieve a better design of slider.

A.1.3 Thermal Analysis during MEMS Fabrication

During deposition of PZT thin film, the annealing temperature will reach above 700^oC. This annealing process introduces residual stresses in PZT thin film due to thermal expansion mismatch. A high residual stress will cause the deformation of cantilever when it is cooled downed to room temperature. Residual stress that develops after processing is often referred to as extrinsic stress. The cause of such an extrinsic stress is a thermal expansion mismatch. If the thermal expansion coefficients of thin film and substrate are α_f and α_s respectively, then an incremental change in temperature ΔT would lead to a displacement mismatch of

$$\varepsilon_0 = (\alpha_s - \alpha_f)\Delta T \qquad (1)$$

per unit length of the two component if they are unbonded. Coherent bonding between the two components enforces continuity of displacements across the interface, and the atoms are constrained away from their equilibrium position. When the substrate is much less compliant than the thin film (either because it is much thicker or has a much higher modulus), the overall dimensions of the system are governed by the substrate, and the film dimensions are forced to match it. For example, if the thermal expansion mismatch and modulus are isotropic, so that biaxial stress conditions apply, the thermal residual stress is given by

$$\sigma_0 = E_f \varepsilon_0 (1 - v_f) \qquad (2)$$

where E_f and v_f are Young's modulus and Poisson' s ratio of the film, respectively.

In our research, the commercial Finite Element Package ANSYS was used to analyze the thermal stress problem. The main objective of this analysis is to understand the deformation of the cantilever after processing. For simplification, only the cantilever is considered in this thermal analysis. Figure 6 shows the sketch of the cantilever, together with PZT and electrode (Pt/Ti) deposited on its top surface one by one. Figure 7 shows the finite element model built in ANSYS and Figure 8 shows part A of finite element model. Table 1, 2 and 3 show the parameters of cantilever, thermal properties of materials and the parameters for different materials respectively. Under these conditions, Figure 9 shows the deformation of whole cantilever after fabrication. From this figure, we know that there is about 187 nm deformation on tip of cantilever toward the moving disk.

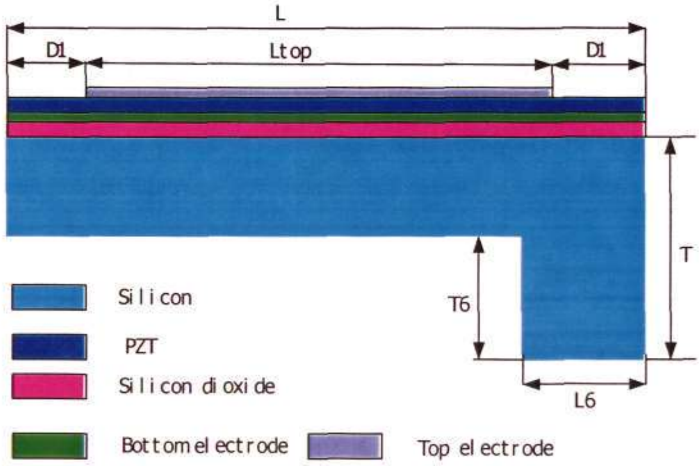

Fig. 6 Sketch of cantilever

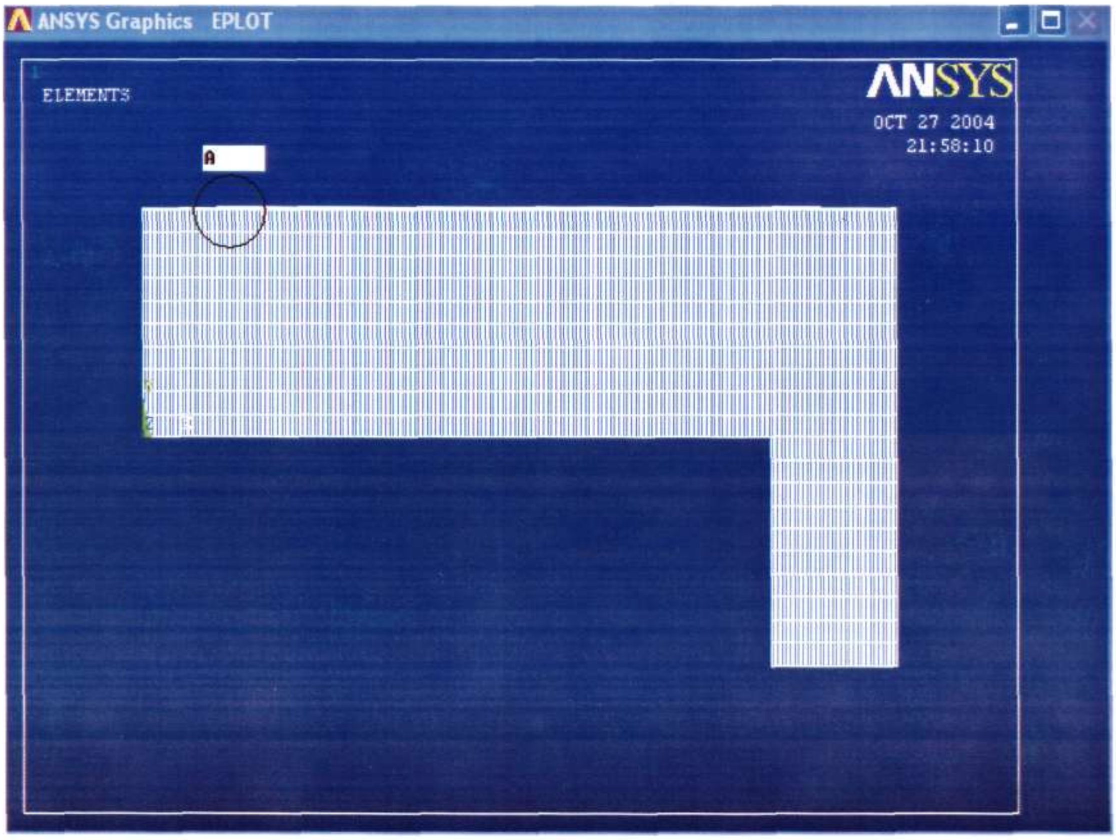

Fig. 7 Finite element model

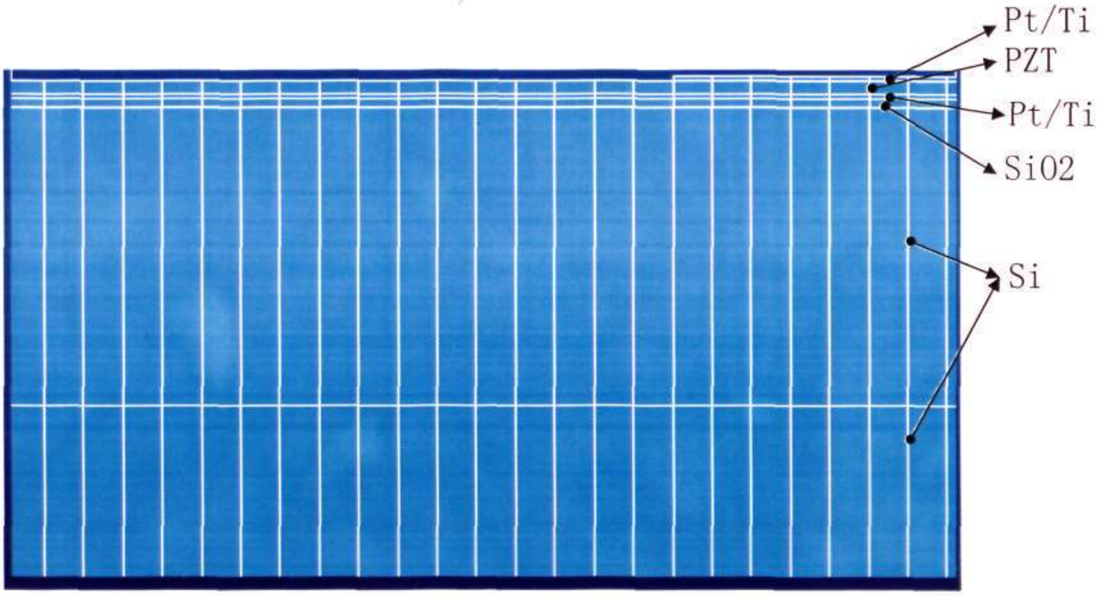

Fig. 8 Part A of finite element model

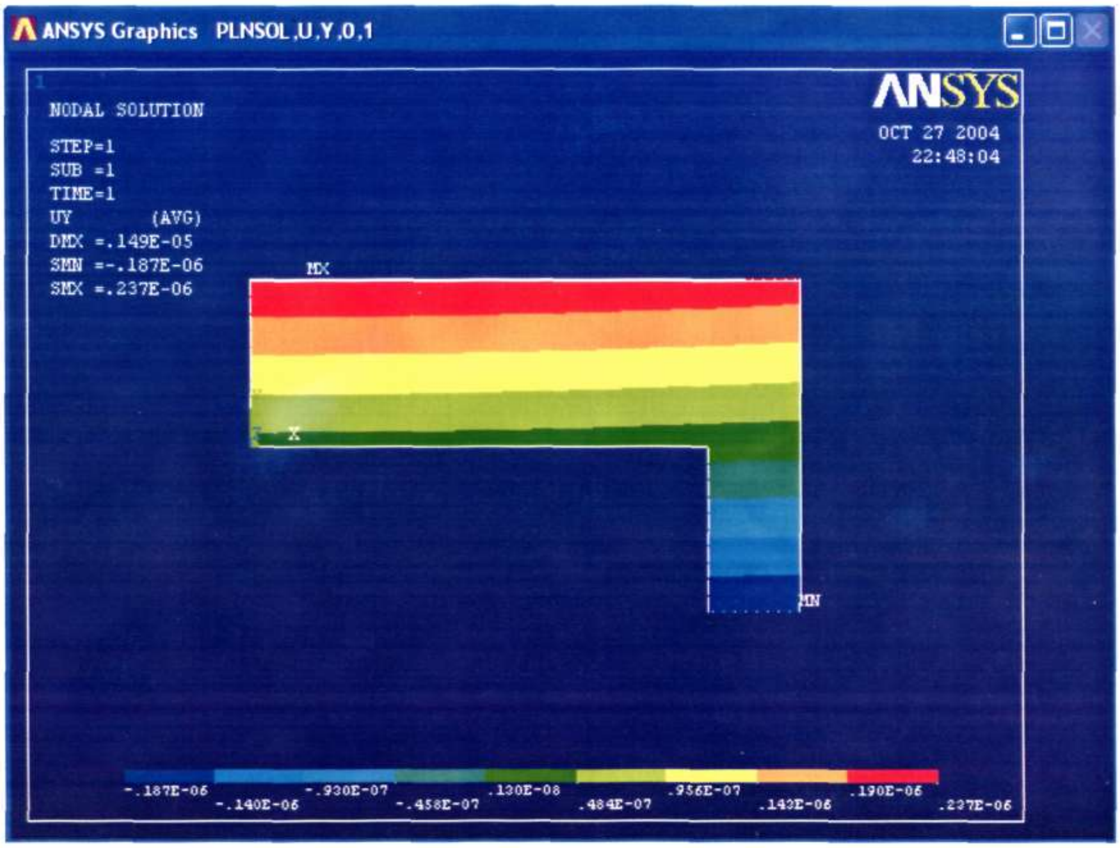

```
NODAL SOLUTION

STEP=1
SUB =1
TIME=1
UY          (AVG)
DMX =.149E-05
SMN =-.187E-06
SMX =.237E-06
```

```
OCT 27 2004
   22:48:04
```

Fig. 9 Deformation after fabrication

Table 1 Parameters for cantilever

Parameters	L	L6	Ltop	T	T6	D1=D2	Thickness		
Values (um)	500	100	400	300	150	50	SiO_2	Pt/Ti	PZT
							0.5	0.2	0.7

Table 2 Thermal properties of materials

Temperature (degree)	Thermal expansion coefficient, $\alpha(10^{-6})$			
	Silicon	SiO_2	Pt/Ti	PZT
20	2.616			1.8
200	3.614			
300	3.842			
350	3.929	0.4	8.9	6.2
400	4.016			7.8
500	4.151			8.2
600	4.205			8.2
700	4.241			8.2

Table 3 Young's modulus trend under different temperature and Poisson's ratio

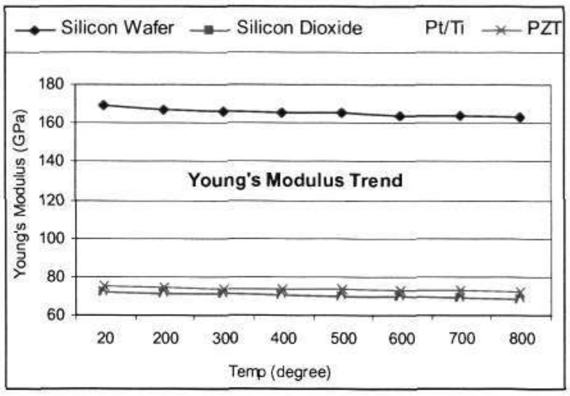

Properties	Young's modulus (Gpa)	Poisson's ratio v
Silicon wafer	169	0.279
Silicon dioxide	72	0.17
Pt/Ti	70	0.3
PZT	75	0.31

A.1.4 ABS Design and Results of Harmonic Analysis by FE Package

From the thermal analysis, we know that the central cantilever bends down toward to the disk even when the hard disk drive is not in work status. This bending deformation is fixed for a same MEMS fabrication process. On finishing the thermal analysis, air bearing surface (ABS) design using CML will be carried out to predict the stable flying height of slider. Firstly, we can calculate the preliminary flying height H_1 provided no deformation of cantilever due to air bearing force. And then the air bearing force f_{a1} will be achieved under flying height H_1. Here, f_{a1} is the resultant air bearing force acting on the cantilever. Such a force will cause the cantilever bend upward. The amount of bending of cantilever can be evaluated simply by the beam's theory. The flying attitude of slider will change due to this bending deflection. Correspondingly, the resultant air bearing force acting on the middle pad will vary. It is evident that the flying attitude of slider and bending of cantilever influence each other. Figure 10 shows the flying cantilever above moving disk. The ABS design will continue until $\Delta H = H_i - H_{i-1}$ is smaller than an acceptable value. For instance, if $\Delta H / H_i < m\%$ (m is a choice of an acceptable range, here we select it as 5), then we can say that the flying attitude is stable. The whole analysis flow is shown in Figure 11. And Figure 12 shows one of the ABS design. Table 4, 5 and 6 show the parameters of air, flying attitude and FH under different rotating speed, respectively. Figure 13 to 15 shows the air bearing pressure during different step of ABS design. Figure 17 shows the results of harmonic analysis using FE program, which is developed in Chapter 4 and Chapter5. It shows that, for this case slider design, the sensitivity can reach about 0.4613 ohm/nm. Table 7 shows parameters of other slider design of the slider. In our ABS design, there are three types: A, B and C. Figure 17 shows these three types of central ABS design. Table 8 shows the sensitivity for each design at a certain frequency.

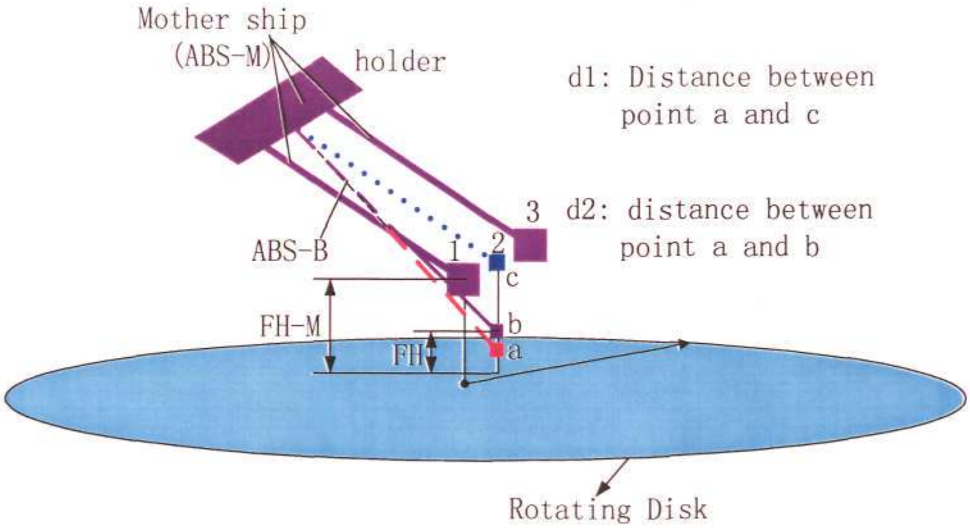

Fig. 10 Sketches of ABS and rotating disk

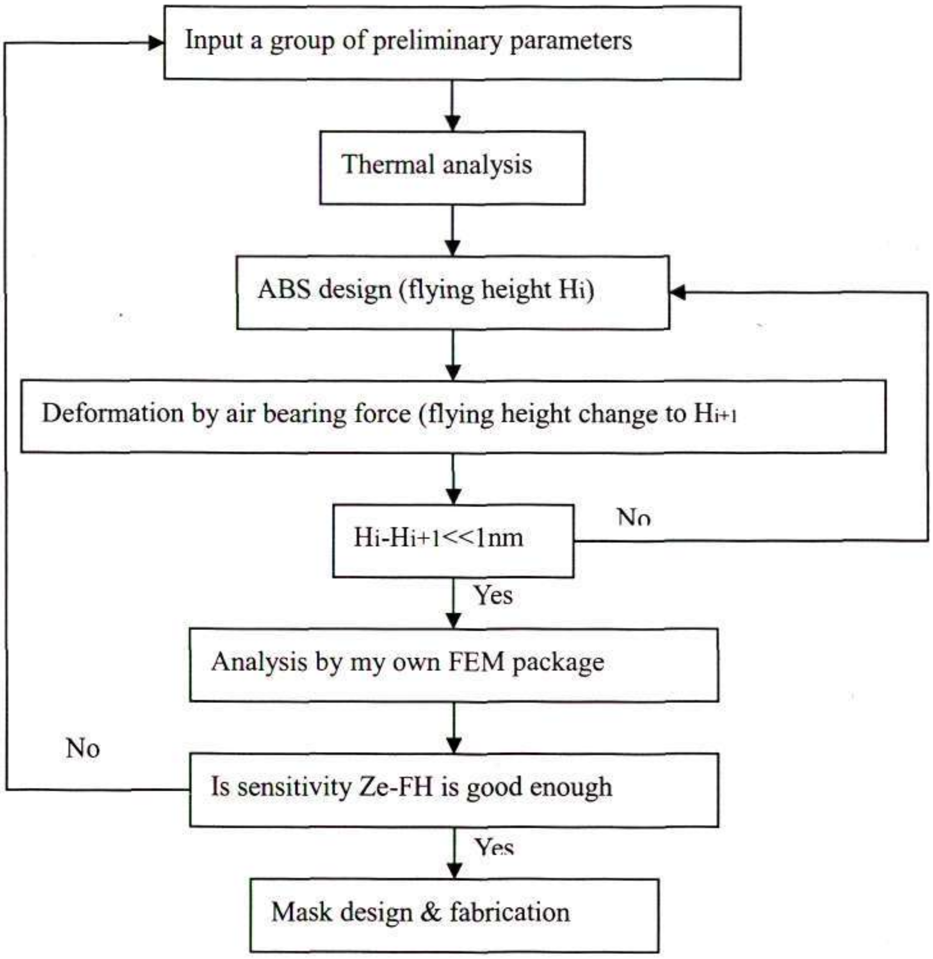

Fig. 11 Analysis flow of slider design with in-situ flying measurement capability

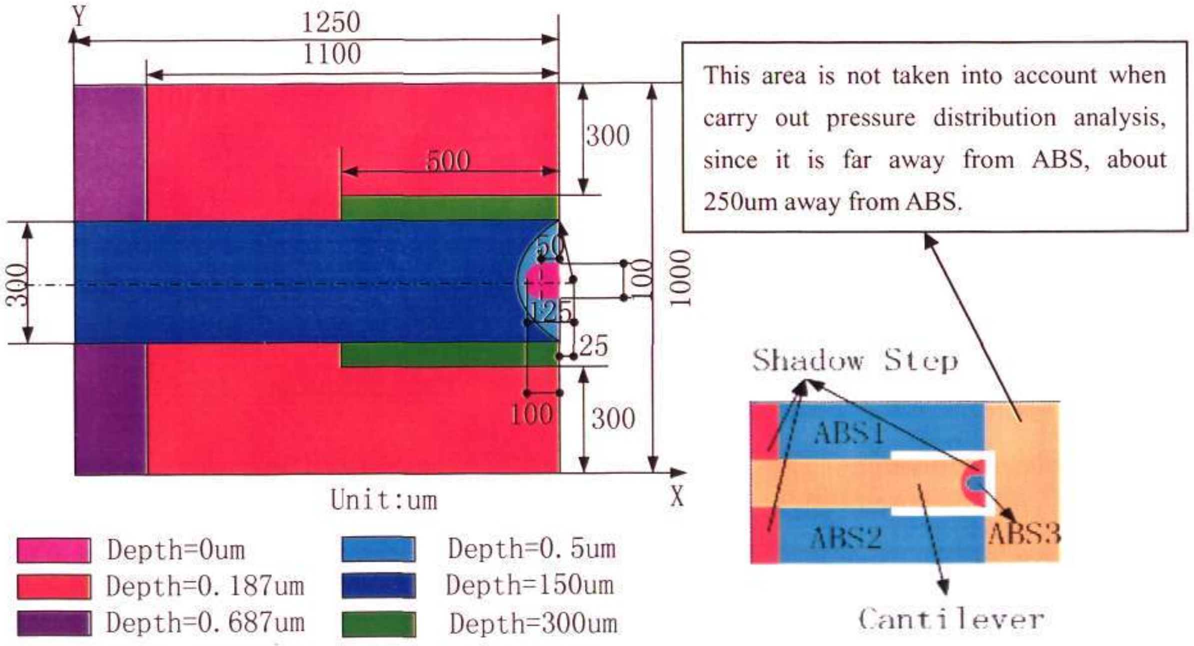

This area is not taken into account when carry out pressure distribution analysis, since it is far away from ABS, about 250um away from ABS.

Fig. 12 ABS design

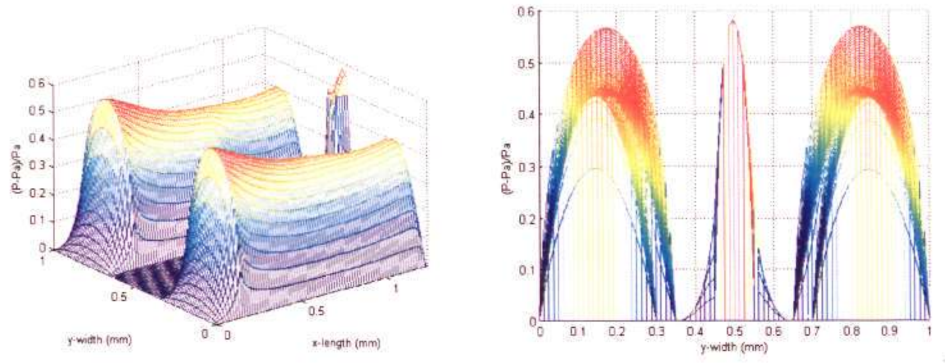

(a) XYZ-view of pressure distribution (b) YZ-view of pressure distribution

Fig. 13 Air pressure distribution of ABS for slider (1st analysis)

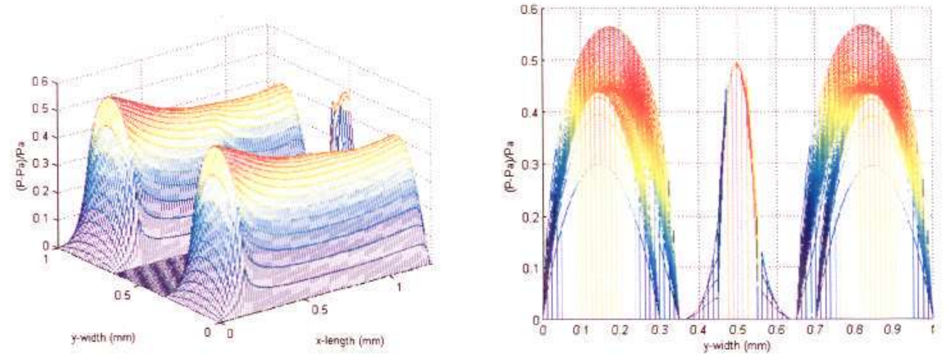

(a) XYZ-view of pressure distribution (b) YZ-view of pressure distribution

Fig. 14 Air pressure distribution of ABS for slider (2nd analysis)

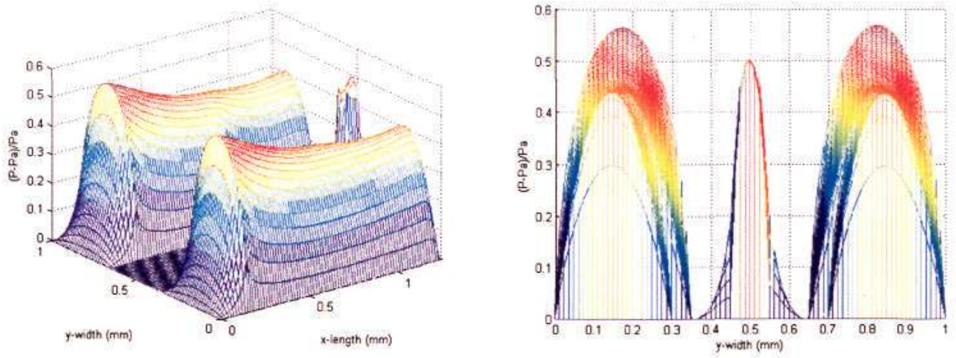

(a) XYZ-view of pressure distribution (b) YZ-view of pressure distribution

Fig. 15 Air pressure distribution of ABS for slider (3rd analysis)

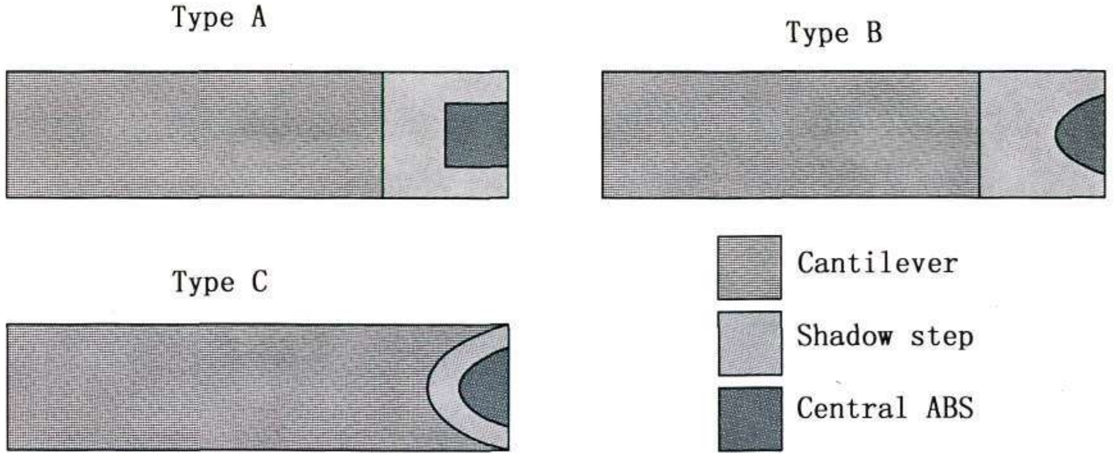

Fig. 16 Three types of central ABS designs

Table 4 Parameters for slider design

Parameters	Radius (mm)	RPM (s^{-1})	ATM (Pa)	Mean Free Path of Air (nm)	Viscosity of Air ($kg/(m \cdot s)$)	Suspension Force Acting on Slider (N)
Values	25.4	5400	1.01325×10^5	63.5	1.806×10^{-5}	2.5

Table 5 Flying attitude of slider (ABS area of cantilever $=3.0673\times10^{-8}m^2$)

Step	1st	2nd	3rd
FH (nm)	88.0057	106.253	104.325
FH-M (nm)	279.31	278.535	278.61
Pitch (uRad)	156.894	158.481	158.32
Roll (uRad)	-7.82574	-7.78583	-7.79087
Average Pressure (atm)	0.4103	0.3614	0.3731
Deflection (nm)	19	17	18

Table 6 FH under different rotating speed

RPM	3600	4500	5400	7200	9000
FH (nm)	37.6733	73.828	104.325	163.337	213.025

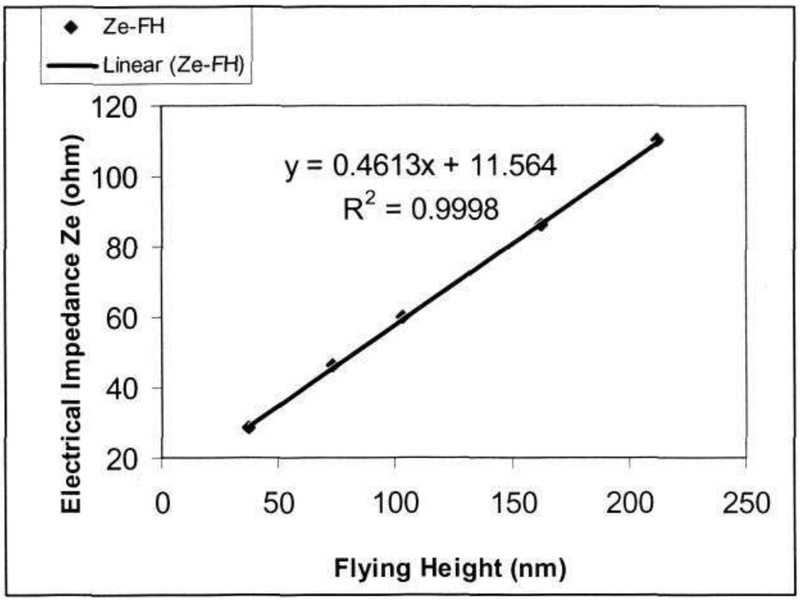

Fig. 17 Ze-FH (Freq. = 232 kHz, k=0.4613 ohm/nm)

Table 7 Parameters for cantilever (Unit: um)

	Central ABS Type	L	L6	Ltop	T	T6	D1=D2	Thickness		
								SiO_2	Pt/Ti	PZT
Slider 1	A	500	100	400	300	150	50	0.5	0.2	0.7
Slider 2	B	500	100	450	300	200	25	0.5	0.2	0.7
Slider 3	C	500	100	500	300	250	0	0.5	0.2	0.7
Slider 4	A	600	100	300	300	150	150	0.5	0.2	0.7
Slider 5	B	600	100	450	300	200	125	0.5	0.2	0.7
Slider 6	C	600	100	600	300	250	0	0.5	0.2	0.7
Slider 7	A	650	100	400	300	150	125	0.5	0.2	0.7
Slider 8	B	650	100	500	300	200	75	0.5	0.2	0.7
Slider 9	C	650	100	650	300	250	0	0.5	0.2	0.7
Slider 10	A	700	100	500	300	150	100	0.5	0.2	0.7
Slider 11	B	700	100	600	300	200	50	0.5	0.2	0.7
Slider 12	C	700	100	700	300	250	0	0.5	0.2	0.7

A.2. Realization of Slider

In the above section, the structure design, ABS design and in-situ flying height measurement capability of a novel slider have been discussed in detailed. All these designs were carried out by CML code, ANSYS and our FE package. To verify the in-situ flying height measurement capability, we need to realize the slider and use the experimental results to be compared with the simulation results. In current industry, a slider is fabricated by a mature process. For our new slider design, it would be fabricated by MEMS technology. In this section, the fabrication details and mask set design are given firstly. Then, the fabrication results, possible factors to affect the fabrication and recommendations are discussed.

A.2.1 Fabrication Details

The fabrication of MEMS-based slider includes eight main steps:

1) The thin walls are formed by a deep reaction ion etching (DRIE) method.
2) The bottom electrode is deposited by sputtering and patterned by a lift-off process.
3) A PZT thin film is deposited by sol-gel spin coating with commercial Mitsubishi E-Series solution and patterned by wet etching.
4) The upper electrode is deposited and patterned by the same method as that was used on the bottom electrode.
5) A layer of silicon dioxide is deposited on top of slider.
6) The shadow step of ABS is formed by DRIE.
7) The cantilever and slider are released from its front side by DRIE process.
8) The cantilever and slider are released by DRIE from back side by DRIE process.

The fabrication process is listed in Table 8 and series of 3-dimensional, top/bottom and cross-session A-A view are shown in Table 9. All the fabrication steps will be performed in Micro Machines Center of Scholl of Mechanical and Aerospace Engineering in Nanyang Technological University of Singapore.

Table 8 Main fabrication process flow of MEMS-based slider

Sequence No.	Fabrication	Thickness (*um*)	Deposition Method	Etching Method
1	Wafer cleaning			
2	Forming thin walls	5		DRIE
3	S_iO_2 deposition	0.5	Thermal oxide	
4	Bottom electrode	Ti (0.05)/ Pt (0.15)	Sputtering	Lift-off
5	PZT	0.7	Sol-gel	PZT etching solution
6	Upper electrode	Ti (0.05)/ Pt (0.15)	Sputtering	Lift-off
7	S_iO_2 deposition	0.5		
8	Back side S_iO_2 etching	0.5		Wet etching
9	Shadow step of ABS etching	0.5		DRIE
10	Front side S_iO_2 etching	1(=0.5+0.5)		Wet etching
11	Front side bulk Si etching	145(=150-5)		DRIE
12	Back side bulk Si etching	150(=300-150)		DRIE

Table 9 Development for slider (shown continuously in following two pages)

Step	3-D View	Top/Bottom View	Cross A-A View
1		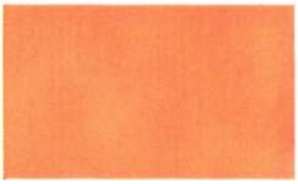	
2		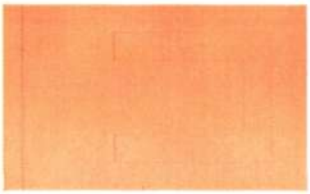	
3	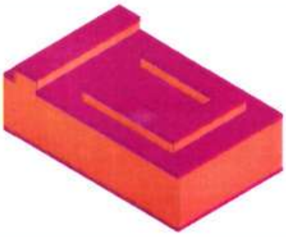		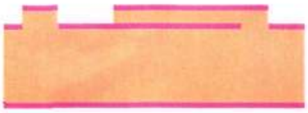

4		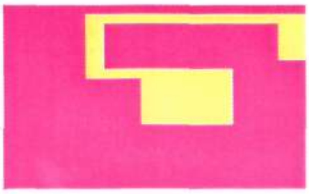	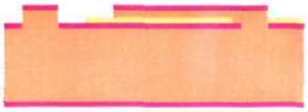
5	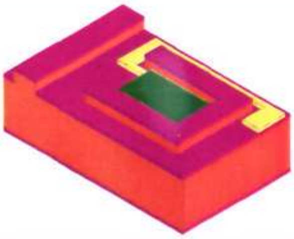	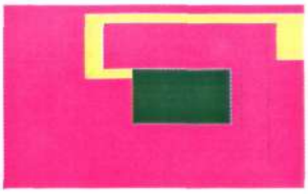	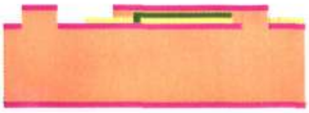
6	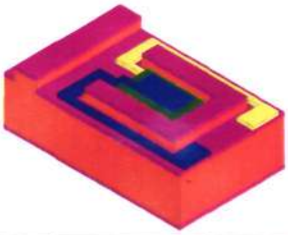	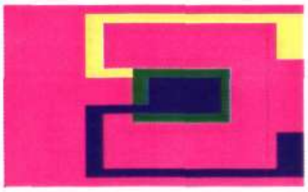	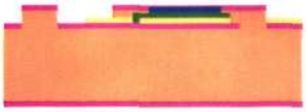
7	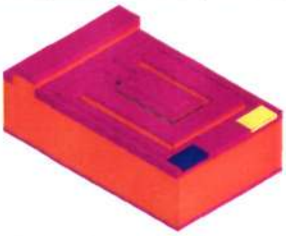		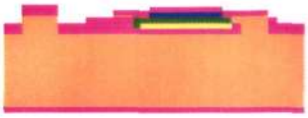
8	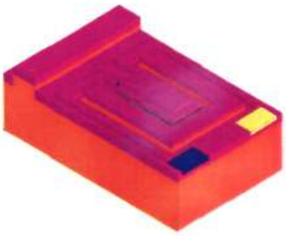		
9	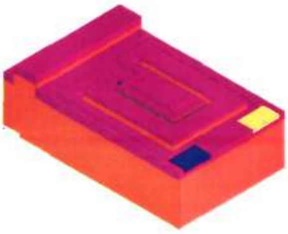	 (bottom view)	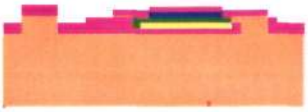
10	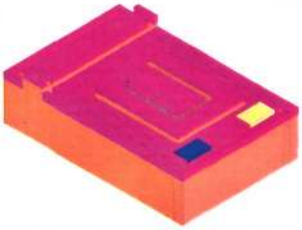		

11	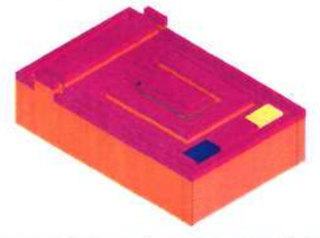	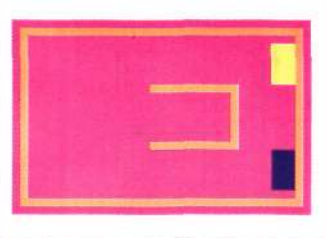	
12	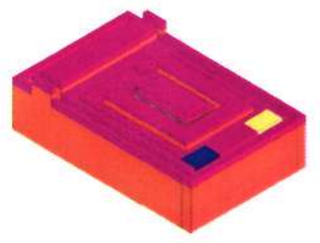	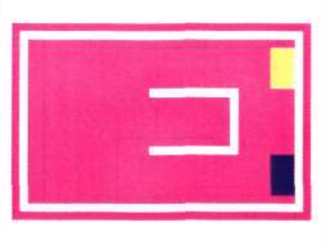	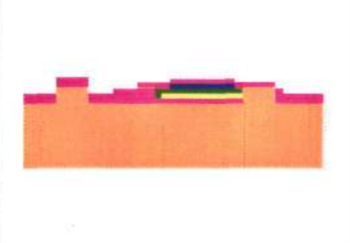

🟧 Silicon 🟪 Silicon Dioxide 🟩 PZT

🟦 Upper Electrode 🟨 Bottom Electrode 🟥 ABS

A.2.2 Mask Set Design

From the above discussions, it shows that there should be 8 masks for the fabrication of MEMS-based slider. Figure 18 shows the wafer layout for the whole mask design. Figure 19 shows part of the whole wafer. In this figure, it also shows the individual cell device and the alignment mark for the wafer. The alignment mark is very important for the fabrication as it will offer us the convenience to make the different layers into same coordinates. Table 10 shows one of the individual layers and related information. Black or Transparent inside table means the part corresponding to that shown in figure is kept or etched away. Eight layers are used in this MEMS-base slider fabrication. The mask design is carried out in Micro-Machine Centre (MMC) of Nanyang Technological University. And they are designed by commercial software LEdit 10.2, which is one of the best software for mask design. The MEMS fabrication will be also carried out in MMC. Twelve different types of sliders (shown in Table 7) are fabricated at the same time. Fabrication results will be shown in next section.

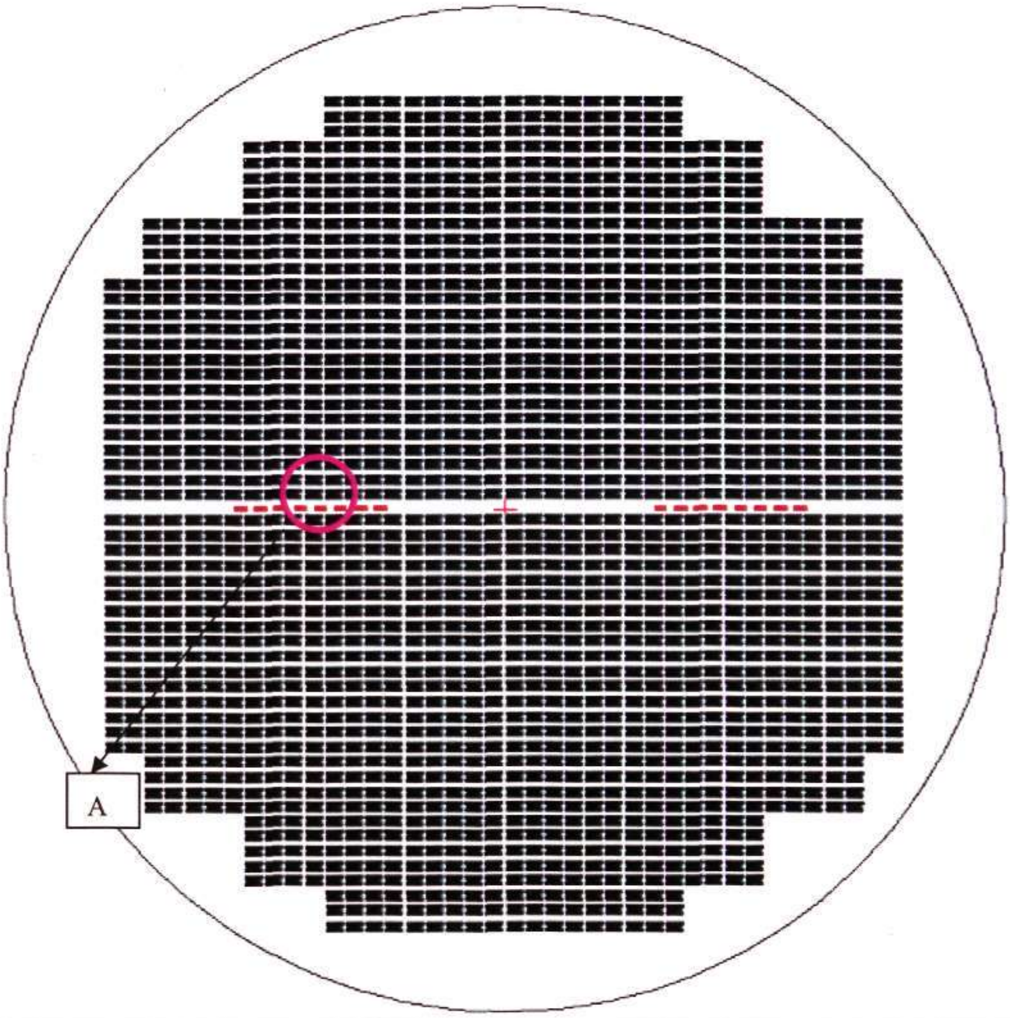

Fig. 18 Wafer layout

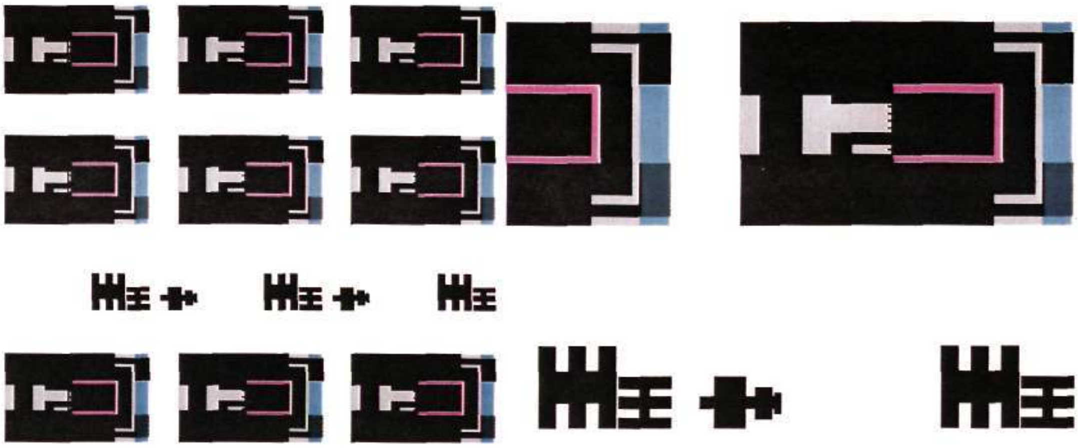

Fig. 19 Part A of wafer layout

Table 10 Mask set design (shown continuously in following one page)

Mask & Color	Cell	Construction
1 Dark	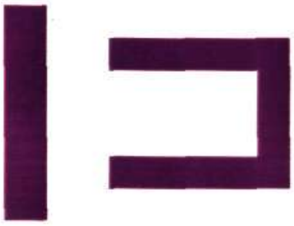	
2 Transparent		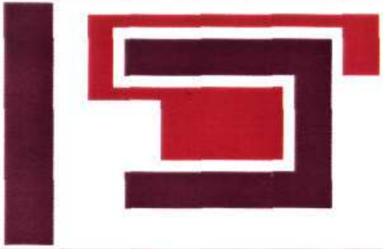
3 Dark	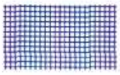	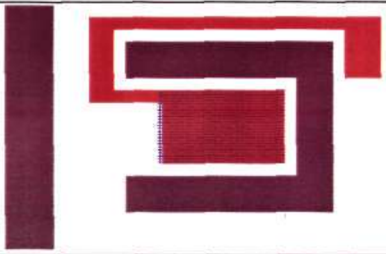
4 Transparent		

5 Transparent	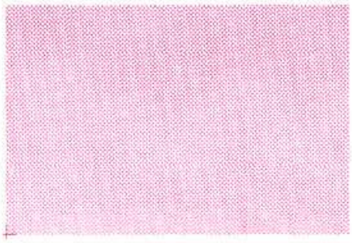	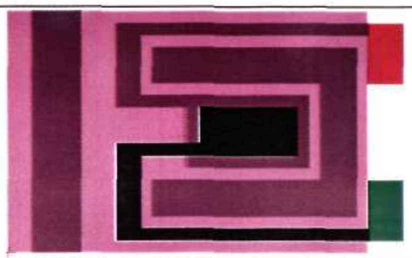
6 Transparent	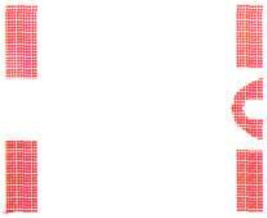	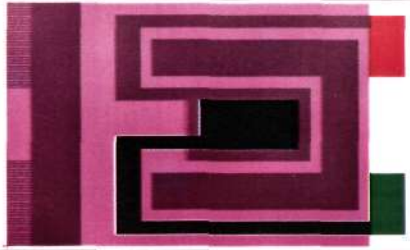
7 Transparent	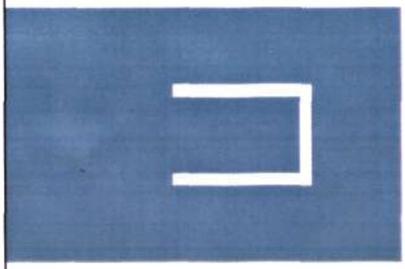	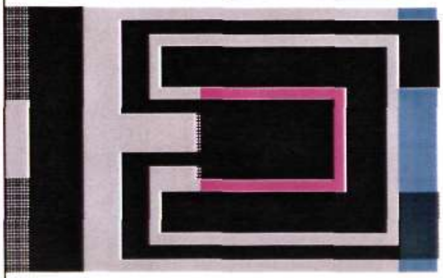
8 Dark	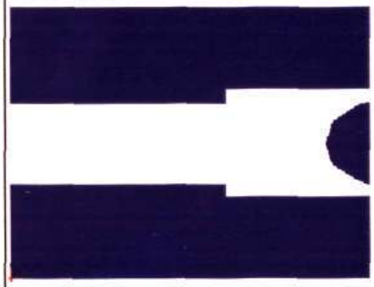	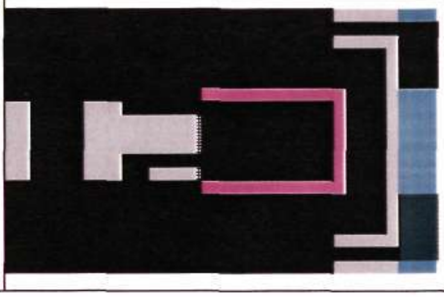

A.2.3 Fabrication Results

Following the fabrication steps which are shown in the previous section, the novel slider has been fabricated. The fabrication results for some individual step are shown. Figure 20 shows several sliders that PZT has been deposited on the part of cantilever. Figure 21 shows the zoom-in view of Figure 20 (a). The layer of PZT is not very clean and uniform as shown in these figures. The possible reasons for these defects are: 1) contamination inside the clean room, 2) photoresistive is not deposited smoothly and uniformly, 3) particle or air bubble keeps inside PZT after thermal processing. Figure 22 shows the results after top electrodes have been sputtered onto the PZT layer. Figure 23 shows the zoom-in view. From these figures, it can be seen obviously that the deposition of top electrodes is worse than that of bottom electrodes. Top electrode is rough and uneven compared with bottom electrode. This ununiformity comes from: 1) the adhesion between Pt/Ti and PZT is much lower than that between Pt/Ti and silicon dioxide, 2) the uniformity of PZT is much worse than that of silicon dioxide. To improve the deposition of top electrodes, the PZT deposition must be improved firstly to keep a uniform surface of PZT. Figure 24 shows the fabrication results after the silicon dioxide has been deposited onto the surface of whole wafer. Silicon dioxide is deposited here for separating the electrodes from contacting suspension after assembling slider into head gimbal assembly (HGA). Figure 25 shows the air bearing surface for several designs. It can be seen that the ABS is not uniform and rough. At the same time, on the ABS, there is lots of contamination and chip off at the edge. For an industry slider, contamination existing on ABS surface would not be acceptable due to flying height of slider is very low and contamination will cause slider contacting with disk, which will make both slider and disk be damaged. So in industry, the slider will be fabricated in a high class (class 100) clean room. As in NTU, the class of clean room is only class 1000, which is not clean enough for slider fabrication. This is the root cause of our failure to fabricate an acceptable slider in PhD limited time. Figure 26 shows that a layer of photoresistive has been deposited onto the ABS surface before the wafer is released from back. Figure 27 shows the fabrication results before the wafer will be etched from back side.

Figure 28 shows the results of after releasing slider from front side for 10 mins. When released the slider from front side of wafer, the etch rate of silicon, gas type and etching time etc are all very important for a good result. There are twelve wafers at the beginning of our fabrication, and only 2 pieces of wafers are left with acceptable results. During the last step, release slider from front side of wafer, we observed the results after 10 minutes' etching, even the designed etching time is 30 minutes for etching away about 150 um silicon. From these figures, it can be seen that: 1) the surface becomes dark, 2) surface becomes very uneven. The results are not acceptable. Firstly, the dark surface is the results of high temperature heating and over-etching of the photoresistive. And we can say that the protecting layer of photoresistive is not thick enough to prevent silicon from direct contacting with etched gas. Secondly, the etchants inside DRIE machine did not etch the surface evenly. To improve the etching results, the etchants and a very good recipe for DRIE machine are required.

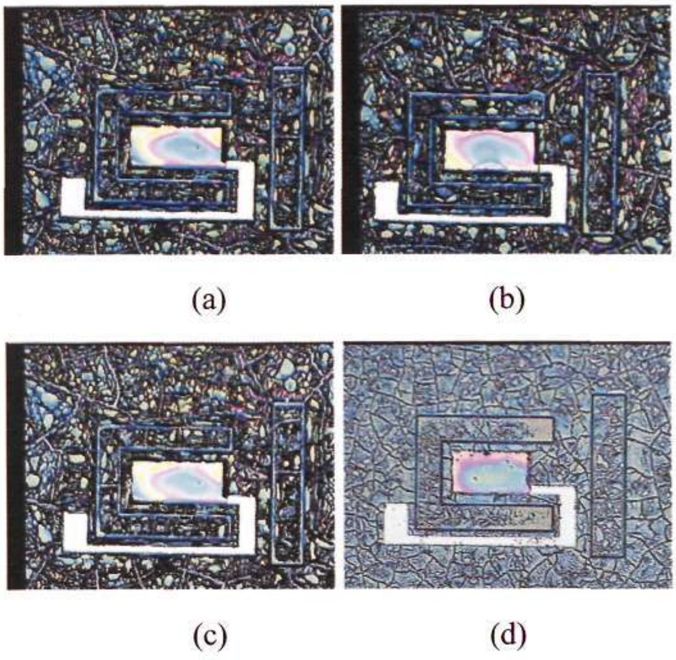
(a) (b)

(c) (d)

Fig. 20 PZT deposited on cantilever

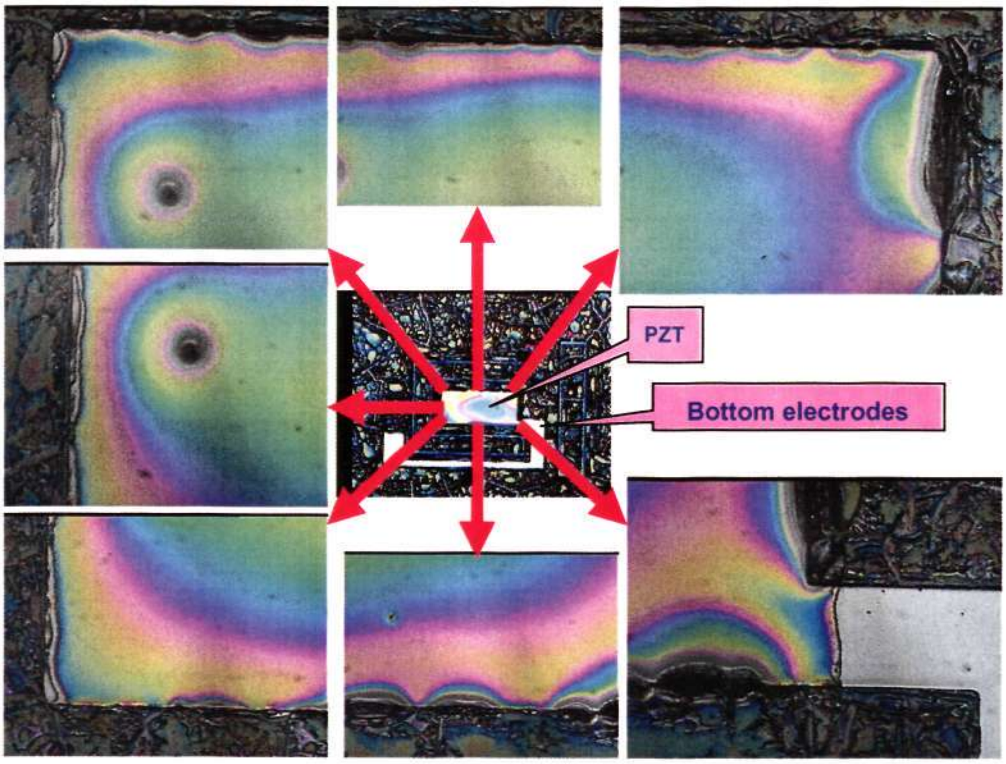

Fig. 21 Zoom-in view of Fig. 20 (a)

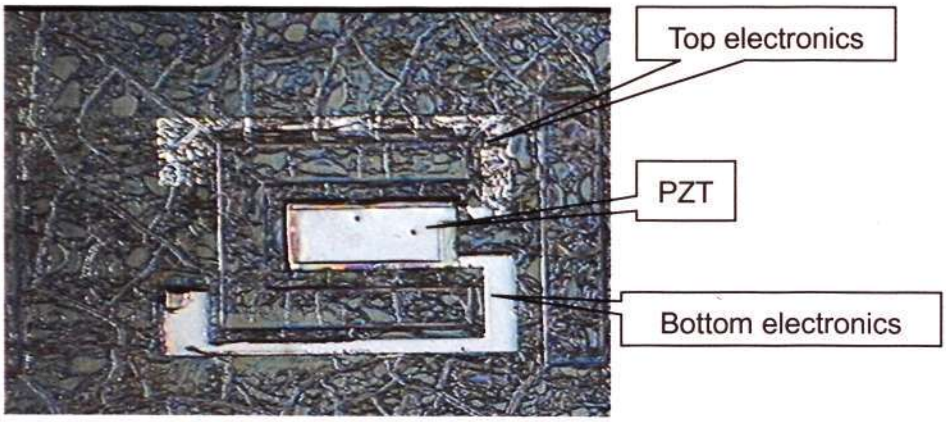

(a)

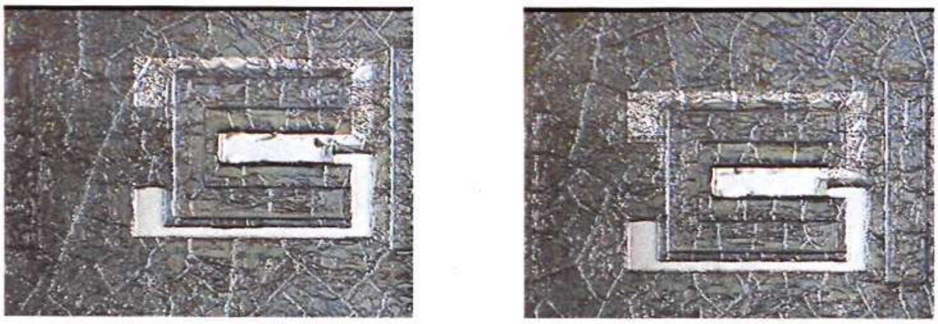

(b) (c)

Fig. 22 Top electrodes (Pt/Ti) deposition

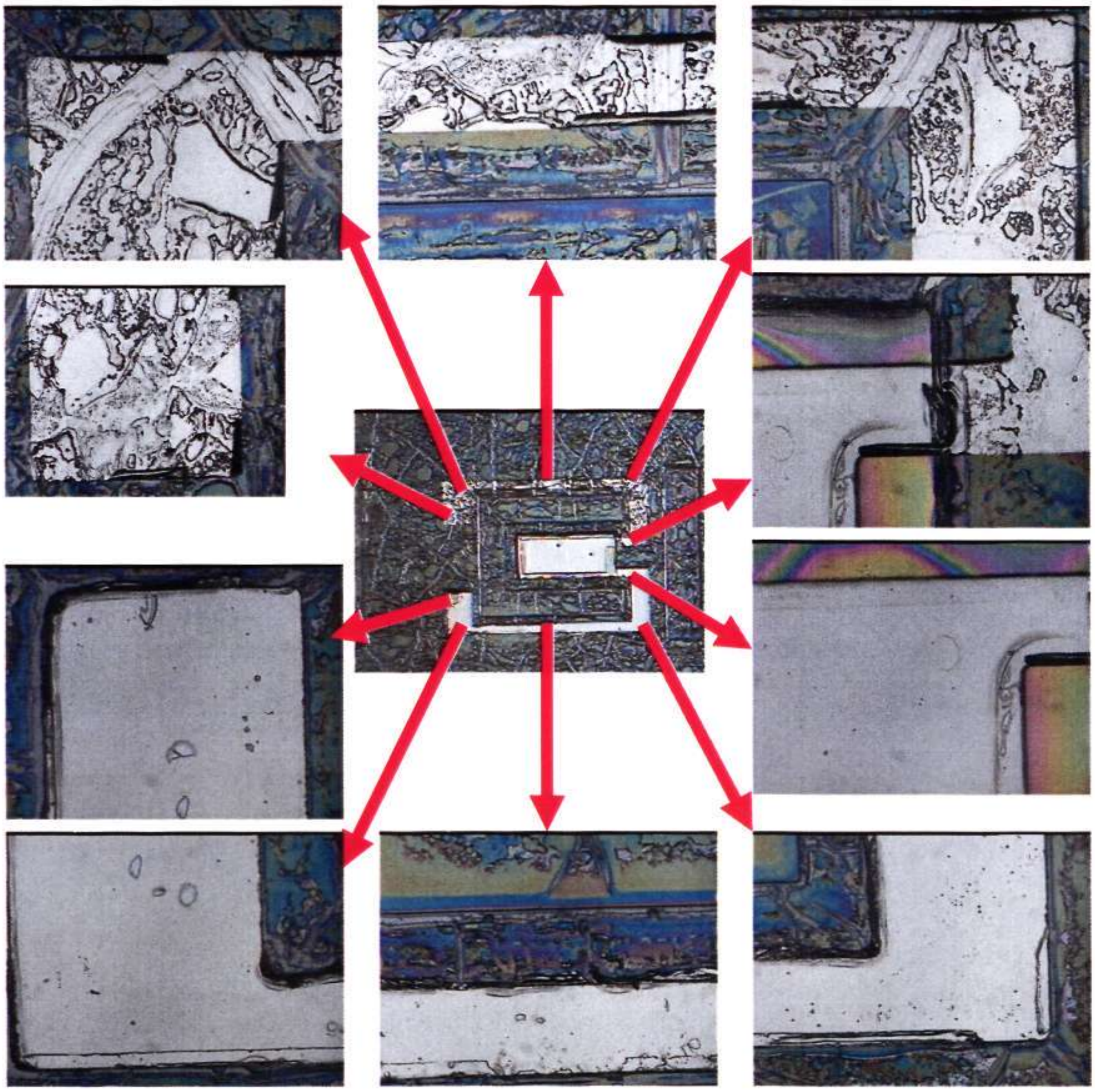

Fig. 23 Zoom-in view of Fig. 22 (a)

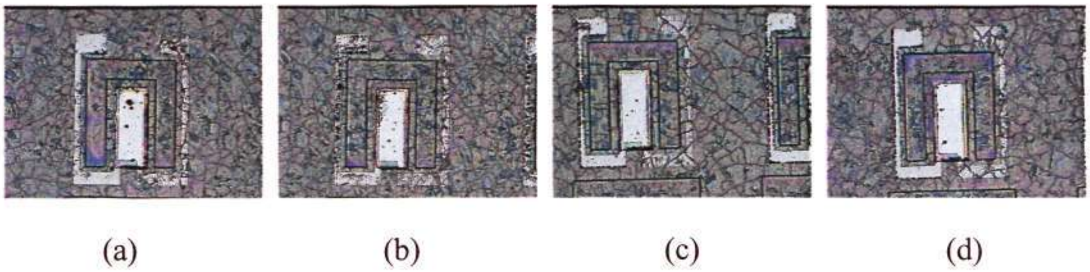

(a) (b) (c) (d)

Fig. 24 Top silicon dioxide deposition

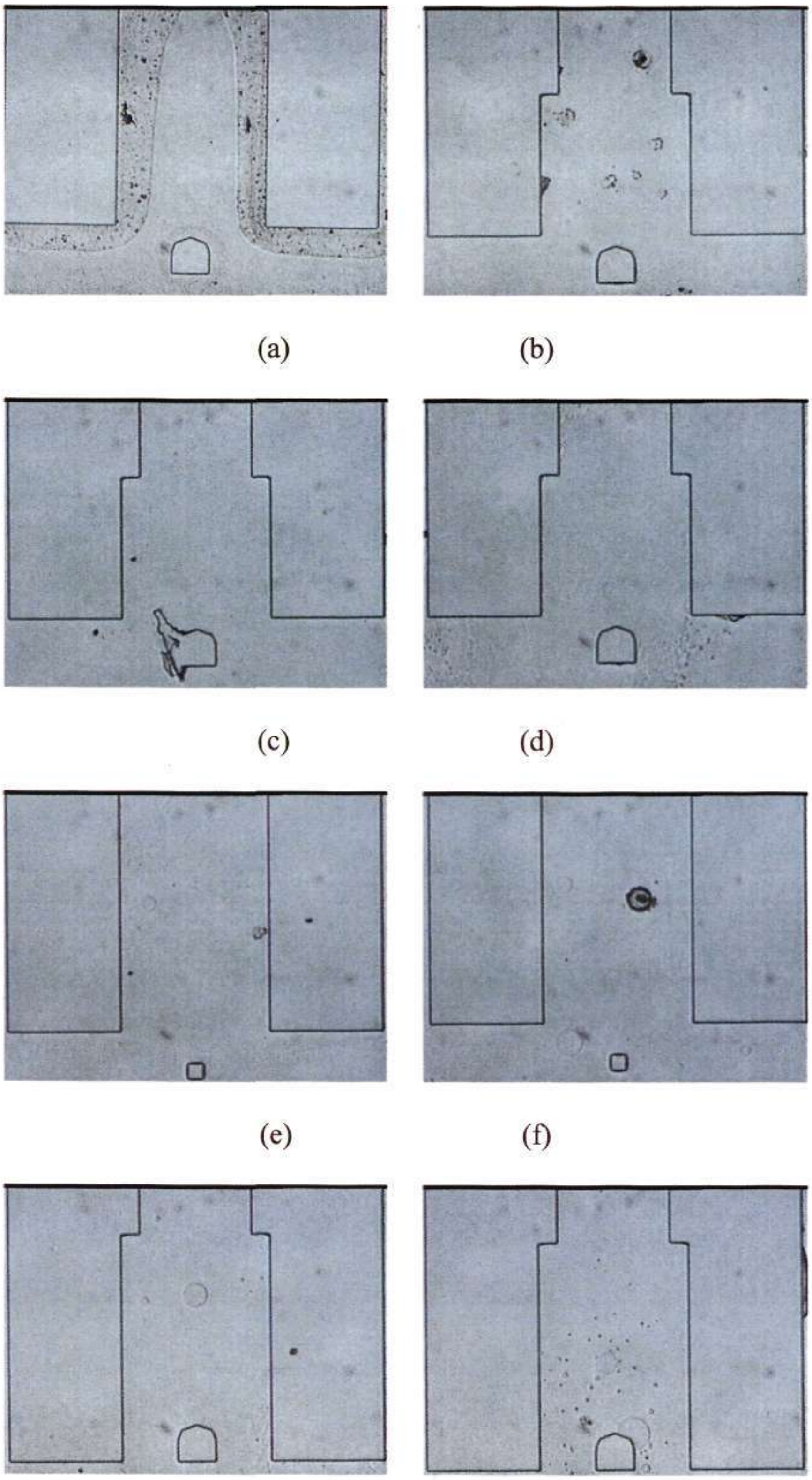

(a) (b)

(c) (d)

(e) (f)

(g) (h)

Fig. 25 Air bearing surface

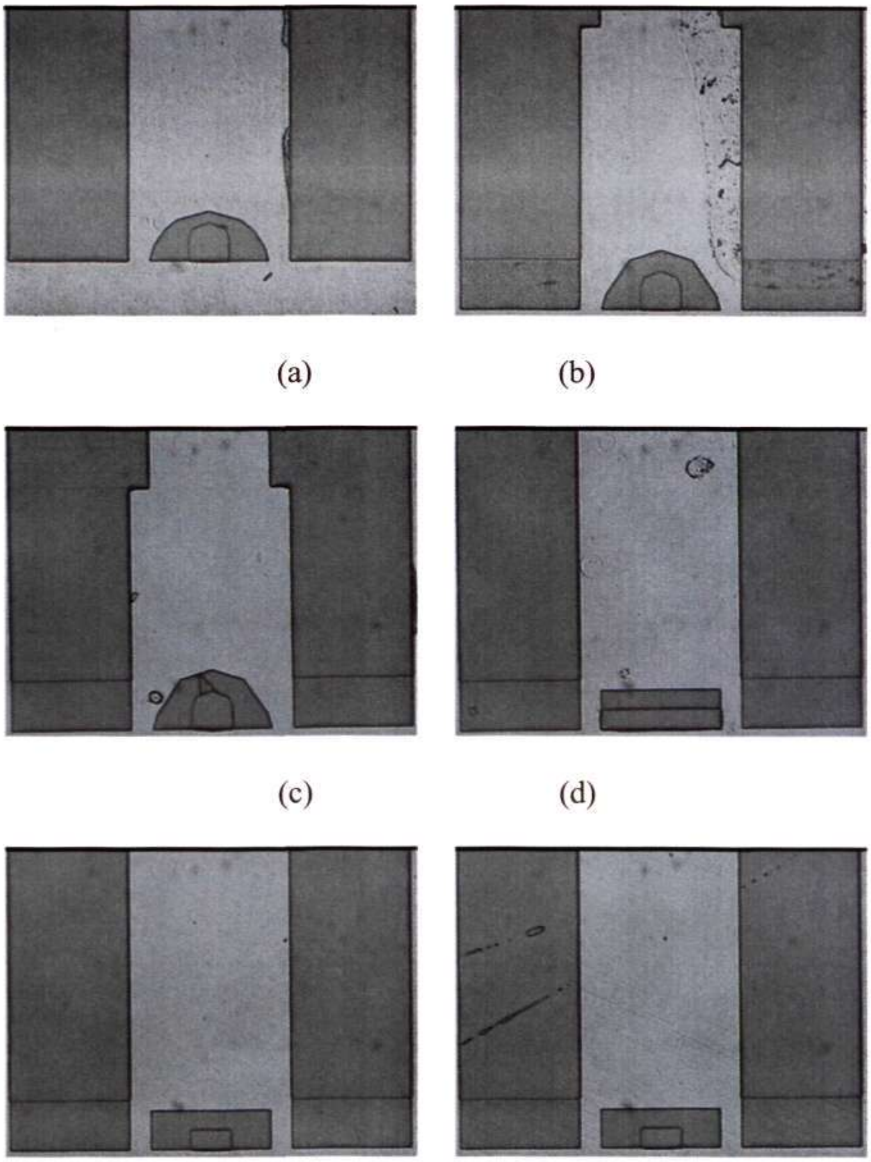

(a) (b)

(c) (d)

(e) (f)

Fig. 26 Photoresistive deposited onto ABS
(before releasing slider from back side of wafer)

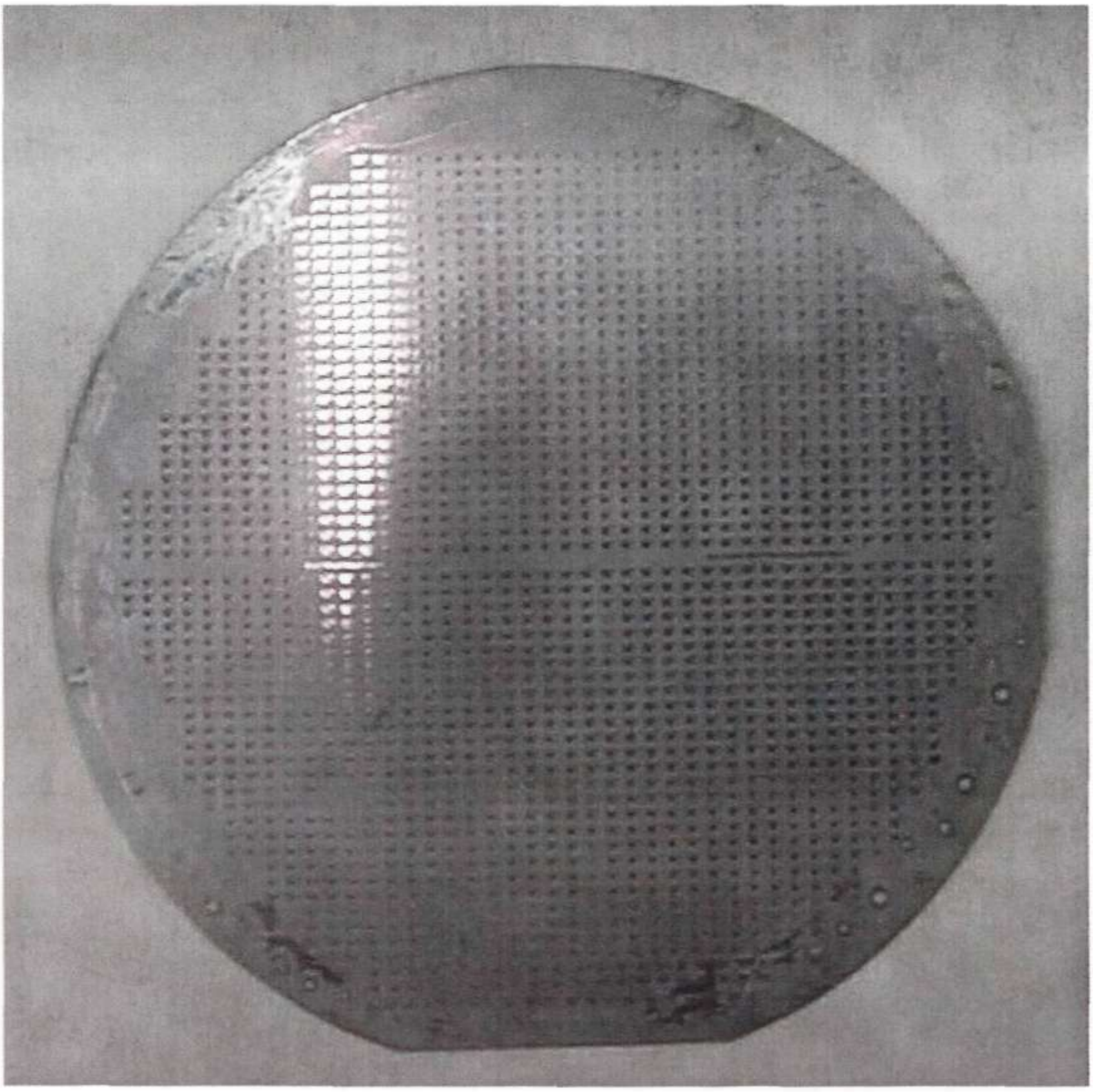

Fig. 27 Fabrication results before etching from back side of wafer

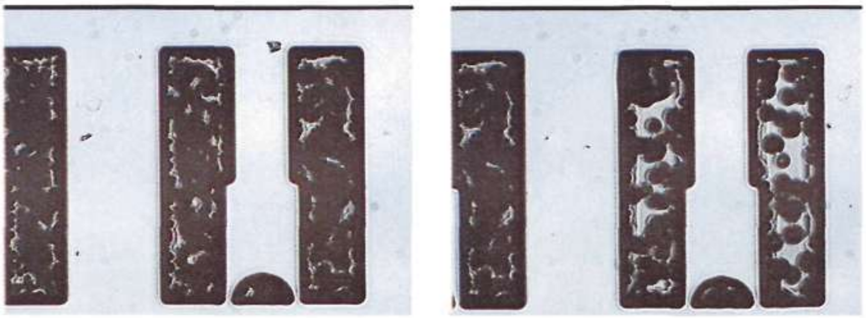

(a) (b)

Fig. 28 Results after 10 minutes' etching

A.3. Discussions and Recommendations

In the above several sections, the slider fabrication results have been shown and the possible causes of failing to fabricate it have also been discussed. The cause could be concluded as below:

1. The clean room is only Class 1000, which is not clean enough for slider fabrication. Class 100 is a must for the clean room for fabricating a slider.
2. Lots of particles and contaminations exist inside clean room. They are landing on the surface of wafer, or penetrating into the photoresistive, or reacting with the gas during fabricating slider. All these defects make some layers of slider be contaminated. For example, there are ununiformities, chip off and debris on the top surface of PZT due to insufficiently clean air and lots of particle.
3. The recipe of some MEMS fabrication machine has limited capability. For example, when the slider is released front side of wafer, as the etchants inside etching machine can not be evenly distributed, and the temperature distribution is also not even, so the etching rate is not same along the whole surface of wafer, but the protect layer for etching silicon is same, this difference causes that protect layer of some part of wafer has been etched away, but other part are still left on wafer surface. In our fabrication, middle part of wafer has a higher etch rate than that of other part.
4. Limited samples at the etching stage can be used to study the exact etching time required to forming the shallow step and ABS. This maybe the first try of

fabricating a slider by MEMS technique, so, the etching time for forming ABS is not confirmed. Theoretically, one may obtain a rough required etching time by using different etching conditions and measuring the fabrication results. For the ABS fabrication with high resolution of sub-micro, we need an exact etching time to etch the shallow step and ABS etc. One could achieve this exact etching time after many etching trials. But as limited samples we have at my last PhD stage, we could not have enough trials and could not get an exact etching time for forming the ABS.

5. Do not successfully examine the fabrication results after each step. There are a lot of sub-steps during the MEMS fabrication. Every result after a single MEMS fabrication step plays important role for the whole process. For example, if we need to deposit the electronic pole, we have better give a detailed check on the sample after it is cleaned in the water tank before deposition of Pt/Ti. A left tiny particle on the sample will result in the electrical short circuit, and even a small bump on the sample will make sample crack in the future process. So keep in mind that checking every step's results, even a very single step like cleaning. This maybe time-consuming, but it is worthwhile.

The above five points are the main reasons which cause failure to fabricate the novel slider.

To fulfill a successful fabrication, it is recommend that, 1) slider must be fabricated inside a higher class clean room, for example, Class 100, which is the standard class for a successful slider fabrication, 2) contamination and humidity inside clean must be controlled well, 3) MEMS machine should be kept in a well working condition and the recipe of them should be carefully studied, debugged and correctly written inside machine itself, and 4) a good fabrication plan is needed and enough samples should be prepared.